ALMA MATER STUDIORUM - UNIVERSITÀ DI BOLOGNA
CAMPUS DI CESENA
DIPARTIMENTO DI
INGEGNERIA DELL' ENERGIA ELETTRICA E DELL' INFORMAZIONE
"GUGLIELMO MARCONI"

CORSO DI LAUREA MAGISTRALE IN INGEGNERIA BIOMEDICA

In vitro characterization of the three-dimensional strain pattern in human vertebrae affected by metastases

Elaborato in
Meccanica dei Tessuti Biologici

Relatore	**Presentata da**
Chiar.mo Prof. Luca Cristofolini	Giulia Cavazzoni

Correlatore
Dr. Enrico Dall'Ara
Dr. Marco Palanca

Anno accademico 2019/2020

To Francesca

the sweetest “bignolata” ever

Abstract

La colonna vertebrale è la principale sede di metastasi, le quali possono alterare la normale distribuzione dei tessuti ossei e ridurre la capacità della vertebra di sostenere carichi. L'instabilità spinale causata dalle metastasi, tuttavia, è di difficile determinazione. La caratterizzazione meccanica delle vertebre metastatiche permetterebbe di identificare e, di conseguenza trattare, quelle ad alto rischio di frattura.

In questo studio, ho valutato il comportamento meccanico a rottura di vertebre umane affette da metastasi misurando *in vitro* il campo di deformazione.

Undici provini, costituiti da due vertebre centrali, una metastatica e una sana, sono stati preparati e scansionati applicando carichi graduali di compressione in una micro-tomografia computerizzata (μCT). Le deformazioni principali sono state misurate attraverso un algoritmo globale di *Digital Volume Correlation* (DVC) e successivamente sono state analizzate.

Lo studio ha rivelato che le vertebre con metastasi litiche raggiungono deformazioni maggiori delle vertebre sane. Invece, le metastasi miste non assicurano un comportamento univoco in quanto combinano gli effetti antagonisti delle lesioni litiche e blastiche. Dunque la valutazione è stata estesa a possibili correlazioni tra il campo di deformazione e la microstruttura della vertebra. L'analisi ha identificato le regioni in cui parte la frattura (a più alta deformazione), senza identificare, in termini microstrutturali, una zona preferenziale di rottura a priori. Infatti, alcune zone con un pattern trabecolare denso, presunte più rigide, hanno mostrato deformazioni maggiori di quelle dei tessuti sani, sottolineando l'importanza della valutazione della qualità del tessuto osseo.

Questi risultati, generalizzati su un campione più ampio, potrebbero essere utilizzati per implementare nuovi criteri negli attuali sistemi di valutazione dell'instabilità spinale.

Parole chiave: metastasi spinali; instabilità spinale; test meccanici *in vitro;* microCT; Digital Volume Correlation, DVC; analisi delle deformazioni.

Abstract

The spine is commonly affected by metastases which may alter the normal bone tissues distribution reducing the load-bearing capacity and getting spinal instability. The assessment of the spinal instability, however, remains unclear for the majority of patients. A comprehensive characterization of the metastatic vertebrae is fundamental to identify, and consequently treat, those at high risk of fracture.

In this study, I aimed to evaluate the mechanical behaviour at fracture of human metastatic vertebrae, measuring the 3-D strain distributions.

Eleven human spine segments consisting of two central vertebrae (one with metastases and one healthy) were prepared and scanned in step-wise compressive loadings within a micro computed tomography (μCT). Full-field principal strains were computed using a global Digital Volume Correlation approach (BoneDVC).

The strain analysis showed that lytic-metastatic vertebrae provided larger deformations than controls. By contrast, mixed-metastatic vertebrae did not show a univocal trend. They combine the opposite behaviour of lytic and blastic lesions triggering the fracture either in the metastatic or in the adjacent control vertebra. A qualitative investigation of the association between the 3D strain field and the microstructure of the vertebra was performed to identify regions with focalized strain concentration. Regional and sub-regional analyses allowed to identify the onset fracture location without identifying *a priori* a preferential region. In fact, few regions with denser trabecular patterns which were expected to be stiffer, showed larger deformations than normal tissue, highlighting the importance of assessing the bone quality.

This method and the consequent evidence, once generalized on a larger sample, could implement new biomechanical-based criteria in the current scoring systems ensuring clearer guidelines for assessing the spinal instability.

Key words: spinal metastases; spinal instability; mechanical test *in vitro;* microCT; Digital Volume Correlation, DVC; strain analysis.

Contents

Motivations

The spine is a mechanical structure [1] that behaves as a strong pillar for the support of the head and trunk, and the protection of the spinal cord [2]. Proper functioning of the spine may be compromised by diseases as primary spinal tumours and spinal metastases, that alter the bone tissue distribution inside the vertebral body. This non-physiological condition results in an incorrect load distribution that can bring structure to fail. Vertebral fractures lead to severe consequences as pain, instability, paralysis and they increase mortality. In order to prevent vertebral fractures, reduce pain and optimise patient quality of life, clinicians need to choose the most suitable treatment for each different patient evaluating the neurological, oncological, mechanical and systemic conditions, [3], [4] through both their personal experience and diagnostic tools, such as X-ray computed tomography (CT). During the past years many scoring systems were defined to predict the effects of spine metastatic tumours, to give operative support in the clinical dilemma between the surgery or the pharmacological treatment [5]. In 2010 the Spine Oncology Study Group (SOSG) developed a new scoring system to predict the spinal stability in case of neoplastic disease. The Spinal Instability Neoplastic Score (SINS) is used to identify those patients who need a surgical consultancy considering 6 parameters: location of lesion, characterization of pain, type of bony lesion, radiographic spinal alignment, degree of vertebral body destruction and involvement of posterolateral spinal elements. Using clinical and radiographic (CT) evaluations, the final score (from 0 to 18) is obtained adding the scores of each variable. The majority of patients are classified as potentially unstable (SINS from 7 to 12). For these patients no clear guidelines are reported, making the decision of the clinicians more difficult and based on their personal experience [6]. It is logical to think that biomechanical aspects should also be considered: load and strain distributions can change from healthy to metastatic conditions. Indeed, studying the mechanical behaviour of metastatic bony tissue could identify sites and mechanisms of fracture [7]. The aim of this study is to measure *in vitro* the 3D strain distributions in human spine segments, consisting of control and metastatic vertebrae, by using Digital Volume Correlation (DVC) to locally characterize the metastatic vertebra and study if particular metastatic features are correlated to specific fracture pattern. Specimens were tested in step-wise loading conditions within a micro-computed tomography (μCT) at the University of Sheffield (UK). A global DVC algorithm (BoneDVC, previously known as ShIRT-FE) was used to evaluate the displacements and strains fields.

CHAPTER 1: Background

1.1 Anatomy of the spine

The spine is a mechanical structure [1]. Vertebrae are articulated bone segments that constitute the spinal column, also called spine. The spine is overall composed of 33-34 vertebrae: 7 cervical vertebrae (C1–C7), 12 thoracic vertebrae (T1–T12) and 5 lumbar vertebrae (L1–L5); in terminal regions, sacrum and coccyx, vertebrae are fused together in group of 4 and 4-5 respectively. Vertebrae are irregular short bones, whose dimensions and mass increase from cervical to lumbar region precisely to adapt to the progressively increasing compression loads to which the vertebrae are subjected [1]. A typical vertebra consists of the vertebral body, that is the largest part of a vertebra, more or less cylindrical in shape [2] and of the vertebral arch, a posterior bony ring connected to the body by a pair of pedicles and laminae from which arise seven articular processes (posterior bilateral joints, connecting each vertebra to the adjacent one).

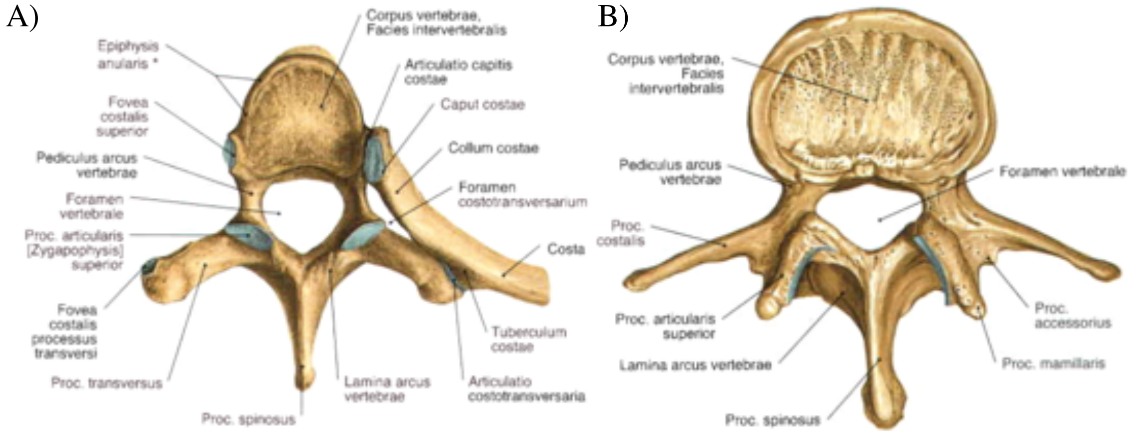

Figure 1: A) Typical structural features exemplified by the fifth thoracic vertebra; superior view. B) Fourth lumbar vertebra; superior view [8].

In particular, in this study we focused on the measurement of internal strains in the vertebral bodies of the thoraco-lumbar spine. Thoracic vertebrae (Fig. 1A) increase in size from above downward. They are mechanically stiffer and less mobile than any of the other regions thanks to the presence of the costovertebral articulations, the rib cage structure and the pedicle orientation. This ensure the needed bipedal support and protection of the cord as well as the other organs in the thoracic cavity [1]. Thoracic vertebrae are distinguished by the presence of facets on the sides of the bodies for articulation with the heads of the ribs, and facets on the transverse processes of all vertebrae, except T11 and T12, for articulation with the tubercles of the ribs [2]. Lumbar vertebrae (Fig. 1B) are the largest segments of the movable part of the spine because they are highly stressed both by the superimposed body weight and muscular forces. In addition, the lumbar spine in conjunction with the hips is responsible for the mobility of the trunk [1]. Lumbar vertebrae can be distinguished by the absence of a foramen in the transverse process, and by the absence of facets on the sides of the body [2]. To connect to the sacro-vertebral joint, the last lumbar vertebra (L5) is characterized by a much deeper body in front than behind. With the exception of the sacral region and the coccyx, each vertebra is independent by the others; they all are articulated through fibrocartilage pads, called intervertebral discs, joint capsules and various ligaments. Additionally, the spine has many muscle insertions which provide spinal stability along with dynamic neuromuscular control systems [1].

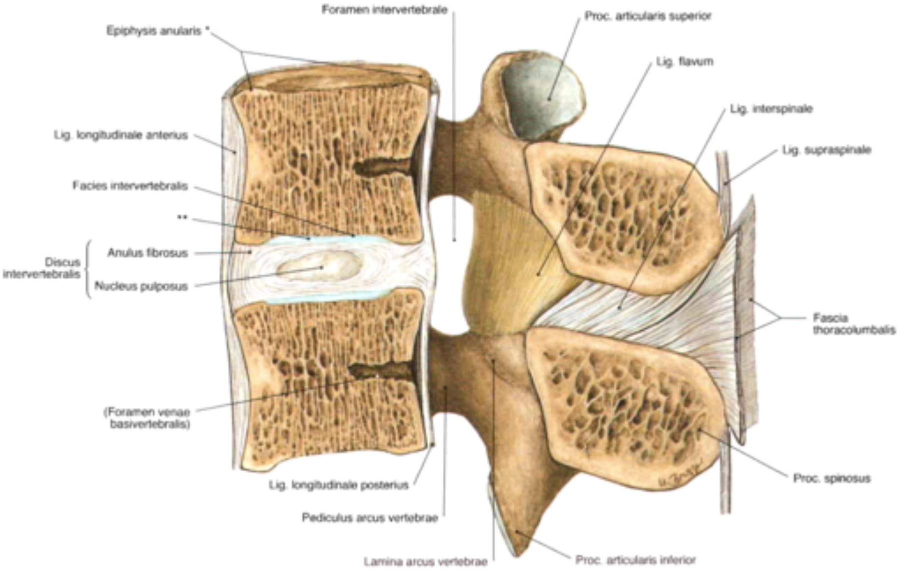

Figure 2: Lumbar motion segment; schematic median section [8].

From a mechanical point of view, the role of the vertebrae and the entire spine is fundamental in supporting body weight, in allowing physiological motions such as torsion, anterior and lateral flexion of the head, trunk and pelvis (motor function) and in the transfer of loads and the resultant bending moments of the head, trunk, and any weights being lifted to the pelvis [1]; it also has a nerve-protecting function against the spinal cord. Figure 3 shows the directions in which the physiological movements of the spine, and then the mechanical stresses, occur.

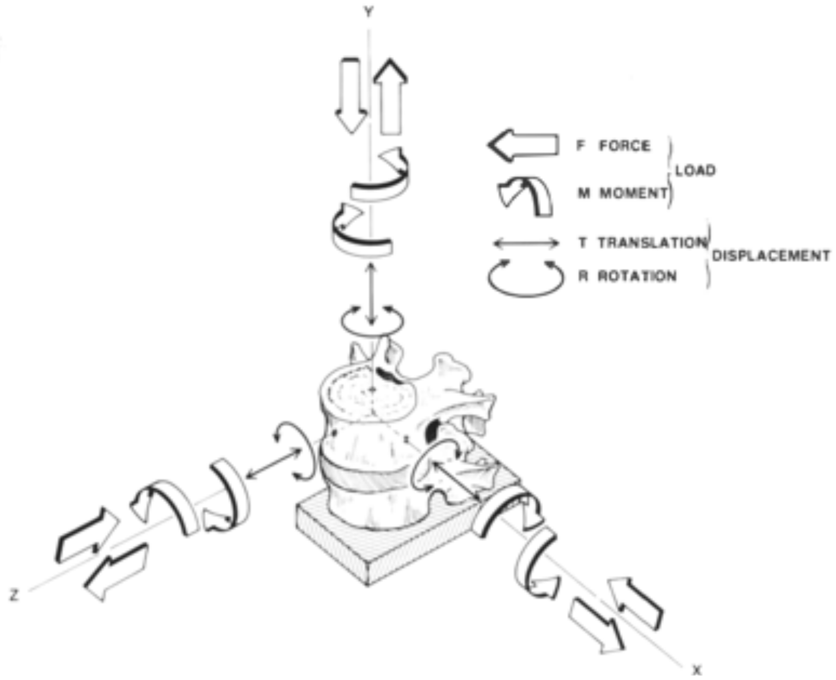

Figure 3: Representation of physiological motions (3D coordinate system at the centre of the upper vertebral body of a motion segment. The coordinate system is fixed in space) [1].

Vertebral bodies are primarily made up of trabecular bone, which is covered by a cortical shell. In almost all physiologic situations, it is the vertebral body that carries the greatest loads and transmits them from the superior to the inferior end-plate of the vertebra, in fact, the thin bony lamellae of the cancellous tissue are more pronounced in lines perpendicular to the upper and lower surfaces in response to greater pressure in this direction [2]. For this reason, vertebrae are often tested under compression along the cranio-caudal direction. White and Panjabi summarized the compressive strength properties of cancellous bone of vertebrae measured on trabecular samples (Table 1) [1].

However, for the mechanical characterization it would be better to use a functional spinal unit (FSU), called also motion segment (Fig. 2), that is the smallest segment of the spine that exhibits biomechanical characteristics similar to those of the entire spine [1]. Specimens consisting of spine segments allow us to reproduce a more physiological condition due to the fact that they include besides the vertebra itself, also the soft tissues. In fact, the load distribution across the vertebral endplate depends also on the anatomy and health of the adjacent intervertebral discs [9]. As previously described, the different regions of the spine have different stiffness as they are stressed by different loads, therefore also the mechanical properties will be different according to the region considered as reported in Table 2.

Table 1: Compressive Strength Properties of Cancellous Bone of Vertebrae [1]

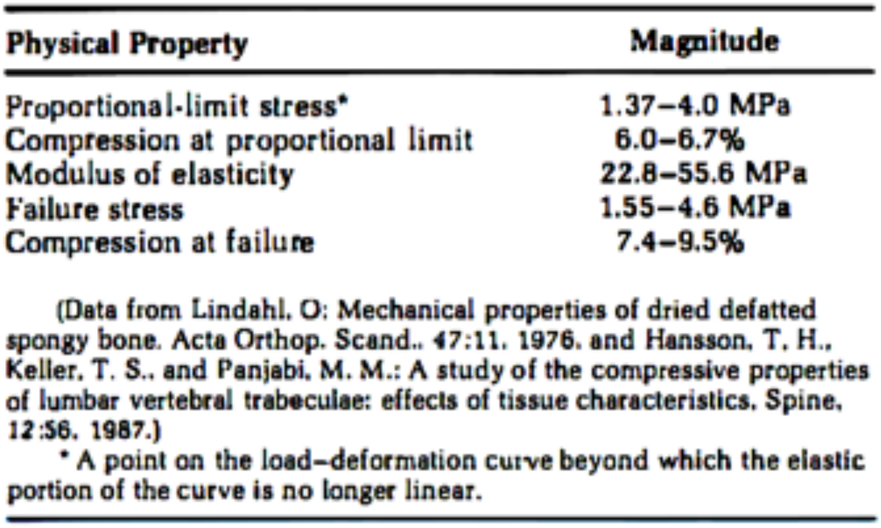

Physical Property	Magnitude
Proportional-limit stress*	1.37–4.0 MPa
Compression at proportional limit	6.0–6.7%
Modulus of elasticity	22.8–55.6 MPa
Failure stress	1.55–4.6 MPa
Compression at failure	7.4–9.5%

(Data from Lindahl, O: Mechanical properties of dried defatted spongy bone. Acta Orthop. Scand., 47:11, 1976, and Hansson, T. H., Keller, T. S., and Panjabi, M. M.: A study of the compressive properties of lumbar vertebral trabeculae: effects of tissue characteristics. Spine, 12:56, 1987.)

* A point on the load–deformation curve beyond which the elastic portion of the curve is no longer linear.

Table 2: Average Stiffness Coefficients of a Representative Functional Spinal Unit in Different Regions of the Spine (Note that these numbers are simple representation of complex spinal behaviour) [1].

	Forces (N)				
	Tension (+FY)	Compression (-FY)	Ant. Shear (+FZ)	Post. Shear (-FZ)	Lat. Shear (FX)
	Stiffness Coefficients (N/mm)				
Cervical	53	200	50	53	53
Thoracic	770	1250	110	110	110
Lumbar	770	2000	121	170	145
Sacroiliac*	156	294	108	189	385

*One ilium fixed

Unfortunately, some pathological conditions, as osteoporosis, primary spinal tumours and spinal metastases, can invalidate the correct vertebral functionality reducing movement capacity, weakening tissue, increasing the risk of fracture and modifying the mechanical stiffness and strength of the entire spine.

1.2 Spinal metastases

Primary spinal tumours are a very rare condition; they represent the 0.2% of all malignant tumours [10]. On the other hand, axial skeleton and, in particular the spine, is commonly affected by metastatic disease. Metastases are secondary tumour masses: cancer cells move from different organs (breast, prostate, etc.) where the primary tumour is located. The incidence of bone metastases varies considerably from one tumour type to another (breast, prostate, etc..) [11]. Spinal metastases can be either lytic, blastic, or mixed. Clinically, lytic bone metastases are much more frequent and cause most morbidity [11]. Lytic metastases have been called bone destructive [12] due to the increased osteoclastic activity and/or number of osteoclasts that compromises the highly oriented trabecular structure of the vertebral body destroying trabeculae, generating micro-fractures [11], [13]. The related lack of mineralization and loss of structural integrity corresponds to a weakening, a reduction in the load-bearing capacity of the remaining bone [12], [13] and indirectly, increases the risk of collapse [3]. In fact, in the past years it has already been shown how bone diseases [14] or age [15] can decrease the bone mineral content and how a small loss of bone tissue (e.g. 25%) produces considerable loss in the vertebral bone strength (e.g. 50%) (Fig. 4). This has to do with the load-bearing capacity of the vertical and horizontal trabeculae, which in the presence of lytic metastases are reduced and poorly oriented, thus weakening the entire structure.

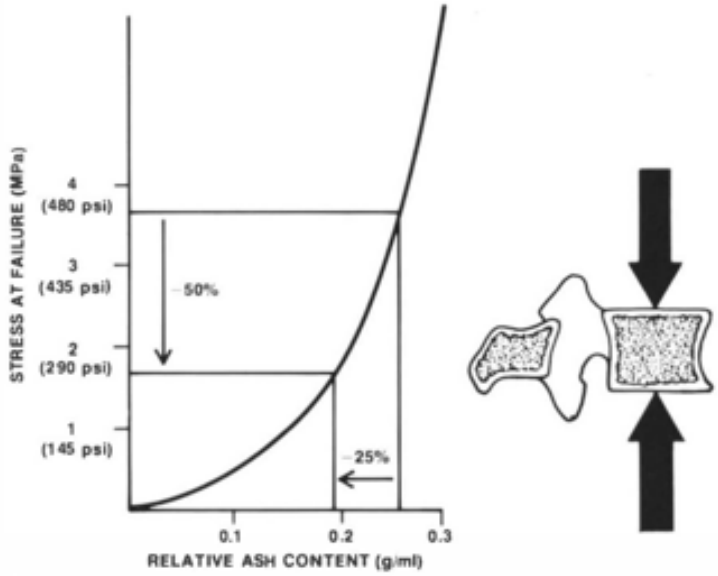

Figure 4: Relationship between osseous tissue and vertebral strength [1].

On the other hand, blastic metastases promote osteoblastogenesis [12]. This process forms new bone tissue, mineralized but poorly organized that covers the normal trabecular structure (limited bone quality). Through a quantitative computed tomography (qCT) or a micro computed tomography (μCT) scanner, it is possible to evaluate how both kinds of lesions alter the normal tissue distribution: lytic metastases create voids inside the trabecular reticulum and/or in the cortical shell, blastic metastasis deposit excess of bone tissue. Mixed-metastatic vertebrae are characterized by both lytic and blastic lesions (Fig. 5).

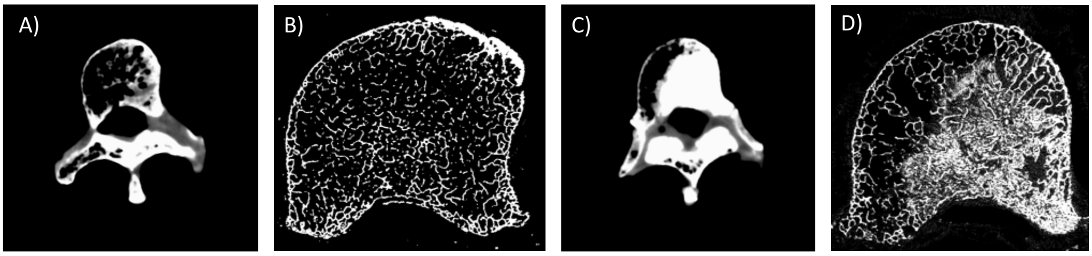

Figure 5: Healthy and mixed-metastatic vertebra scan with a qCT (A, C) and μCT (B, D) respectively.

Because of the altered balance of the bone remodelling process and, as a consequence, the altered distribution of the bone tissue inside the vertebra, both kind of vertebral metastases can often cause mechanical instability of the spine. The Spine Oncology Study Group (SOSG)[1] defines spinal instability as loss of spinal integrity as a result of a neoplastic process that is associated with movement-related pain, symptomatic or progressive deformity, and/or neural compromise under physiologic loads [3]. This is not just a pure orthopaedic problem, all of these patients have also a compromised and generally poor health status. In fact, oncologists and orthopaedists decide which treatment, whether conservative or surgical, is more suitable for each patient upon many factors, including general patient health, neurological status, prognosis, tumours histology and spinal stability [3], [5]. Treatment choice depends also on tumour sensitivity to chemo/radiotherapy, the number of involved vertebrae and life expectancy [16]. Over the past 15 years, the multidisciplinary spine team at Memorial Sloan-Kettering Cancer Center (MSKCC) has developed a decision framework for metastatic spine disease, called NOMS (Neurologic, Oncologic, Mechanical instability, and Systemic disease) [4]. This

---

[1] The SOSG is an international group of 30 spine oncology experts and thought leaders from North America, Europe, South America, and Asia who meet biannually to discuss research, assess the best evidence for current practices, and formulate clinical trials to advance the field of spine oncology [3]

multidisciplinary approach allows the correct determination of the optimal combination of radiotherapy and surgery. The goal is to minimize the surgical intervention for making surgery safer for the patients [4]. In the NOMS mechanical instability is a condition that is defined separately for pathological fractures. The probability of developing a fracture increases with the duration of metastatic involvement [13] and it is also influenced by metastases location and size [17], [18]. Radiation, although effective for local tumour control, has no impact on spinal stability [4]. Thus, in order to treat fractures, stabilization interventions (brace application, percutaneous cement and/or pedicle screw augmentation, or open surgery) are needed. These surgical treatments are difficult and risky [13]: they may force patients to bed rest, aggravate pain and other symptoms [17]. So, over-protection may result in unnecessary constraint and reduction of quality of life, while insufficient treatments may lead to fractures and deformities of the spine with possible neurological consequences [10]. Therefore, the prediction of the fracture risk for each specific patient gains a huge clinical relevance [17]: it would allow to implement preventive solutions that could benefit patient's quality of life.

1.3 Spinal Instability Neoplastic Score (SINS)

Historically, fracture prediction in patients with cancer and/or bone metastases was primarily founded on experts' opinions based upon clinical experience and descriptive studies. At first, information was obtained in 2-dimensions by X-ray and skeletal scintigraphy, later with Digital 3D imaging as CT: the accurate and precise evaluation of the tumours burden and its structural implications on the remaining bone are fundamental for the evaluation of the fracture risk [12]. Over the years many scoring systems have been developed [5] as prognostics tools for surgeons. Nowadays in the clinical practice, a new classification scheme is widely used to evaluate the mechanical instability of the spine and then, the risk of fractures. Spinal Instability Neoplastic Score (SINS) is a scoring system developed in 2010 by the Spine Oncology Study Group (SOSG) based upon clinical (patient pain) and objective radiological elements. SINS can help healthcare professionals (surgeons, oncologists, radiologists and orthopaedics) in developing optimized treatment plans by identifying those patients who require surgical assessment [19] and may benefit the most from a surgical intervention; those who cannot support such invasive operation and those who may benefit the most from other therapeutic options [19], as chemo/radiotherapy. To evaluate spinal instability, SINS assesses and scores 6 variables: location of lesion, characterization of pain, type of bony lesion, radiographic spinal alignment, degree of vertebral body destruction and involvement of posterolateral spinal elements (Table 3).

Table 3: Elements of SINS [3]

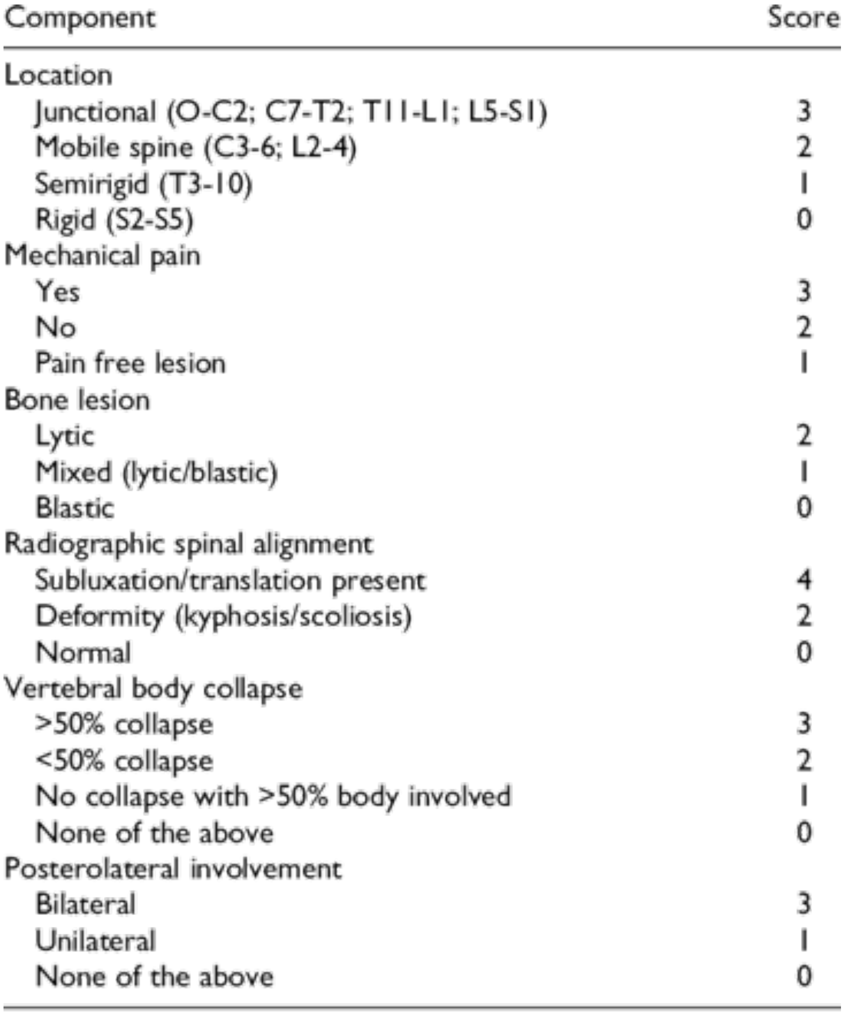

Component	Score
Location	
Junctional (O-C2; C7-T2; T11-L1; L5-S1)	3
Mobile spine (C3-6; L2-4)	2
Semirigid (T3-10)	1
Rigid (S2-S5)	0
Mechanical pain	
Yes	3
No	2
Pain free lesion	1
Bone lesion	
Lytic	2
Mixed (lytic/blastic)	1
Blastic	0
Radiographic spinal alignment	
Subluxation/translation present	4
Deformity (kyphosis/scoliosis)	2
Normal	0
Vertebral body collapse	
>50% collapse	3
<50% collapse	2
No collapse with >50% body involved	1
None of the above	0
Posterolateral involvement	
Bilateral	3
Unilateral	1
None of the above	0

The scores for each variable are added, and a final score is obtained (Table 4). The minimum score is 0, and the maximum score is 18. A score of 0 to 6 denotes stability, a score of 7 to 12 denotes indeterminate (possibly impending) instability, and a score of 13 to 18 denotes instability. For SINS greater than 7, a surgical consultation is recommended [3]. Otherwise SINS score can be considered as a binary indicator of surgical referral status: ‘stable’ (0-6 points) or ‘current or possible instability’ (7-18 points) [20].

Table 4: SINS scores organized as a total score, three-clinical categories, and binary scale with their corresponding levels of stability where surgical consultation is recommended for a total score ≥ 7 [20]

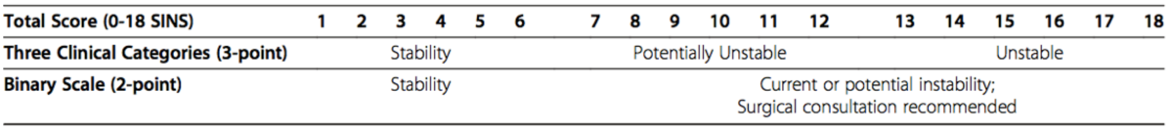

Total Score (0-18 SINS)	1	2	3	4	5	6	7	8	9	10	11	12	13	14	15	16	17	18
Three Clinical Categories (3-point)	Stability						Potentially Unstable						Unstable					
Binary Scale (2-point)	Stability						Current or potential instability; Surgical consultation recommended											

One of the most critical aspects is that for patients with a score between 7 and 12 (potentially unstable) no clear guidelines are reported, making the decision of the clinicians more difficult and based on their personal experience [6]. However, it has been shown that the SINS has a near-perfect inter- and intra-observer reliability in determining three clinically relevant categories of stability (sensitivity of 95.7% and specificity of 79.5% [19], [21]) and it is able of appropriately identifying as requiring surgical assessment all unstable and 98.7% of potentially unstable patients [19]. Despite that, SINS reliability is still controversial. In fact, Fisher et al. demonstrated that cases can be classified differently if the SINS is applied by a radiologist or a surgeon: 20% of the cases that the surgeons identified as stable were considered potentially unstable by the radiologists [19]. Moreover, poor correlation was found between the SINS and the biomechanical outcome in case of metastatic vertebrae [22]. Palanca et al. [10] demonstrated that, in two of the three considered cases, SINS did not suggest any spinal stabilization, giving low scores (e.g. 4-6), while the biomechanical tests had shown that these patients were at high risk of fracture. According to Costa et al. [6] SINS is not related to the compressive strength of the vertebra with lesions because no correlation was found between the scoring system and the mechanical properties estimated from computational models. Nevertheless, mechanical properties, as bone strength [7], are related to the presence of metastases. Loads and strain distribution can change from healthy to metastatic condition. Indeed, transfer of loads between the vertebrae depends on parameters such as the quality of the bone tissue and the intervertebral discs, the size and shape of osteophytes[2], if present [23]. So, further elucidation of the mechanical behaviour of bony tissue affected by metastatic disease could identify sites and mechanisms of fracture [7]. As in the diagnosis of impending pathological fractures in long bones (Mirels' score, 1898 [24]), biomechanical criteria should be added to the clinical scores to ensure clearer guidelines for bone stabilization.

---

[2] Osteophytes are bone spurs that grow on the vertebrae

1.4 Mechanical characterization of the spine: state of the art

In 1997, Taneichi and colleagues [16] reported that the mechanical properties of the metastatic spine and the mechanisms of collapse were still unknown. Today, the characterization *in vivo, in vitro* and *in silico* of the mechanical properties of the spine in physiological conditions, in presence of pathologies such as vertebral metastases or after treatments, is widely reported in the scientific literature. In particular, spinal strain field measurement should be used to study the effects of metastases on failure mechanics in bone helping in predicting vertebral fracture.

In vitro experimentation allows us to measure mechanical and apparent properties (stiffness, strains, failure strength, mode of failure) of the spine by applying at the specimen simplified loading conditions (e.g., axial compression) [25]. *In vitro* tests must be repeatable, proving a consistent response when the same input is given several times; and reproducible, providing the same output when performed in different instances, following the same protocol. This allows us to compare the results obtained from the same test, carried out following the same protocol, on two different specimens, such as two vertebrae, one with and one without metastases. Due to the fact human cadaveric specimens are difficult to obtain and their use is subjected to strict ethical regulation, more often animal models from the alimentary chain are used [25]. However, there are strong anatomical differences within quadrupeds and humans, both in terms of dimensions (porcine vertebral bodies is smaller in size and have a thicker of the cortical shell) and microstructure (porcine vertebra are denser than human ones). The bone structure and its mechanical properties, as the range of motion and the stiffness [26], differ depending on the level of the spine and the different physiological loads: the spine in quadrupeds is mostly subjected to bending, while the human spine is optimized for axial compression [25]. In both human or animal cases, the specimen type is generally chosen based on the purpose of the study (Fig. 6). Specimens consisting of spine segments (series of adjacent vertebrae) are useful for characterizing kinematics and spinal instability. This type of specimens allows us to reproduce a more physiological condition due to the fact that it includes besides the vertebra itself, also the soft tissues. In fact, the load distribution across the vertebral endplate depends on the anatomy and health of the adjacent intervertebral discs [9], which are viscoelastic structure that acts as shock absorbers [2]. If instead the goal is to study the structural properties of the single vertebra, specimens that include only one whole vertebra or the vertebral body, with or without end plates, can be used. Here the load is no longer applied through the discs (all soft tissues are removed) but directly on the surface of the vertebra or on the end plate, sometimes embedded in polymethyl-methacrylate (PMMA). In this scenario, the absence of adjacent intervertebral discs may limit the physiological relevance of the results because of artefactual failure mechanisms [9]. Trabecular and cortical core specimens are unrepresentative of the behaviour of the whole vertebra, but they are mainly used for a more in-depth analysis of the local mechanical properties of the bone tissue [25].

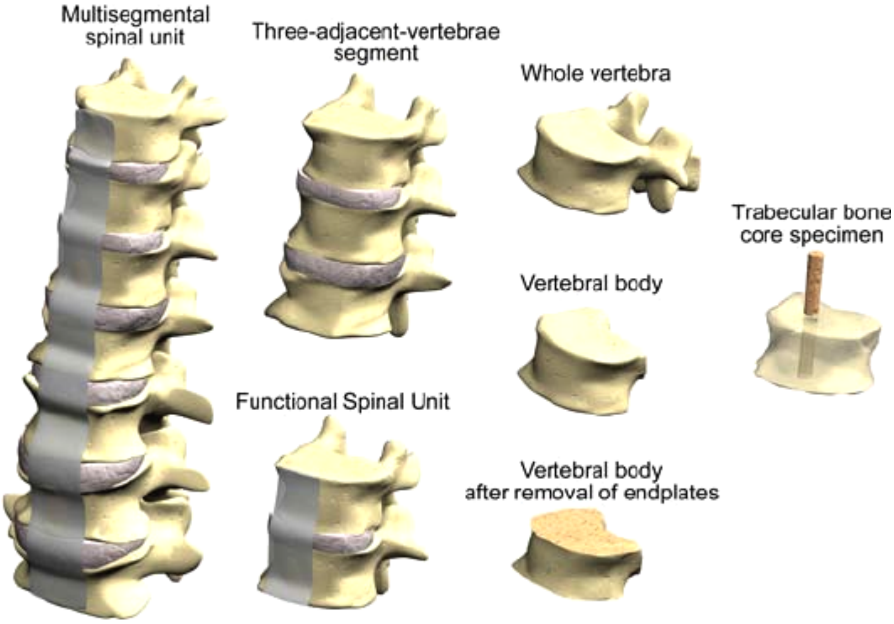

Figure 6: Main types of specimens used for in vitro testing [25].

Moreover, the most appropriate loading condition must be chosen. Spine segments are subjected to many types of loads as compression, torsion, flexion, extension, and lateral bending or their combination [1] but the real physiological extent of these loadings is still unknown. Even if today mathematical models are a non-invasive method that can be used for predicting forces and moments, *in vivo* tests are considered more reliable even than the *in vitro* ones, that are not able to simulate muscle structures and the neuromuscular controls [1]. Telemetric implants enable the measurement of forces and moments transmitted through the implant, but not through the vertebra. Under physiological conditions intervertebral discs are responsible for loads transmission and absorption from one vertebra to the adjacent one but the information obtained through implant transducers in the nucleus pulposus of the disc are not an actual measure of the supported load [25]. Brandolini and colleagues [25] have collected a lot of data from the literature for both spine segments and single vertebrae regarding ranges of loadings conditions. Table 5 reports data extracted from [25] for spine segments tested under compressive axial loadings. Each of the reported loads (ultimate load) corresponds to a different deformation field to which the spine is subjected. To date, many tools can be used to measure the local or global strain field on the surface of the specimen and within the bone. A more detailed description is given below.

Table 5: Ultimate load for different intact spinal segments (data extracted from [25]) .

Region	Ultimate load (average± std dev.)	Number of specimens	Ref.
T5 – T7	2409±1233 N	114	Bürklein D et al., *Correlation of thoracic and lumbar vertebral failure loads with in situ vs. ex situ dual energy X-ray absorptiometry*, J Biomech 34(5):579–587, 2001.
T9 – T11	3174±1596 N		
L2 – L4	3009±1505 N		
L1 – L5	810±10090 N (range)	52	McLain RF et al. *Comparative morphometry of L4 vertebrae: Comparison of large animal models for the human lumbar spine*, Spine (Phila Pa 1976) 27(8): E200–E206, 2002.
T10 – T12	2080±1420 N	22	Moro M, Hecker AT, Bouxsein ML, Myers ER, *Failure load of thoracic vertebrae correlates with lumbar bone mineral density measured by DXA*, Calcif Tissue Int 56(3):206–209, 1995.
L1 – L3	2620±1510 N		
All FSUs* from T7 to L5	1800 N (OP fracture) 3090 N (Traumatic fracture) 3240 N (Non discernible fracture)	73	Jiang G et al. *Vertebral fractures in the elderly may not always be "osteoporotic"*, Bone 47(1):111–116, 2010.

* FSU = functional spinal unit

1.4.1 Strain gauges and extensometers

Extensometers and strain gauges are among the first instruments used to measure deformations on a specimen. These tools have been broadly used for investigating local surface strains. Triaxial strain gauges allow measurement of the principal strains and their orientation on the vertebral body surface (Fig. 7) [25] at the point where they are glued.

Strain gauges were used to evaluate the apparent properties and pointwise strains on intact vertebrae, [27] single human vertebrae [28], [29] and spinal segments [30] with simulated metastatic lesions. These results can be compared with those estimated from *in vivo* measurements, and used to locate the regions on the vertebra undergoing the higher strains [25]. As well as strain gauges, extensometers are a common tool to measure strains across the whole vertebra on which they are fixed [31]. Both strain gauges and extensometers must be fixed to the specimen by an operator, therefore they will involve both an intrinsic error of the instrument, and random errors related to malposition and misalignment; moreover, they could measure the apparent tensions due to bone dehydration. Even if they are very precise tool, they only provide a measurement of the strain averaged over a small area where they were fixed. Thus, part of the useful information is lost: what happens in the nearby points where the strain gauges are not attached is not detected. Moreover, extensometers may induce micro-damage in bone, and measure the average strain over the gauge length [32].

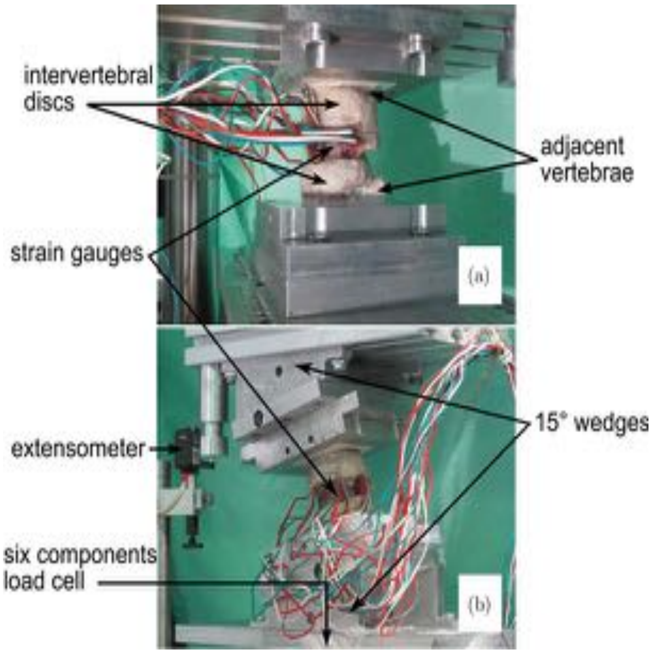

Figure 7: Set-up for non-destructive testing of three adjacent vertebrae in an over-constrained condition [25].

As already mentioned, the functional spine unit (FSU) is the smallest specimen that exhibits biomechanical characteristics similar to those of the entire spine [1]. This kind of specimen includes both rigid tissues (vertebral body) and soft tissues (intervertebral discs, ligaments, etc.). However, strain gauges and extensometers cannot be used to measure the strain in soft tissues as they would perturb the local stiffness of the structure invalidating the result [33].
Thus, in order to investigate the full-field strain distribution on the external surface and in both hard and soft tissues of the FSU, a different technique, known as Digital Image Correlation, can be used.

1.4.2 Digital Image Correlation (DIC)

The use of tools as strain gauges does not allow to measure either the global strain distribution on the entire surface, nor inside the vertebra and they also cannot evaluate the strain field in soft tissues. Among the most recent techniques used to measure the strain field on the entire surface of a specimen, there is the Digital Image Correlation (DIC) approach. It is a contactless method that compares series of digital images of the same specimens starting from the original and unloaded state and up to selected loading conditions (displaced and/or deformed state). Images are acquired by one (2D-DIC), two or more cameras (3D-DIC) (Fig. 10). These images are divided into smaller sub-images called *facets*. Then a matching algorithm is used to match the *facets* between the reference and deformed state [32]. So, the algorithm computes the displacement field, and the strain field is obtained by derivation. To guarantee the recognition of each different *facets,* on the surface of the specimen is created a high-contrast random pattern. This must deform together with the specimen surface and must not alter the biological specimens. The typical one is the black-on-white speckle pattern that uses water-based paints which minimise the alteration on biological specimens [32].

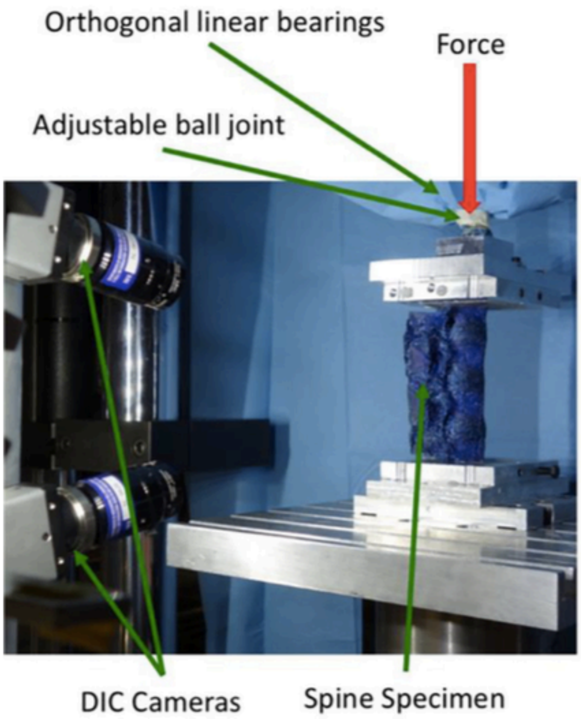

Figure 10: Loading and acquisition system [34].

The DIC provides the displacements field on a portion of the surface of the specimen, with an excellent accuracy and precision [34]. The strain field, instead, is obtained by differentiation process, that enhances the noise present in the computed displacements field, causing loss of accuracy and precision [35]. Zero-strain test should be performed in order to measure these systematic and random errors (Fig. 11), that could be minimized optimizing the DIC parameters, such as the facet size, the grid spacing, the strain computation window, the validity quote and the filtering [32]. Compared to strain gauges, the DIC technique has more noise but DIC can provide a full-field information [32].

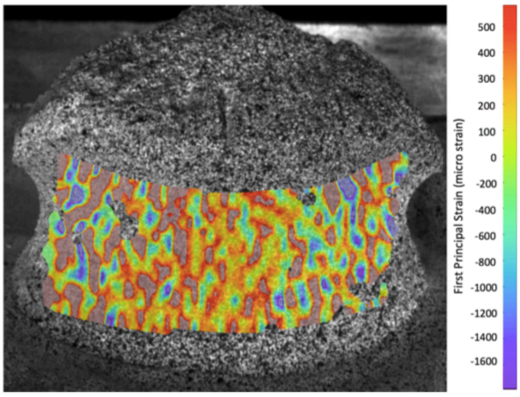

Figure 11: Test of correlation on a vertebra specimen (L5, anterior view): the apparent strain in a zero- strain, zero-displacement condition is shown, without application of any filtering [35].

The DIC technique has already been applied to measure the full-field strain distribution on the cortical surface of a whole vertebra and in multi-vertebra spine segments. Mechanical tests have been carried out both with the use of human specimens with primary spinal tumours [10], with simulated metastases [18] and specimens of animal origin. Palanca et al. [34] tested porcine spine segments with two loading configurations (flexion and lateral bending (Fig. 10)). The same protocol has now been repeated on human multi-vertebra segments to study the effects of spinal metastases on the strain distribution applying three different loading conditions: anterior bending, lateral bending and uniaxial compression [36]. A great advantage of this technique is that in a multi-vertebrae segment of spine, it allows to study simultaneously the deformations on hard and soft tissues, such as the intervertebral discs [33], [37] and the ligaments [38] as shown in Figure 12. From the results obtained in the study by Ruspi et al. [33] it emerged how important it is to investigate the biomechanics of the spine with a full-field tool capable of measuring the different magnitude and direction of the strain field on the surface of different types of tissue.

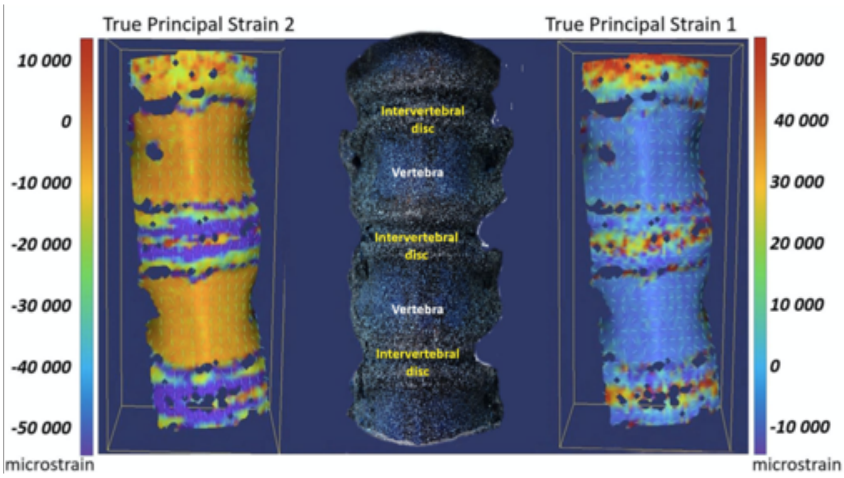

Figure 12: Different deformation of vertebral body, growth cartilages and intervertebral discs during an anterior bending test from a frontal view. From left to right: minimum principal strain (compression), specimen as viewed by the cameras, maximum principal strain (tension). Porcine specimens were used [33].

Unfortunately, Digital Image Correlation is unable to provide any direct information about the evolution of the internal displacement and strain distributions under load [39]. Furthermore, it is unable to quantify internal vertebral micro-damage evolution [39] and the related mechanical properties. Today all these characterizations are possible thanks to a different technique, a 3D-extension of the Digital Image Correlation (DIC) known as 3D Digital Volume Correlation (DVC).

1.4.3 Digital Volume Correlation (DVC)

The DVC technique created in 1999 by B. Bay, is an inspection tool for the visualization of internal damage, and for the identification of internal strain distributions in heterogeneous materials [40]. DVC operating principle is a 3D-extension of the DIC: it combines computed tomography (CT) imaging with *in situ* mechanical testing [41]. This method allows researchers to measure the field of displacements and, by differentiation, the strain field inside a structure by optimising a cost function used to compare small sub-volumes of subsequent CT scans of a sample. These images are acquired in undeformed and deformed (elastic or plastic) conditions. Since micro-CT (μCT) has been developed in the 1980s by J.C. Elliott and S. D. Dover [42], it immediately became popular in the medical research thanks to its higher resolution. In fact, compared to a conventional clinical-CT it has a much smaller field of view with a higher resolution detector. μCT reconstructs the 3D structure of the specimen using the differences in the X-ray attenuation properties of the materials. Therefore, it is ideal for microstructural analysis in trabecular bone because it provides adequate resolution in 3D, has excellent contrast in bone and has very little geometric distortion [43]. When the specimen used is an FSU, both the hard tissues (vertebral body) and the soft tissues (e.g. intervertebral discs) are scanned. The problem is that μCT demonstrated excellent spatial resolution, but poor soft tissue contrast. To elevate soft tissue contrast a contrast agent can be used [44].

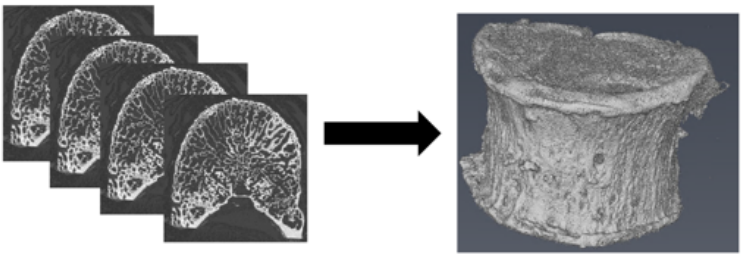

Figure 13: The μCT through stack of 2D images produce an image volume (3D image).

The μCT gives as results a stack of 2D images that produce a volumetric image (3D image) of the specimen (Fig. 13), which is scanned in both unloaded and step-wise loading conditions. In order to measure the displacement and strain distribution, different DVC approaches can be applied (Fig. 14). A local (subset-based) DVC approach performs the registration of small subsets of image data [31] and independently correlates, using direct correlation (DC) or fast Fourier transform (FFT), sub-volumes from deformed to undeformed states as a discrete function of grey-levels [45], [46]. For each sub-volume the displacement field is evaluated in the central point. Then the strain field is computed via centred finite differences [46]. A global DVC approach performs registration of an entire image dataset containing, for example, the whole human vertebra and not just portions of it. The local load-induced displacement in the structure is identified by superimposing to the images a 3D grid of discrete points with selectable nodal spacing (sub-volumes) defined with respect to the reference image (usually the unloaded condition is taken as the reference image). At each node of the sub-volumes, the correlative imaging algorithm solves the elastic registration equations to compute the displacement field [46]. Then the displacement fields can be differentiated using various numerical differentiation approaches [45].

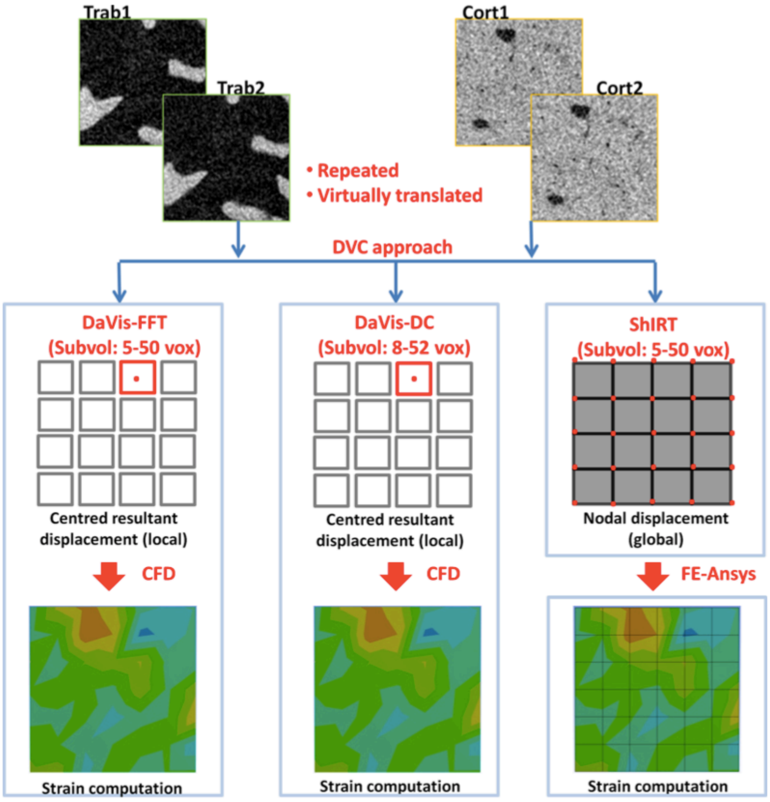

Figure 14: Description of the three DVC approaches [45]

For example, BoneDVC (previously known as ShIRT-FE) is a global approach that obtains the strain field using an FE software (ANSYS) to differentiate the displacement field previously obtained (Fig. 15). The FE software converts the 3D grid in an 8-noded hexahedrons mesh and uses the measured displacements as boundary condition [41], [46]. In 2016, Palanca et al. [46] demonstrated that a global approach applied to a whole vertebral body is more robust for strain measurements than a local approach. In fact, they showed the global approach had maximal errors that were three orders of magnitude lower than the ones of the local approach.

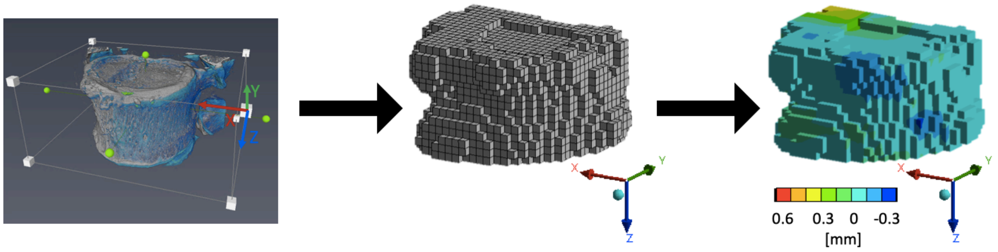

Figure 15: A) Rigid Registration on Amira, B) Mesh generation (BoneDVC, Ansys), C) 3D colour map of the displacement field on the X-Axis (Ansys)

As well as in the DIC, the quality of the input images (e.g. image contrast, signal-to-noise ratio, voxel size, etc.) and the DVC parameters (e.g. sub-volume size, objective function, etc.) can affect the accuracy and precision of the displacement and strain measurements [31]. In fact, the larger the sub-volume size and the nodal spacing, the lower the measurement uncertainties and, consequently, the larger (worst) the measurement spatial resolution [45], [47]. Accuracy and precision of the DVC method were defined by Liu et al. [48] as the mean absolute error (MAER) and the standard deviation of the error (SDER). They were quantified as the mean and the standard deviation of the average of the absolute values of the six strain components for each sub-volume:

$$MAER = \frac{1}{N}\sum_{k=1}^{N}\frac{1}{6}\sum_{c=1}^{6}\left|\varepsilon_{c,k}\right| \tag{1}$$

$$SDER = \sqrt{\frac{1}{N}\sum_{k=1}^{N}\left(\frac{1}{6}\sum_{c=1}^{6}\left|\varepsilon_{c,k}\right| - MAER\right)^{2}} \tag{2}$$

where "ε" is the strain; "c" represents the strain component; "k" represents the point of measurement; "N" is the total number of measuring points.

The relationship between the precision of the method and the size of the sub-volume for both a global (BoneDVC, top) and a local (Davis-DC, bottom) DVC approach is shown in Figure 16. As the sub-volume size increases, the SDER decreases and the precision increases. Figure 16 shows the correlation between precision and sub-volume size for different structures, both animal and human. It is useful to point out that some differences between cortical and trabecular bone are present: accuracy and precision errors were found higher for cortical bone than for trabecular bone [41]. In fact, according to Palanca et al. [46] the errors increased passing from the trabecular tissue, rich of features, to the thin cortical bone, and finally to the surrounding saline solution. As shown in Figure 17, higher values of strain in the cranio-caudal direction are reached at the boundary regions of the specimen.

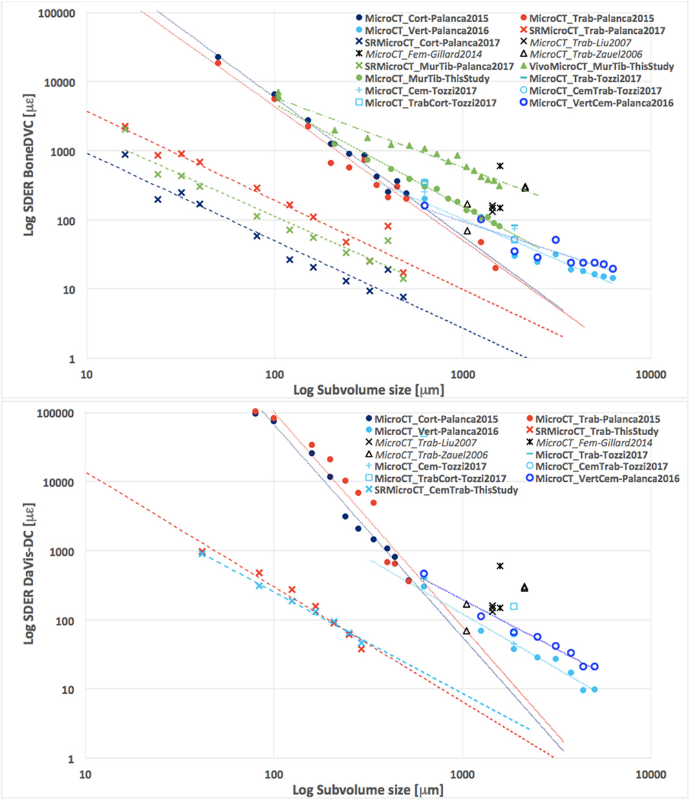

Figure 16: Relationship in logarithmic scale between the standard deviation of the error (SDER; median values in case more specimens were analysed per group) and the sub-volume size for both global (BoneDVC, top) and local (DaVis-DC, bottom) DVC approaches [41].

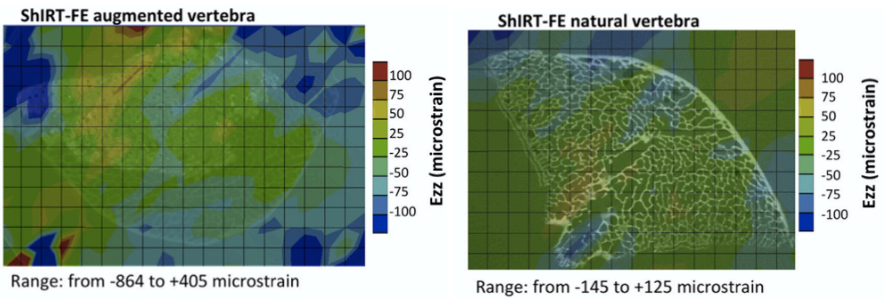

Figure 17: Strain distribution in the cranio-caudal (z) direction with a sub-volume size of 48 voxels on a mid-height cross-section of typical augmented (A) and natural (B) vertebra for the global approach (ShIRT-FE) [46].

It also should be noticed that, as well as in the DIC technique, the derivation process used to obtain the strain field amplify all these errors [41]. As with the DIC technique, accuracy and precision of the method can be estimated with the "zero-strain" test. It consists in registering repeated scans of the same undeformed specimen [41], [48], [49] ("zero-strain" condition) which account for the image noise. It can also be performed by registering scans of the same virtually displaced [47], loaded [49] or deformed [50] specimen. However, these methods probably underestimate the uncertainties due to the absence of the image noise [49]. Also, over the years, improvements in computer processing power and better optimized algorithms have reduce the computation time required for each displacement calculation.

A major limitation of the DVC approach concerns the time consuming process to acquire 3D images of adequate quality: a μCT with adequate resolution and quality can take up to a few hours for each scan. The high time required is due to the fact that more images are normally acquired under different mechanical conditions (loading and unloading conditions). Moreover, it is not possible to apply loading conditions with physiological speeds but it is only possible to do a quasi-static stepwise loading. In fact, the vertebral body, the discs, and the spinal segment as a whole are viscoelastic structures that have a time-dependent behaviour and can therefore show creep and stress relaxation when constant loads or deformations are applied (Fig. 18). Preconditioning is usually used to ensure the testing set-up to settle, and to reduce the effects of viscoelasticity [25].

Furthermore, throughout the acquisition and execution of the mechanical tests, the non-fixed biological specimens must be kept hydrated (for example with gauzes soaked in saline solution) otherwise they could be damaged and invalidate the results.

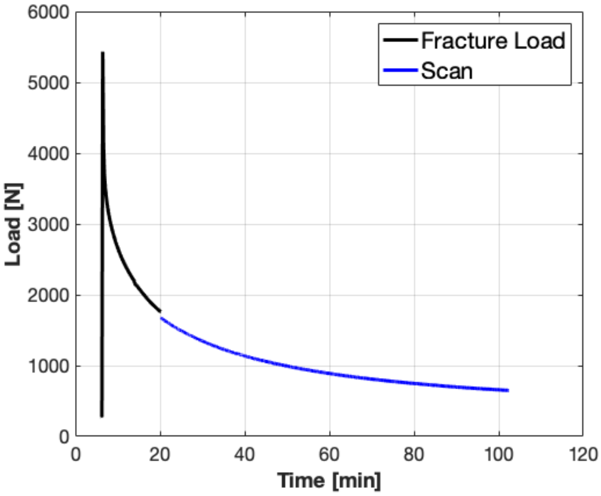

Figure 18: Relaxation curve after compressive load (N) application on two adjacent vertebrae

During the past years, many research groups used the DVC technique in order to compute volumetric strains inside a vertebral body. Hardisty and Whyne were the first to apply the DVC technique in an animal model [43]. They developed and validated an image registration method to spatially resolve strain in a whole rat vertebra using µCT images. Rat models are commonly used in scientific research but, as mentioned earlier, animal anatomy is different from that of humans. First of all, rat vertebrae have sensible different vertebral dimensions that vary more between vertebral levels than they do in the human spine [26]. Rat vertebrae have more lengthen vertebral bodies and different cortical/trabecular bone ratio considering the greater cortical shell thickness relative to the amount of trabecular bone as compared to human vertebrae [7]. From a mechanical point of view, rat vertebrae are slender and this makes them more flexible than human ones. But since the morphology in the axial plane is similar, these specimens are an appropriate surrogate for modelling the axial and shear load of the human spine [26]. In 2016 Tozzi et al. investigate the strain field inside porcine vertebral bodies under progressive compressive axial loading (Fig. 19) up to failure, by using a local DVC approach (DaVis-DC) [39]. The internal strain distribution helped in predicting high-strain concentrations inside the vertebrae and therefore, the regions of failure.

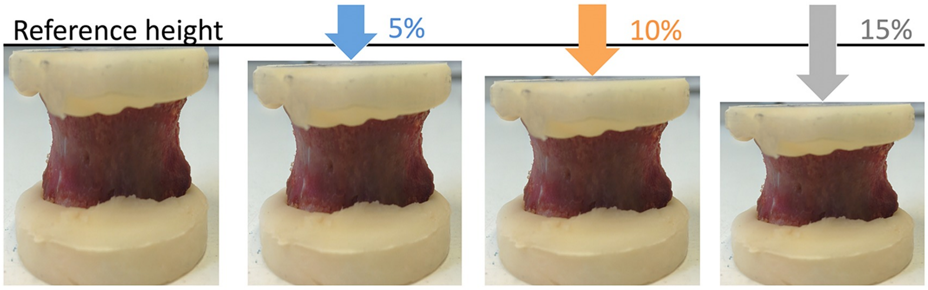

Figure 19: Whole porcine vertebra. Initial reference state and the compressive steps are shown [39].

DVC was also applied to a porcine vertebra by Palanca et al. [46] to compute local strains in natural and augmented (Acrylic vertebroplasty cement, Mendec Spine, Tecres, Italy) vertebrae. They quantified the measurement uncertainties of both a local (DaVis-DC) and a global (BoneDVC) DVC approach, investigating the variability between the specimens. Results showed that the strain measurement uncertainties of DVC were adequate to investigate strain distribution associated with physiological loads and bone failure.

However, porcine models have few limitations. In particular, due to the different posture of the pigs (quadrupeds) and the humans (bipeds), the kyphotic and lordotic curvatures are different in the two species [51]. Moreover, human spine has relatively larger caudal vertebral bodies to sustain the higher longitudinal loads, as well as larger intervertebral discs in the lumbar region [51]. In order to use the results obtained on porcine vertebra, it must be taken into account that animals used for research purpose are usually not fully grown thus, the growth plates, weaker regions of cartilage and calcified cartilage where strain concentrations are often localised, are still open in the vertebral bodies. However, animal models are commonly used in scientific research to define new procedures primarily for ethical choices.

The first ones to use human specimens were Hussein and her colleagues. They used the DVC to obtain quantitative data on full-field deformation of one whole human vertebra, supporting that this could help in predicting bone failure and in studying the effects of a particular disease on failure mechanics in bone [23]. Figure 20 reports the workflow they followed: A) specimen scan via μCT; B) generation of vertebral body's surfaces; C) generation of an 8-noded hexahedrons mesh; D) computation of strains from the displacement data [23].

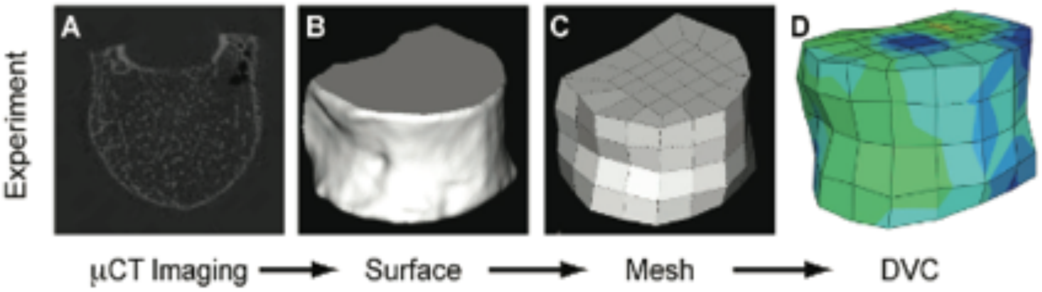

Figure 20: Generation of the 3D irregularly shaped volume for DVC analyses of a whole vertebral body [23]

For both animal and this human model, a great limitation lies in the fact that only one vertebra was characterized and not a multi-vertebra segment. In fact, Hussein et al. [9] demonstrated how deformation and failure patterns are different in the presence of the intervertebral discs.

Human spine segments consisting of three intact vertebrae were first used by Jackman et al. [52]. Specimens were tested in axial compression or axial compression with anterior flexion up to failure. Through the DVC technique (same method used in [23]), the displacement field within the middle vertebra was computed. Then, these displacements were compared to those simulated by qCT-based Finite Element Analyses of the same vertebra.

The study of the full-field strain distribution in pathological conditions (spinal metastases) was for the first time evaluated in 2012 by Hardisty et al. [7]. They used an animal model, rat spinal motion segment: metastases were induced by injecting MT-1 human breast cancer cells under general anaesthesia in five female rats. Then rats were monitored until the presence of the tumour was verified (2–3 weeks post injection) and then sacrificed. The tumour-bearing vertebral motion segments was matched with a healthy vertebral motion segments from similarly aged control animals. They both were tested under axial compression with the same loading conditions. Image registration [43] was used to measure strain in each vertebra under load and it highlight that the compressive strain in the metastatic vertebrae were an average of two times more than the control vertebrae (Fig. 21) [7]. In addition to the quantitative aspect, image registration is also able to qualitatively demonstrate the effects of lytic-metastatic involvement. Strain concentrations in the metastatic vertebra were found adjacent to the dorsal vertebral body wall, aligned with the areas compromised by the lytic lesions and consistent with clinical burst fracture patterns (failure of the posterior wall of the vertebral body) [7].

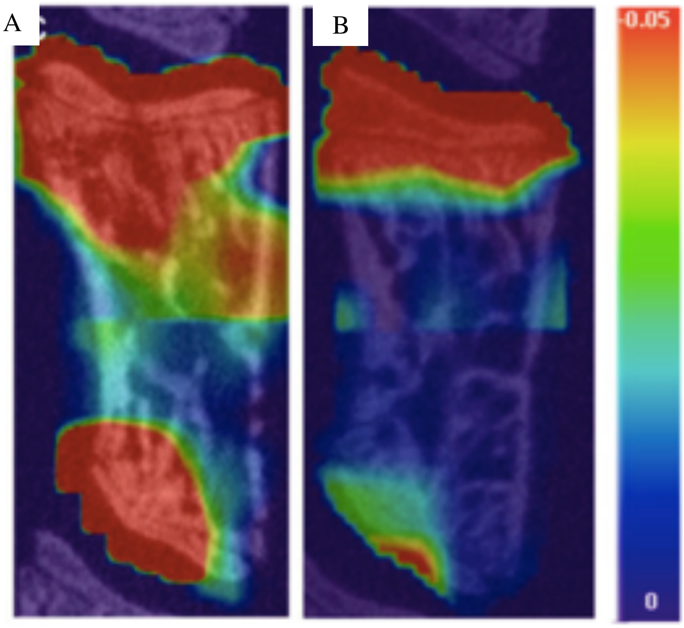

Figure 21: Central sagittal sections of the vertebra with tumours (A) and the control vertebra (B) in the unloaded configuration overlaid with axial strain measured by image registration [7].

In 2020, Palanca et al. [53] used DVC to evaluate the effects of artificial bone lesions within the vertebral body by comparing the 3D strain field before and after the lesion formation. They tested intact porcine spines in compression inside a μCT scanner. Then, lytic metastases were simulated as holes involving the cortical shell in the anterior or later middle portion of the vertebra (Fig. 22). The artificial lesions had effects on the strain distribution within the vertebra reducing the bone mechanical properties, leading the vertebral body to failure.

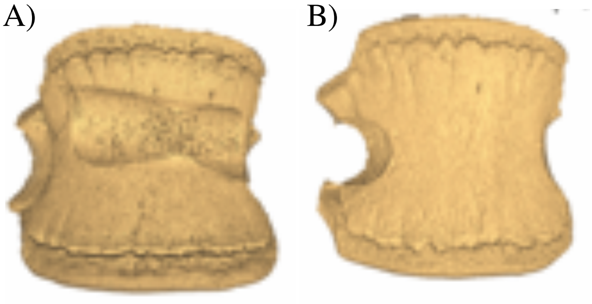

Figure 22: Artificial lesions in the anterior (A) or lateral (B) middle portion of the middle [53].

To the author's knowledge, to date, Hardisty et al [7] is the only study that compared the strain distribution on a metastatic and a healthy vertebrae (in rats). However, these vertebrae belonged to two different donors. To date, DVC has never been applied on human spinal segments consisting of more than 3 vertebrae. They would allow us to compare the strain distributions within two adjacent vertebrae considering one as the metastatic vertebra and one as the control vertebra (healthy or with an irrelevant pathological condition). Moreover, DVC has never been applied on human spinal segments with actual metastases. The simulation of the metastatic condition on animal models is often an ethical choice for setting the procedure, but it does not provide any clinical evidence. To implement the DVC technique in the clinical practice, it is necessary to evaluate the effects of actual metastases on human vertebrae.

Considering the potential of this method, the results obtained from an application of the DVC on human spinal segments with actual metastases, could also be used for the validation of FE models for the prediction of the behaviour and mechanical properties of vertebrae with both actual or simulated metastases, to date performed only using animal models [54].

1.4.4 FE-modelling

In vitro tests allow to evaluate the mechanical properties of the specimens only in some loading conditions based on the experimental set-up that is available. Furthermore, *in vitro* failure tests allow us to experiment only one loading condition, once, on the same specimen. So, since their first development in the 1950s, numerical models (mostly finite element (FE) models) have been immediately applied in the biomechanics of the spine. These *in silico* models introduced the possibility of simulating a multiplicity of clinical situations, and also repeating the same experiment a limitless number of times on the same model, changing the parameters and evaluating their effects on vertebral strains. Indeed, the FE method enables parametric representation of complex geometric and material property distributions of the metastatic spine [12] that can be eventually modified to reflect any condition, physiological (Fig. 23) or not (Fig. 24). The advantage is that virtual specimens cannot be overloaded or damaged and also, they reduce our dependence on animal and cadaveric experiments [55].

Nevertheless, to be used as a clinical tool, all of these models must be validated. Validation is an extremely difficult process: mechanical properties estimated by the FE model need to agree with the data recorded on the specimens during *in vitro* experimental mechanical tests with the same loading and boundary conditions. The difficulty in model validation increases also due to the unavoidable, and often significant, physiological variation among individuals and then, among specimens [55].

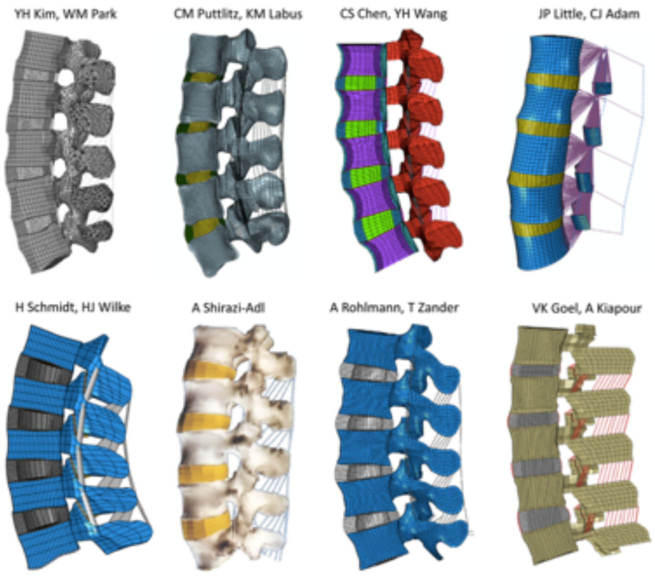

Figure 23 : FE models of intact L1-5 lumbar spine [56]

Initially, FE models of the spine were generated with reference to a generic or average anatomy [57], [58] obtained via anatomical atlas. These models were used to draw generic or average conclusions [58]. Then, to be clinically relevant, for patient assessment, pre- and inter-operative planning [55], FE models need to be more specific for each single patient. Subject-specific FE analysis requires the generation of 3D FE meshes of the bone segments from diagnostic data collected, also *in vivo*, using computed tomography (CT) [55], [58], or quantitative computed tomography (Q-CT) [6], [52] or micro-computed tomography (μCT) (only for small rodents) [12], [59]. Soft tissues morphology can be obtained via magnetic resonance imaging (MRI) or ultrasound [60]. Starting from the CT data the attenuation coefficient of the bone tissue is used to evaluate the apparent bone density (ρ_{app}) of each voxel. Then it can be related to the Young's modulus and the strength of each element through many available empirical relationships. As regarding metastatic vertebrae modelling, lytic metastases can be modelled as a holes in the vertebral volume using empirical relationships to characterize bone as a porous material (Fig.24) [59]. Otherwise blastic and lytic metastases can be modelled by using the same empirical relationships of bone tissue [6].

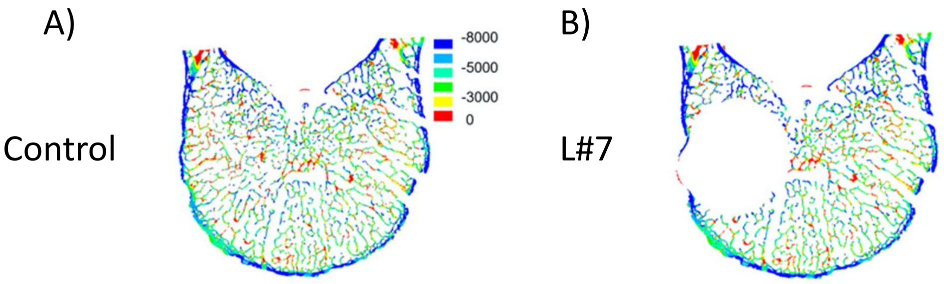

Figure 24 : minimum principal strain distribution (in με) along the mid-cross-section of the control model (A) against the models with single simulated lesions of 12% VB placed in the lateral right (L#7) (B) [59].

When healthy bone is described as a porous material, its materials properties are empirically derived from the apparent bone density [61]:

- Young's Modulus: $\boldsymbol{E} = \boldsymbol{a} * \rho_{app}^{b}$
- Yield compression strength: $\boldsymbol{S} = \boldsymbol{c} * \rho_{app}^{d}$

The constants a, b, c and d are experimentally derived from a calibration curve that converts the grey scale into hydroxyapatite density values.

Nevertheless, a purely elastic approach may not be sufficient to reproduce the complex behaviour exhibited by this biphasic material. In fact, poro-elastic modelling of the spine (poro-elastic solid saturated with a pore fluid), can be also employed, with an increase in the computational cost [57], [61], [62].

FE and Micro-FE modelling has already been used to model intact human vertebral bodies [56], or vertebrae affected by tumours [57] or lytic metastases (actual or simulated) [6], [54], [59], [63]. It has been demonstrated to be a sensitive tool for assessing the strength of bones: principal strains could be used as indicator of fracture risk and to localize regions of potential vertebral trabecular bone failure [6], [57]. Moreover, the behaviour of the vertebra can be estimated for different loadings conditions, and the strain distribution can be computed and mapped (Fig. 25).

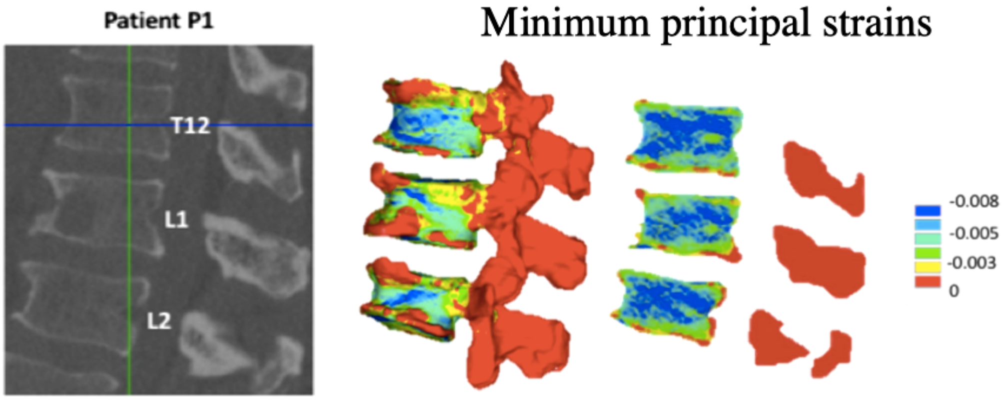

Figure 25: From left to right: side a sagittal section from the qCT image, vertebra with a lytic lesion (L1) and the two adjacent control (T12 and L2); 3D distribution of minimum principal strain; sagittal section [6].

In addition, FE-modelling enables focused investigations into the effects of parameters such as metastasis position, metastasis size [17], [57], [59], material properties, and loading rate [57]. In fact, according to the radiologic assessments of Taneichi et al. [16], tumours size is one of the most important risk factor for vertebral body collapse in metastatically involved spines, followed by the more quick applied load and the lower bone density [12].

FE-modelling has also few limitations. First of all, for static analyses using FE models of the whole spine, researchers commonly simplify the material properties (e.g. constant average Young's modulus mapped to each finite element [64]) while in models of localized spinal structures, more fine-grained values for Young's Modulus can also be used [60]. The use of variable finer Young's Modulus allows to obtain more accurate strain predictions due to the fact that finer changes in the elastic properties of the bone and localized phenomena can be evaluated [64]. On the other hand, Fagan et al. [55] argue that the simplifications of the FE model can often be a strength when there is a lot of uncertainty and variation between individuals, because they allow to fully explore the cause-effect relationships and to eliminate the intrinsic variability of the experimental tests. Model accuracy is also influenced by mesh density: the optimized model is not too little sensitive to localized phenomena (elements too large) and does not require too much time computationally (elements too small) [60]. In fact, mesh elements can have different shapes (e.g. rod (1D), plate (2D), or tetrahedron (3D), etc.) and sizes depending on the resolution needed, on the geometric constraints, and on the available computational power [60]. The fidelity of the results can also be affected by the boundary conditions; they are correlated with the different type of load applied and with the level of simplification (from highly idealized to experimentally matched) used [52].

1.5 Aim

The aim of this study was to evaluate the mechanical behaviour at fracture of human metastatic vertebrae, measuring *in vitro* the internal three-dimensional strain distributions in human spine segments, including metastatic vertebrae and healthy controls, by using Digital Volume Correlation (DVC). The maximum principal and minimum principal strain fields within the vertebral bodies were investigated in the control and metastatic vertebra, to identify the onset fracture location, possible strain patterns typical for the metastatic vertebrae, and regions with focalized strain concentration for better understanding the fracture mechanics in metastatic vertebrae. This study aimed to clarify how the type, the size and position of the metastases can compromise the load-bearing capacity of the vertebra and get spinal instability.

CHAPTER 2: Materials and Methods

2.1 Donors and specimen preparation

All the following procedures were approved by both the ethics committees of Bologna [65] and Sheffield [66], in accordance with the Declaration of Helsinki. Fresh-frozen human spines with vertebrae affected by bone metastases were obtained through an ethically approved international donation program (Anatomy Gift Registry, USA). The spines were selected (same inclusion criteria used in [10]), stored at -30°C and then defrosted in the fridge before testing. In order to keep the specimen hydrated during the test, they were wrapped with gauzes soaked in saline solution. Donors were adults, males and females of different ages, height and weight, affected by different kinds of tumours, with spinal metastases of different types (Table 6).

Table 6: Donors details.

Specimen	**Cancer**	**Sex**	**Age**	**Height (cm)**	**Weight (kg)**	**SINS***	**Control level**	**Metastasis level (s)**	**Type of metastasis**
#766_T2T5	Adrenal	M	81	182	77	4	T3	T4	lytic
#766_T5T8	Adrenal	M	81	182	77	3	T7	T6	lytic
#771_T10L1	Bladder	M	75	172	49	8	T11	T12	mixed
#772_T5T8	Breast	F	82	157	54	3	T7	T6	lytic
#772_L2L5	Breast	F	82	157	54	4	L3	L4	lytic
#775_T12L3	Breast	F	55	165	48	10	L1	L2	lytic
#780_T5T8	Breast	F	51	178	130	7	T7	T6	mixed
#780_T11L2	Breast	F	51	178	130	7	L1	T12	mixed
#781_T6T9	Lung	F	73	175	72	6	T8	T7	mixed
#782_T4T7	Adeno-carcinoma	F	62	157	149	3	T6	T5	lytic
#784_T6T9	Prostate	M	52	172	50	5	T7	T8	mixed

*The SINS was evaluated only based on the radiographic parameters not considering the pain, for which no information was available (SINS maximum value was reduced from 18 to 15)

A series of mechanical tests were performed on the mentioned sample before the analysis reported in this work. A brief description of the methods and findings, obtained in the previous work, was reported as preliminary outcomes for the development of the current study. For each spine, quantitative computed tomography (qCT, AquilonOne, Toshiba, Japan) images were acquired following an optimized clinical procedure for scanning the spine (voltage: 120 kVp, current: 200 mA, slice thickness: 1mm, in-plane resolution: around 0.45 mm). Calibration was performed using a European Spine Phantom (ESP) [67]. The overall condition of the spine, the type, size and position of the metastasis and the spinal instability neoplastic score (SINS) [3] were evaluated by two expert clinicians [53], considering only the radiographic parameters. As the pain was not measured, the maximum of the SINS scale was reduced from 18 to 15. The size of the metastasis was obtained by a manual segmentation of the qCT images (Table 7).

Table 7: Size of the vertebra (volume and mean cross-section) and volume of the metastasis, obtained manually on Amira.

Specimen	Volume of the vertebra (mm^3)	Volume of the metastasis (mm^3)	Mean cross-section area of the metastasis (mm^2)
#766_T2T5	18460	2995	738
#771_T10L1	34538	1366	1191
#772_T5T8	11593	600	552
#772_L2L5	25577	5206	882
#775_T12L3	25331	3555	974
#780_T5T8	13995	4331	636
#780_T11L2	27481	5283	1018
#781_T6T9	15930	5317	797
#782_T4T7	13638	845	682
#784_T6T9	21412	9960	973

Thoracic and/or lumbar multi-vertebrae segments were extracted from the spines. Each specimen included a healthy vertebra (later referred to as control), a metastatic one and other two at the extremities. It is reasonable considering that the control and the metastatic vertebrae, being adjacent, were subjected to similar loads. Thus, this assumption allows us to directly compare the strain field of the two vertebrae and to evaluate the possible effect of the presence of the metastases.

Specimens were prepared to be analysed with the Digital Image Correlation (Aramis Adjustable 12M, GOM, Brunswick, Germany) in a previous study. Briefly, the endplates of the two outermost vertebrae of each specimen were embedded in poly-methyl-methacrylate (PMMA) to be fixed in the testing machine with the help of one, or more, screws. All the soft tissues, except for the intervertebral discs and the posterior ligaments, were removed using surgical tools without damaging the vertebral bodies. The external surface of few spine segments was stained with a water-based paint of methylene blue; a white paint (Q250201 Bianco Opaco, Chrèon, Italy) was used for the speckle dots (Fig. 26). Other specimens were prepared only with the white speckle pattern without any background. Four different physiological loading conditions were tested using a uniaxial testing machine (Italsigma frame, Instron 25kN load cell, Instron 8500): flexion, right and left lateral bending, and pure compression [36]. The DIC technique provided the strain field on the external surface of the specimens. The analysis of the maximum principal and minimum principal strains and of the maximum shear strains showed the different mechanical behaviours in the metastatic and control vertebrae and, between lytic, blastic or mixed-metastatic vertebrae. Results showed that the SINS poorly correlated with the mechanical properties. However, the metastatic features, as the location and size of the lesions, did affect the spinal stability, thus, their integration in the current clinical scoring system, could improve the characterization of the metastatic vertebrae.

Figure 26: Specimen prepared for the application of the DIC with a white on blue random pattern.

2.1.1 Specimen preparation for the DVC analysis

In this work, the focus moved to the strain analysis within the vertebral body. A global Digital Volume Correlation (DVC) approach was applied to the same sample in order to explore the behaviour of metastatic vertebrae up to fracture. Apparent axial compressive loads were applied within the loading device (later referred as jig) where large displacements were not allowed.

In fact, to get the specimen into the jig, it was necessary to remove the posterior elements, by cutting the specimens in the middle of the vertebral arch in the cranio-caudal direction (Figure 27). The absence of the posterior elements obviously alters the physiological kinematics of the spine and therefore, the transmission and distribution of loads and strains.

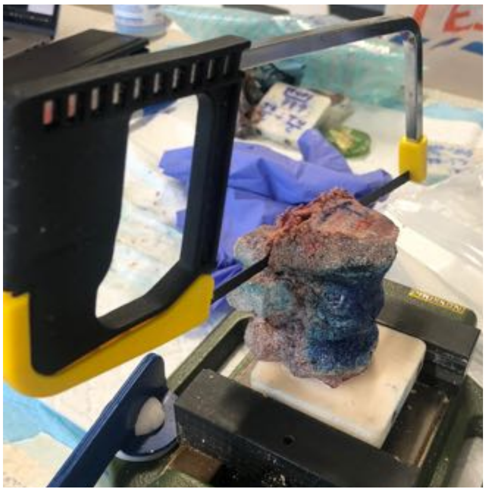

Figure 27: Removal of the posterior elements.

Part of the PMMA at the extremities were removed to fit the specimens in the jig. In some specimens, the embedding material was completely removed; in other cases, it was cut, to reduce its size. Then, the embedding material was recreated using a custom-made aluminium potter which guarantees to obtain the right diameter to fit the jig and, the co-axiality and the parallelism of the embedding bases (Fig. 28). The embedding material was created using the Technovit® 4071 (Kulzer Technique, Wehrheim, Germany) cement, a fast-curing two-component inclusion resin based on highly cross-linked methyl-methacrylate in the form of powder and a liquid monomer activator.

The preparation of the embedding material (in the potter cap) was done as described in the following steps:

- Sprinkle the release spray on the potter cap to facilitate the detachment.
- Place the specimen centrally in the cap.
- Mix the two components of the cement pouring the liquid into the powder and mix well. We used them in a ratio of 2:1 (~16 g of powder and ~8 of liquid).
- Pour the cement trying to create a layer superior to the old pot, if present.
- Leave in the chemical hood for at least 20-30 minutes.

Similar procedure, but using the other side of the potter, was applied to prepare the embedding base on the opposite side. To remove the specimens from the potter without damaging it, a screw is used to move the potter bottom and push the specimen out of the potter.

Figure 28: A) Specimen during the embedding procedure. B) Specimen embedded in PMMA.

2.2 *In situ* mechanical tests

Acquisition and mechanical test were performed at the Medical School (University of Sheffield, UK) by Dr. Marco Palanca, co-supervisor of this project.

2.2.1 Imaging Protocol

A micro-CT (µCT) scanner (VivaCT80, Scanco Medical, Bruttisellen, Switzerland) was used to scan each specimen in pure compression step-wise loadings (Fig. 29). The µCT parameters of acquisition were based on a previous study in porcine vertebrae [53]: current 114 µA, voltage 70 kVp, integration time 300 ms, power 8 W, isotropic voxel size 39 µm. To reduce the beam hardening artefact a polynomial correction based on scans of a wedge phantom with 1200 mg/cm^3 of hydroxyapatite (HA) was used during the reconstruction step. Before each scan, a pre-calibration was performed to quantify the black-field and bright-field noise in the μCT chamber and correct it. Afterwards, the jig was inserted into the μCT chamber. A scout view was performed in order to choose the whole area of interest, including both the metastatic and the control vertebra. Each scan took approximately 1,5-2 hours.

Figure 29: VivaCT 80 microCT scanner.

2.3.2 Experimental mechanical tests

Specimens were tested in pure compression inside a custom-built jig, consisting of a Plexiglas tube with low X-Rays attenuation (Fig. 30). The jig is a loading device, with a screw-lead screw system, manually activated by means of a torque wrench. The loading system is made of a compressive force transducer (load cell). A Linear Variable Displacement Transducer (LVDT) measures the linear axial displacement of the specimen. In this work, we used a load cell with a nominal full-range force of 10 kN (HBM, Germany) to apply the compressive load and 20 mm LVDT (HBM, Germany) to measure the axial deformation of the specimens. Before the application of the compressive loads, the load cell and the LVDT were zeroed. Each loading condition was applied manually outside the μCT chamber by means of a torque wrench (Fig. 31). Ten cycles of preconditioning from 50 to 300 N were applied before each test. In order to avoid imaging artefacts as a result of stress-relaxation, the specimen relaxed for 15 minutes to stabilize the applied load. After the relaxation, the loading device was inserted into the μCT scanner for the scan.

During the loading and scanning phases, the load measured by the load cell (N) and displacement measured by the LVDT (mm) were low-pass filtered, amplified (Spider8, HBM, Germany) and registered (acquisition rate of 50 Hz during the loading phases and acquisition rate of 1 Hz during the scans) using the "Catman Easy" software (HBM, Germany).

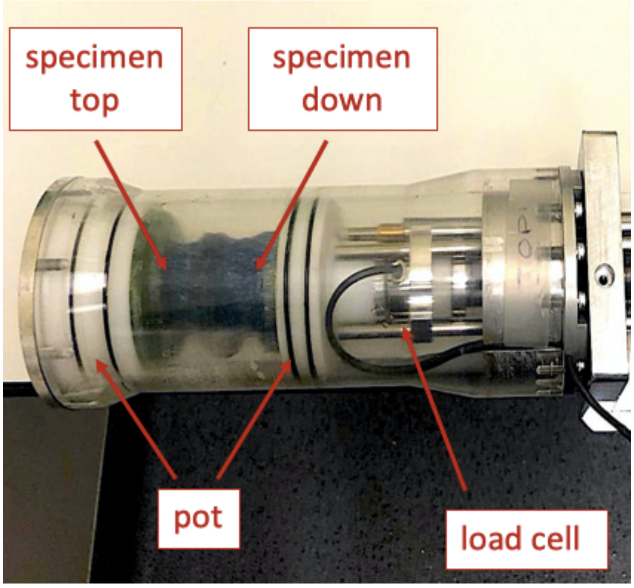

Figure 30: Specimen (blue) inside the loading jig with the 10kN load cell.

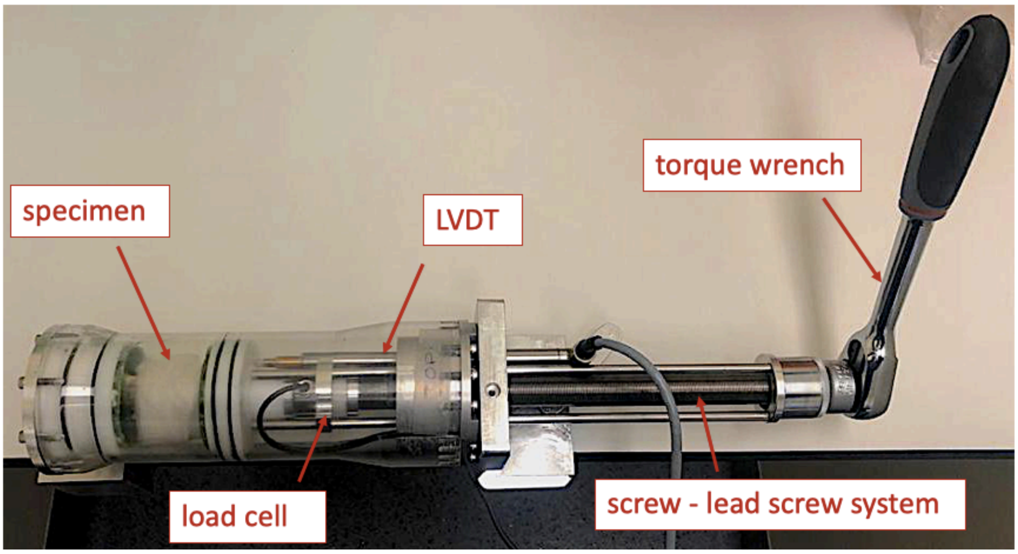

Figure 31: Manual loading application, by means of the torque wrench, on the specimen inside the loading jig with the screw-lead screw system, the 10kN load cell and the 20mm LVDT.

Each specimen was scanned in the μCT according to the following loading protocol:

- "Scan1": scan of the entire specimen in preloaded (approximately 50 N) condition;
- "Scan2": scan of the middle portion of the metastatic vertebra that included the metastasis in preloaded (approximately 50 N) condition;
- "Scan3": scan of the entire specimen in loaded Physiological load condition (see below details);
- "Scan4": scan of the entire specimen in loaded (3x Physiological load) condition;
- "Scan5": scan of the entire specimen after failure.

The 50 N preload was used to keep the specimen stationary and avoid moving artefacts during the scans in the unloaded conditions. "Scan1" and "Scan2" were the unloaded scans. They were used to evaluate the DVC strain measurement uncertainties.

Physiological loads were defined following the protocol reported in [36] during the DIC measurements performed before this study. Briefly, for each specimen, loads were defined in function of the strains reached on the surface of the control vertebra. Palanca et al. [36] chose strains between -3500 and -2500 με as a target because it corresponds to the strain levels measured during physiological motor tasks [39] in order to remain in elastic regime without damaging the bone.

In the last loading condition, the specimen was loaded until the failure occurred. "Scan5" was used to compute the strain field, in the control and metastatic vertebra.

Table 8 reports the applied load for each specimen. The trend of the compressive loads applied to one of the specimen (#780_T5T8) is reported in Figure 32.

Table 8: Magnitude of the applied loads for each loading step for each specimen

Loading Steps	Physiological Load (N)	3xLoad (N)	Fracture (N)
#766_T2T5	1000	3000	4000
#766_T5T8	2385	The jig broke at 6000 N	
#771_T10L1	720	NA	1998
#772_T5T8	810	NA	1450
#772_L2L5	196	589	1800
#775_T12L3	600	NA	1100
#780_T5T8	1150	3450	5000
#780_T11L2	200	630	6500
#781_T6T9	850	NA	1200
#782_T4T7	1300	NA	2700
#784_T6T9	330	927	4563

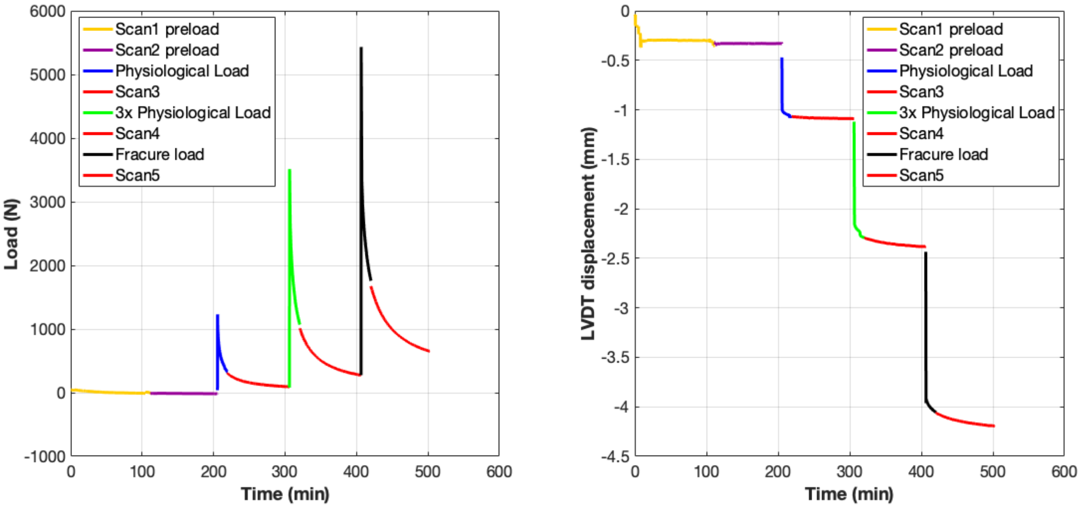

Figure 32: Description of the compressive loads applied to one specimen (#780_T5T8).

2.3 BoneDVC

The μCT images, acquired in step-wise loading, allowed us to study the mechanical behaviour of the specimens and locally characterize the entire metastatic vertebra, by applying a Digital Volume Correlation (DVC) algorithm. BoneDVC is a global DVC approach, which is the combination of an elastic region software ShIRT (Sheffield Image Registration Toolkit) and a Finite Element (FE) software package (Ansys v.14.0, ANSYS, Inc., Canonsburg, PA), used to measure the displacement and strain field within the bones. BoneDVC focuses on the identification of the optimal displacement field to be applied to the nodes of a grid superimposed to the fixed (undeformed) and moved (deformed) images, in order to minimise the difference between the fixed and the registered moved image. The 3D homogeneous grid of discrete point with selectable nodal spacing (NS) can be defined with respect to the two images [47]. Briefly, the displacement field is evaluated at each node of the grid by solving the elastic registration equation [41]. For small displacement, the displacement functions u(x, y, z), v(x, y, z), and w(x, y, z) are computed mapping the fixed image f(x, y, z) into the moving image m(x', y', z'), considering an additional intensity displacement function, *c(x, y, z),* to account for potential changes in the grey levels [41]:

$$f - m \approx \frac{1}{2}\left(u\left(\frac{\partial f}{\partial x} + \frac{\partial m}{\partial x}\right) + v\left(\frac{\partial f}{\partial y} + \frac{\partial m}{\partial y}\right) + w\left(\frac{\partial f}{\partial z} + \frac{\partial m}{\partial z}\right) - c(f + m)\right) \tag{3}$$

Then, the displacements in each node are interpolated with a trilinear function to compute the 3D full-field of displacement in each point of the moved image [41], [47]:

$$\begin{cases} u = \sum_i a_{xi}\varphi_i \\ v = \sum_i a_{yi}\varphi_i \\ w = \sum_i a_{zi}\varphi_i \end{cases} \tag{4}$$

Then, the strain field is computed by differentiating the displacement field, using Ansys (Fig. 33): the 3D grid of discrete point is converted into an eight-noded hexahedrons mesh, the model is solved linearly, and the six strain components are computed in each node using the computed displacement as kinematic boundary conditions [47].

The region where the elastic registration takes place is selected by the application of the DVC mask: each voxel, of the reference and model images, that has a grey-value above the mask threshold value is considered included in the region of interest. In order to analyse the displacement and the strain distribution over the whole volume of the vertebra, or within a restricted area, the voxel detection mask, defined with respect to the reference image, can be used. In fact, the voxel detection process works as a selection of those grid nodes that fall inside the mask and therefore, removes all elements of the mesh with the nodes outside the mask.

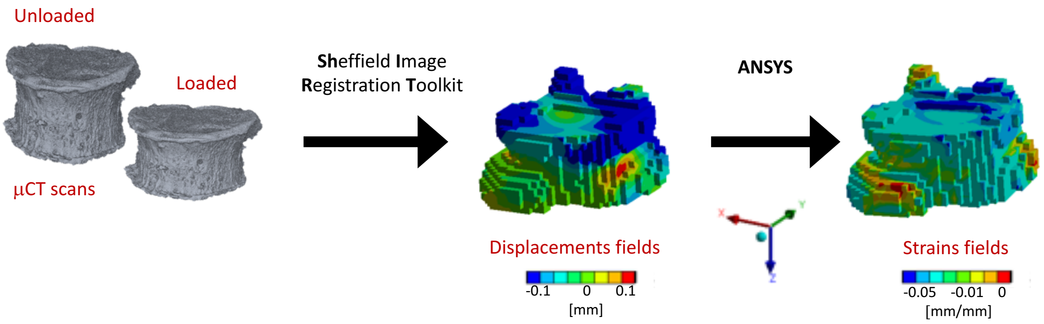

Figure 33: BoneDVC functioning: the outputs of the registration are the axial displacements (x-axis). The strain field is computed by Ansys.

This algorithm has already been tested for several bone structures [41], [45], [46]. Moreover, in 2016 Palanca et al. [46] demonstrated that it was more accurate and precise for strain measurements within the vertebral bodies, than other available DVC local approaches. Thus, the BoneDVC service (https://bonedvc.insigneo.org/dvc/) was used to perform all the strain analyses reported in this work.

It uses as inputs:

- Configuration file: .txt file containing information on the DVC parameters such as the specimen name, the region of interest, the voxel size, the nodal spacing, the mask threshold, and the maximum number of iterations; other optional information can be added, such as the fixed image name, the moved image name and the DVC mask name.
- Fixed Image: the reference image of the undeformed specimen ("Scan1", 8 bit DICOM Multi-slice)
- Moved Image: the model image of the undeformed (zero-strain analyses) or deformed specimen ("Scan2", "Scan3","Scan4" or "Scan5", 8 bit DICOM Multi-slice)
- DVC Mask: an image with value of 255 inside the contour of the region of interest and 0 in the background, used to specify where the registration has to occur (8 bit DICOM Multi-slice).
- VD Mask: an image with value of 255 inside the contour of the vertebra in the reference condition, and 0 in the background, used to select the region of interest (8 bit DICOM Multi-slice).

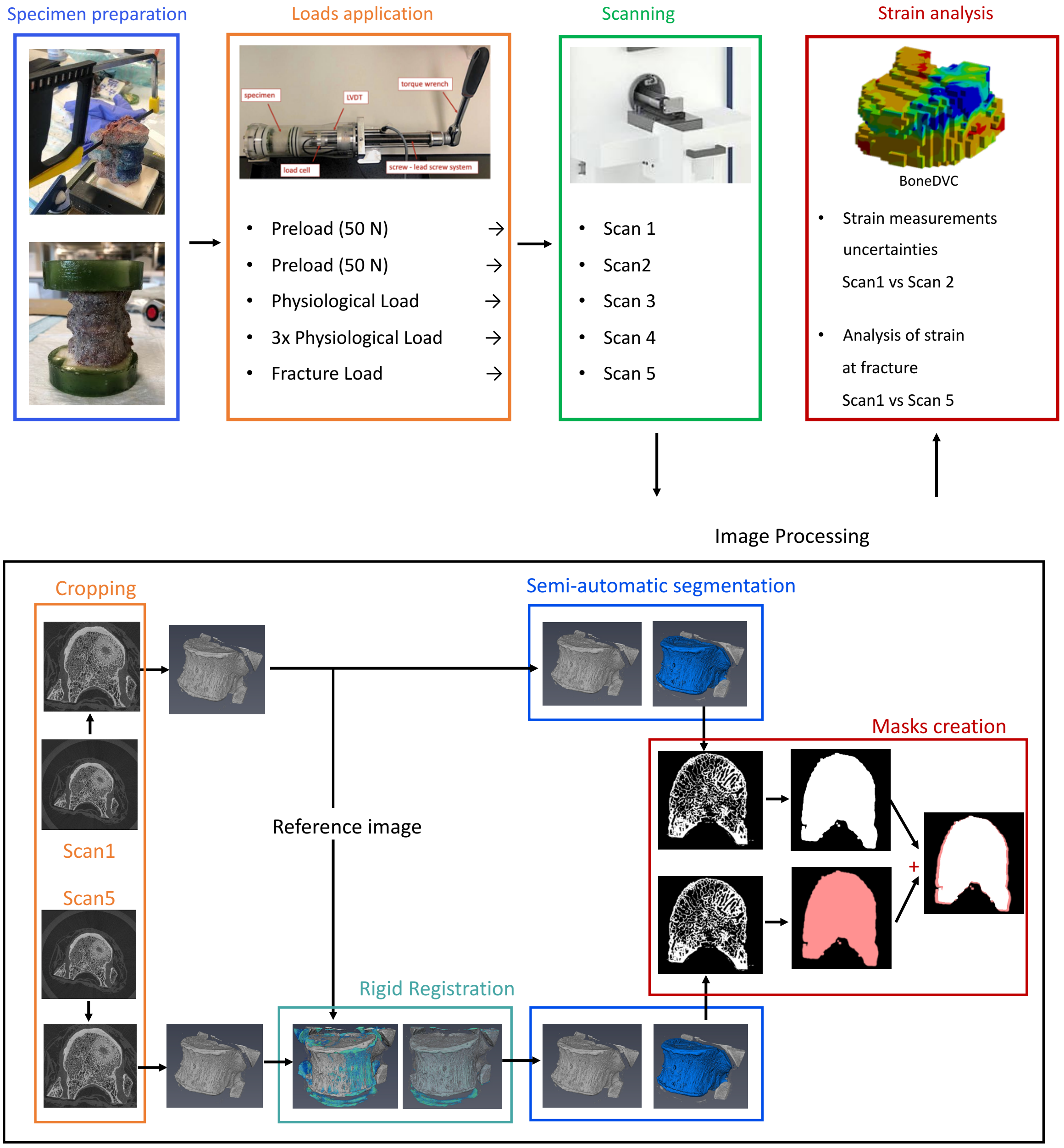

Figure 34: Schematic for the applied workflow.

2.4 Image Processing

The μCT provides a stack of 2D images related to the cross-sections of the scanned specimen. The specimen is positioned between an X-ray source and a detector that acquires hundreds of 2D projections of the specimen from different angles. Then, the X-rays projections of the scanned specimen are used to reconstruct the 3D image of the specimen. In our study, the reconstruction was done using the software provided by the SCANCO Medical MicroCT. Then, the image processing pipeline (Fig. 34) was applied to each specimen, for the control and metastatic vertebra, separately.

2.4.1 Cropping and Rigid Registration

As the μCT acquires a volume larger than the one of interest, the scans are cropped using ImageJ (National Institutes of Health, USA). Only the slices of interest, and so the vertebra of interest, are selected. In order to reduce possible source of uncertainties in the DVC measurement due to the air bubbles (identified by a darker area in the slice (Fig. 35A) that could move in between the scans), a custom-made ImageJ script was used. The voxel grey-levels corresponding to the air bubbles, were replaced by values similar to those of the bone-marrow (Fig. 35B).

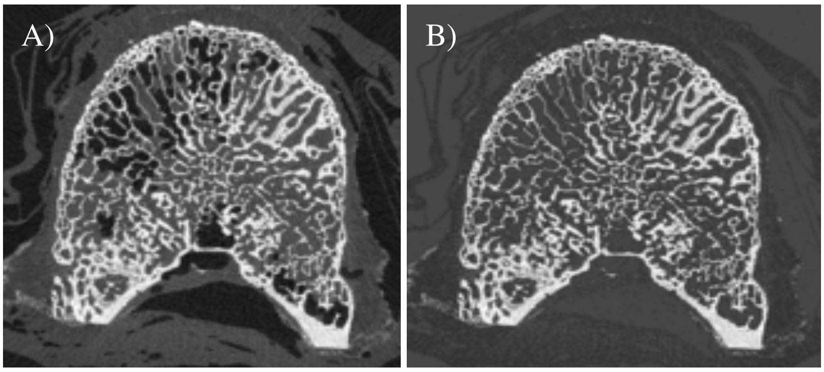

Figure 35: A) Scan before removing air bubbles. B) Same scan after the air bubbles removal.

During the compression loading phase, the vertebrae were subjected to rigid body motions, whose magnitude was related to the state of the intervertebral discs. A rigid image registration of the specimen is necessary to remove the rigid body motions. Through the rigid registration tool (Amira 6.2, Thermo Fisher Scientific), the coordinate system of the moved image is transformed (6 degrees of freedom: 3 translations, 3 rotations) so that it matches with the coordinate system of the reference image (Fig. 36). In our work, we aligned the principal axes of each scan of the same specimen using the "Scan1" (unloaded condition) as the reference image. Once the alignment was completed, the images of the moved and deformed specimen ("Scan3", "Scan4", "Scan5") were cropped (Lancsoz interpolation) against the reference image, in order to have the same dimension of the bounding boxes[3]. In the evaluation of the DVC strain measurement uncertainties the moved image ("Scan2") was aligned to the "Scan1", and the "Scan1" was then cropped against the "Scan2".

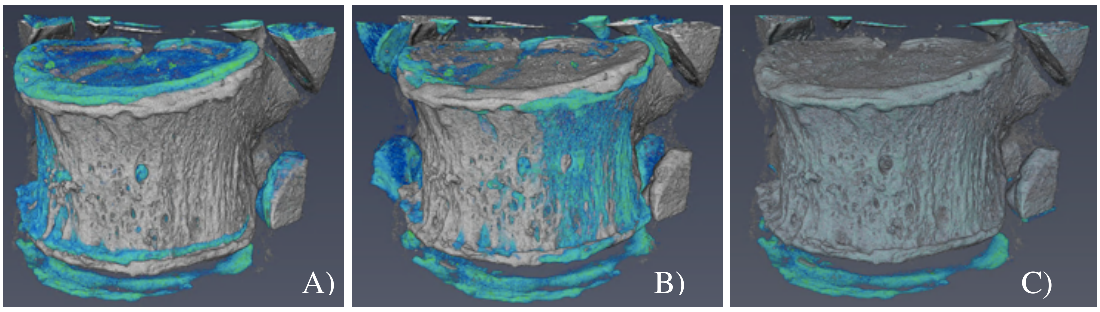

Figure 36: Scan1 (grey) used as the reference image and Scan2 (blue) used as moved image: A) Before the alignment. B) During the alignment. C) After the alignment.

2.4.2 Segmentation and creation of the masks

The μCT records an image over a very large volume (Fig. 37A), including also the wet gauzes positioned around the specimen, the costovertebral joints, and portions of the adjacent vertebrae above and below. A semi-automatic segmentation of each scan was performed, as it was necessary to remove all the elements present in the μCT images that that did not have a mechanical role in the tests performed: adjacent vertebrae, costovertebral joints, wet gauzes, etc. Using the Amira's segmentation tool, the removal was done semi-automatically, by setting a threshold to distinguish between the mineralized and non-mineralized structures. A more precise contouring for specific regions was achieved manually slice-by-slice (Fig. 37B) [68] .

---

[3] Bounding boxe: it is an imaginary box which contains the whole volume of the object of interest.

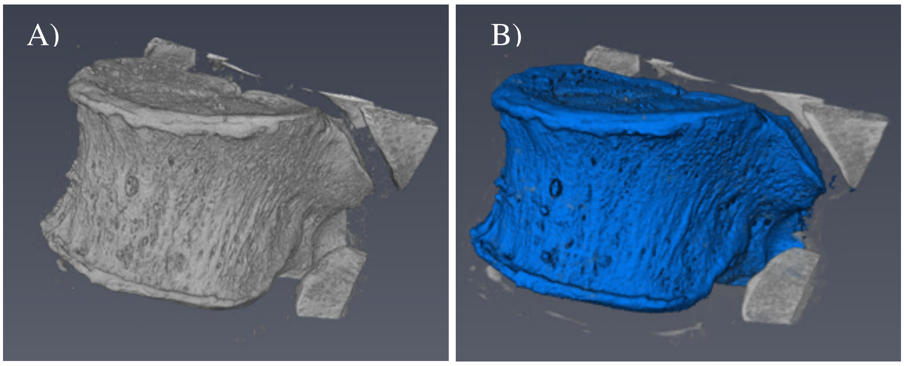

Figure 37: A) Original 3D image (grey). B) Segmented vertebra (blue).

The DICOM multi-slice images obtained after segmentation (Fig. 38A) were used to create both the binary masks[4] for the Voxel Detection (VD) and the DVC on ImageJ. The creation of a binary mask involves: the application of Gaussian 3D filter to reduce the high frequency image noise resulting from the reconstructed μCT image (Fig. 38B); a manual selection of the threshold in order to increase the distinction between the bone tissue and the bone marrow (Fig. 38C); the use of the binary process "Fill Holes", as well as of the dilatation and erosion process as many times as needed, until all the holes within the vertebra are filled (Fig. 38D).

The VD binary mask is created following the procedure described above, while the DVC binary mask is obtained by superimposing the binary mask of the analysed loading condition ("Scan2", "Scan3", "Scan4" or "Scan5") and the binary mask of the "Scan1", that is used as a reference.

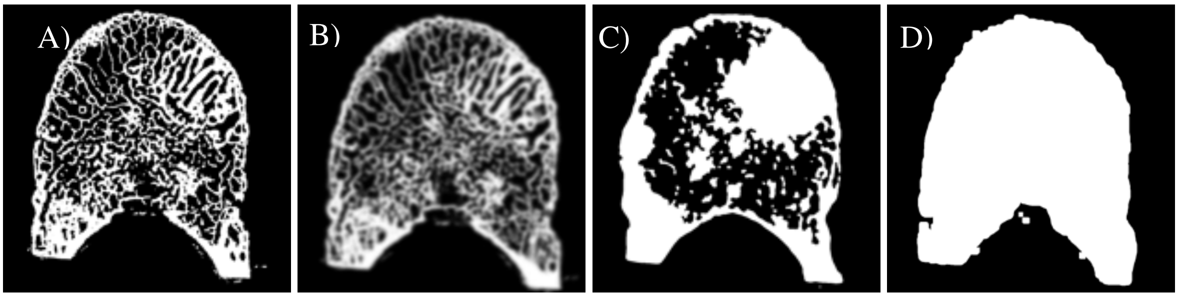

Figure 38: A) Segmented scan. B) Application of the Gaussian Blur 3D filter. C) Selection of the Threshold. D) Binary mask.

---

[4] Binary Mask: an image with value of 1 in the foreground (bone voxels) and 0 in the background (elsewhere)

2.5 Parameters optimization

Accuracy and precision of the DVC method were defined by Liu et al. [48], respectively, as the mean absolute error (MAER) and the standard deviation of the error (SDER). For zero-strain applications, they were quantified as the mean and the standard deviation of the average of the absolute values of the six strain components for each sub-volume of the 3D image (Eq. (1) and Eq. (2), refer to sub-paragraph 1.4.3).

Wide range of accuracy and precision of the measured displacement and strains for different BoneDVC application are reported in previous studies [41], [45], [47]. However, DVC effectiveness on human vertebrae affected by actual metastases has never been tested. Spinal metastases create highly variable trabecular patterns, poor in features, characterized by less dense (lytic metastasis) or denser (blastic metastasis) bone tissue within the vertebra. Considering that the DVC has a slightly better behaviour when applied to structure rich in features, as, for example, trabecular pattern, closer to the ideal condition of 1:1 solid–porosity ratio [45], a quantification of the uncertainties was mandatory in order to choose the optimal parameters for the DVC registration on metastatic specimens.

In this study the following parameters were optimised: nodal spacing (NS), application of the DVC mask, and application of the Voxel Detection (VD) mask. The optimisation of the parameters was performed by registering repeated scans ("Scan1" and "Scan2") of the same specimen in undeformed condition ("zero-strain"), to include both errors related to the image noise, to the registration procedure and the DVC parameters [31], [47]. The systematic and random errors were computed for each component of strain, as well as the MAER and the SDER.

2.5.1 Nodal spacing optimization

The evaluation of the optimal nodal spacing (NS) was performed analysing the repeated scans ("Scan1" and "Scan2") of a single specimen (#780_T5T8). Considering an isotropic voxel size of 39 μm, a series of NS of 10, 30, 50, 70 and 90 voxels was tested. The NS optimization was performed running the BoneDVC algorithm directly on the images without any DVC mask.

The VD mask used was created following the procedure reported in 2.4.2. As expected, the results showed a decrease of the MAER and SDER as the NS increases (Fig. 39) [45]. NS of 50 voxels (isotropic voxel size 39μm) was chosen as optimal as it guaranteed a good compromise between accuracy (1832 με) and precision (1618 με) and spatial resolution [47].

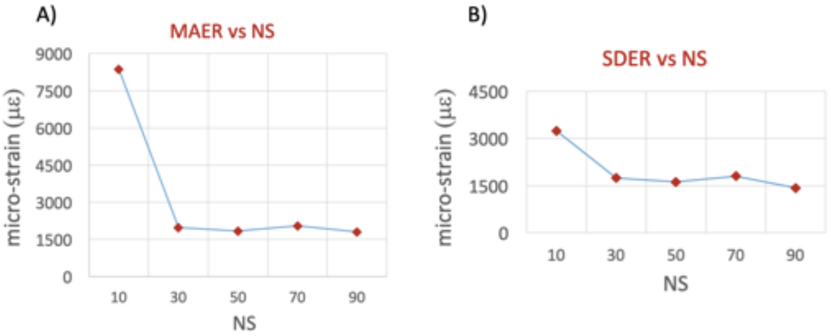

Figure 39: A) MAER vs NS. B) SDER vs NS.

2.5.2 DVC mask optimization

Lytic metastases alter the continuous distribution of the bone tissue and create poor mineralized areas within the vertebral body. This lack of features and of contrast at the lytic metastasis-bone interdigitation may induce larger errors in the elastic registration performed by the BoneDVC approach. The errors were evaluated by testing two different DVC masks on one specimen (#772_T5T8). The first mask (MaskDVC1) included the whole volume of the vertebra and the volume of the metastasis (Fig. 40A). It was created on ImageJ according to the procedure reported in the subparagraph 2.4.2. By contrast, the second mask (MaskDVC2), was created on Amira by selecting manually the volume of the vertebra and the volume of the lytic metastases and considering them as two different materials. The resulting binary mask, created on ImageJ after the segmentation (refer to sub-paragraph 2.4.2), had value of 0 in the background, value of 1 in the lytic metastasis and values of 2 in the vertebra (Fig.40B). By setting, a mask threshold of 2, the DVC excluded both the background and the area with the lytic metastasis from the registration. Results showed that the mask that did not include the volume of the lytic metastasis provided similar values of MAER, but higher values of SDER (Table 9). Considering also the strong operator-dependence in the creation of the MaskDVC2, the use of the MaskDVC1 was preferred as it was more reproducible.

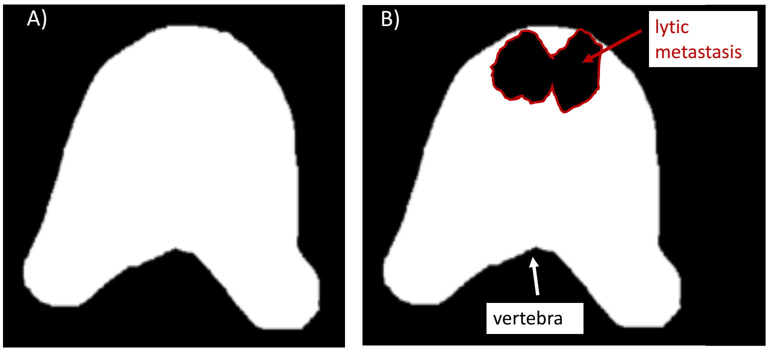

Figure 40: A) MaskDVC1. B) MaskDVC2: vertebra (white) and metastasis (grey).

Table 9: MAER and SDER values for different type of masks before and after the voxel detection.

	MAER (με)		**SDER (με)**	
	Before VD	After VD	Before VD	After VD
MaskDVC1	1199	1511	762	946
MaskDVC2	1217	1673	853	1204

2.5.3 Voxel Detection mask optimization

As the other DVC approaches, the BoneDVC provides larger errors at the edges. In fact, both the systematic and random errors, increased at the boundary of the vertebra in the transition area from the bone tissue, rich of features, to the outer regions, and at the lytic metastasis-bone interdigitation. Thus, the effects of the voxel detection were evaluated through two different VD masks on one specimen (#772_T5T8). The first mask (MaskVD1) included the whole volume of the vertebra and the volume of the metastasis (Fig. 41A). By contrast, the second mask (MaskVD2) was created reducing the size of the MaskVD1 so that it did not include any point on the external surface or on the endplate. Considering a NS of 50 voxels, the MaskVD2 was created reducing by the 50% of the NS (25 voxels), the size of the mask in each direction (x, y, z) so that the most external nodes of the 3D grid were excluded (Fig. 41B).

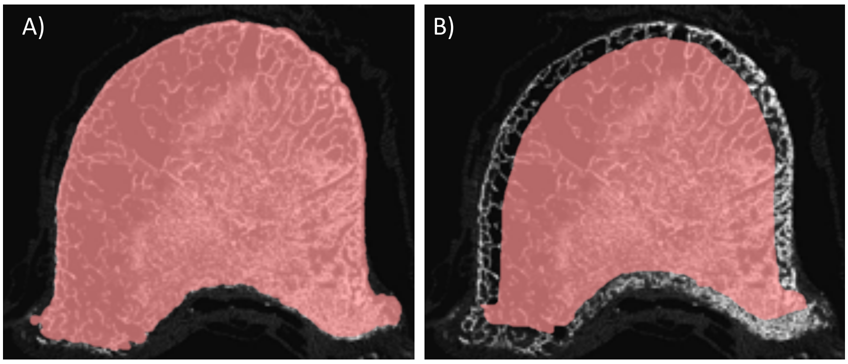

Figure 41: A) MaskVD1 (red) superimposed on the μCT cross-section. B) MaskVD2 (red) superimposed on the μCT cross-section.

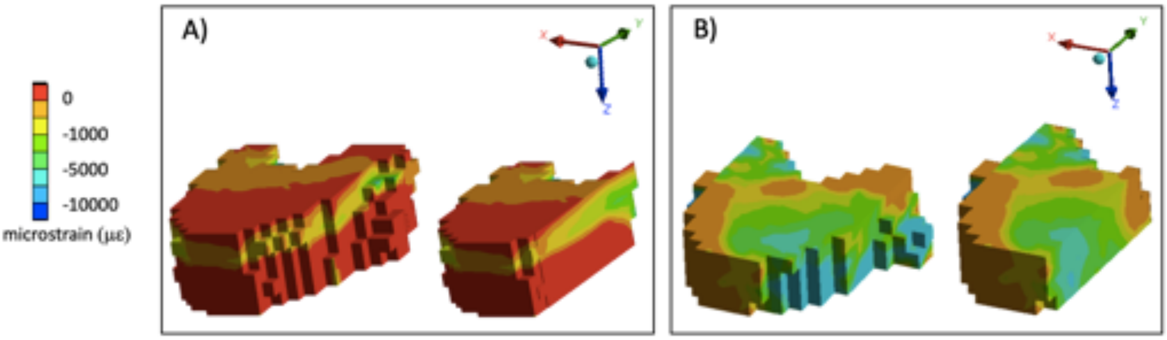

Figure 42: Strain distribution in the shear xz-direction with a nodal spacing of 50 voxels on a mid-height portion of the vertebra using A) MaskVD1 and B) MaskVD2.

As expected, the errors were localised at the boundary regions of the vertebra in both cases (Fig. 42). In particular, the MaskVD2 provided higher values of MAER, but lower values of SDER with respect to the MaskVD1 when tested on one specimen. Considering the great variability over the sample, systematic and random errors were estimated for each specimen with the use of both masks. The two masks showed similar trends (Fig. 43), but as the reduced VD mask, MaskVD2, provided less accurate but more precise results (Table 10), thus its use was preferred. However, to have a comprehensive characterization of the strain field in the whole volume of the vertebrae, including the cortical shell, the boundary regions must be considered. Thus, in the analysis of strains in case of fracture, the MaskVD1 was used.

Table 10: Median MAER and SDER and their standard deviation for two different VD masks over the sample.

	MAER (με)	**SDER (με)**
MaskVD1	1107±336	755±247
MaskVD2	1155±380	564±197

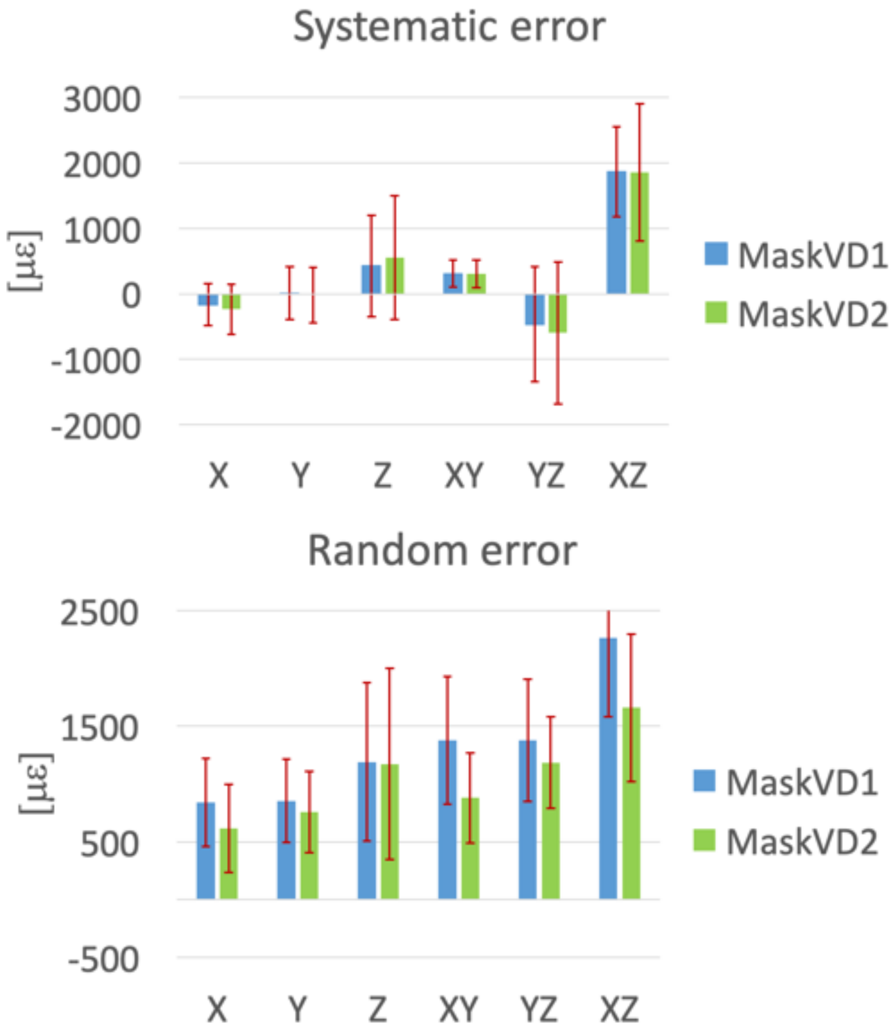

Figure 43: Systematic (Top) and random (Bottom) errors for each component of strain for repeated scans in zero-strains conditions for two different VD masks.

2.6 Metrics

The DVC strain measurement uncertainties over the sample were evaluated analysing the repeated scans, "Scan1" and "Scan2" using the optimized parameters (NS of 50 voxels, MaskDVC1 and MaskVD2). Systematic and random errors for the six components of strains (normal and shear strains) and MAER and SDER were reported in terms of median and standard deviation over the eleven specimens.

In the second part of the study, the spine segments were tested in pure compression step-wise loading, up to fracture. In order to analyse the strain distribution in case of failure of the vertebrae, "Scan5" was registered to the "Scan1" and the strain field was evaluated within the vertebral bodies of the control and metastatic vertebrae. Maximum principal strains (ε_1) and minimum principal strains (ε_3) were computed for nine specimens. Normality of the maximum and minimum principal strain distributions was tested with the one sample Kolmogorov-Smirnov test, while homoscedasticity was tested with the Levene's test (the data did not meet normal distribution and homoscedasticity). Median values of the maximum and minimum principal strains were reported on bar charts to compare the global behaviour of the control and metastatic vertebra, for each spine segment. In order to evaluate if metastatic and control vertebrae of the same spine segment, under the same load, had significantly different behaviours, the respective maximum and minimum principal strains were tested with the Mann-Whitney test. All the statistical analyses were performed using Prism (Prism 9, GraphPad Software, USA) with the level of significance set to 0.05.

Assuming the different strain distributions between metastatic and control vertebrae and that adjacent vertebrae were subjected to similar loading conditions, a Biomechanical Volumetric Ratio (BVR, scalar), consisting in normalizing the strain of the metastatic vertebra with respect to the control one, was defined as a surrogate of the strength of the metastatic vertebra. It was computed as the ratio between the median minimum principal strain of the metastatic vertebra and the control vertebra:

$$BVR = \frac{median\ minimum\ principal\ strain\ in\ the\ metastatic\ vertebra}{median\ minimum\ principal\ strain\ in\ the\ control\ vertebra}$$

Lytic and blastic lesions could be more or less extended inside the vertebral body (the size of the metastases are reported in Table 7, refer to paragraph 2.1). Thus, a compartmental analysis was necessary to locally characterize the behaviour of the vertebral body.

Three-dimensional colour maps of the maximum and minimum principal strains were reported to show regional differences between metastatic and control vertebra, and to localise portions of the vertebra with larger (alarming) strains and identify the onset fracture region. Then, a qualitative investigation of the relationship between the strain fields and the microstructure of the vertebra was performed.

Each vertebral body was divided in three longitudinal (xy-plane) regions of interest (ROIs) using a custom made Matlab script: top, middle and bottom (where the top and the middle ROIs contained the respective cranial and caudal) (Fig. 44A). The effects of the presence of the metastases were evaluated by comparing the minimum principal strains distributions in the control and metastatic vertebra in each ROI. To locally characterize the portion of bone including the metastases, each ROI was divided in 9 sub-regions of interest (subROIs) on the coronal (xz-plane) and sagittal (yz-plane) plane (Fig. 44B): anterior left (AL), anterior (A), anterior right (AR), left (L), central (C), right (R), posterior left (PL), posterior (P), posterior right (PR). The Biomechanical ROI Volumetric Ratio (BVR) was computed also for each subROI and thematic colour maps were used to identify the most critical differences between the metastatic and control vertebra behaviours.

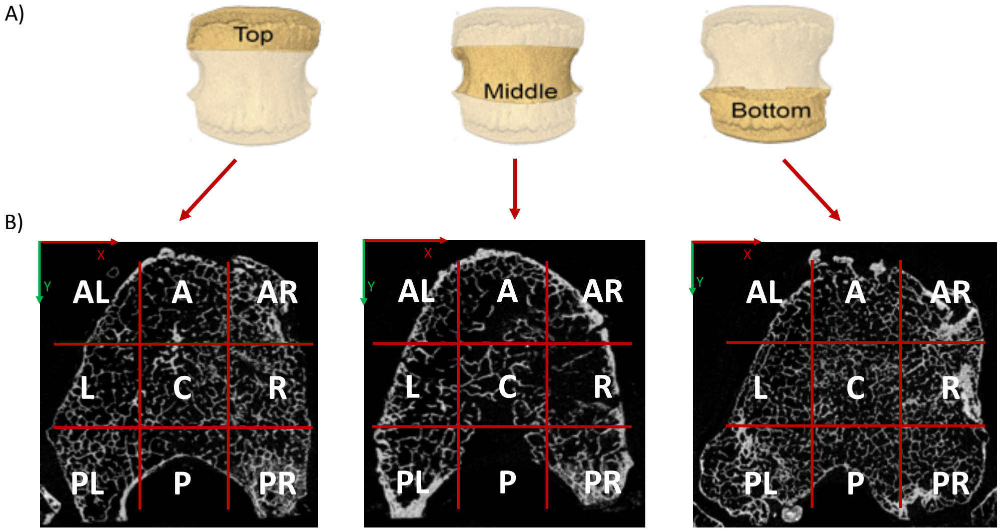

Figure 44: A) The vertebral body is divided in three longitudinal regions of interest (ROI) [53]. B) Each region was divided in nine sub-regions of interest (subROI).

CHAPTER 3: Results

3.1 Strain measurements uncertainties

The strain measurement uncertainties were evaluated for eleven specimens, registering two repeated scans of the middle portion of the metastatic vertebra, in unloaded condition (zero-strain test) using a NS of 50 voxels and the optimised DVC and VD masks.

Systematic and random errors were computed for the six components of strain for each specimen (Table 11 and 12); median values, over the sample, for the six components of strain, were reported in Fig. 45. Larger systematic errors were found in the coronal plane (shear xz-plane) in 9 specimens out of 11. Systematic errors on the other components of strain were an order of magnitude smaller than the one on the coronal plane, and random errors were lower as well. Systematic errors for the maximum and minimum principal strains, over the sample, evaluated using the maskVD2 (refer to sub-paragraph 2.5.3), were 1959 ± 635 με and -1431± 714 με, respectively. Random errors were 1701 ± 613 με and 1149 ± 542 με, respectively. MAER (accuracy) and SDER (precision) values were 1155 ± 380 με and 564 ± 197 με.

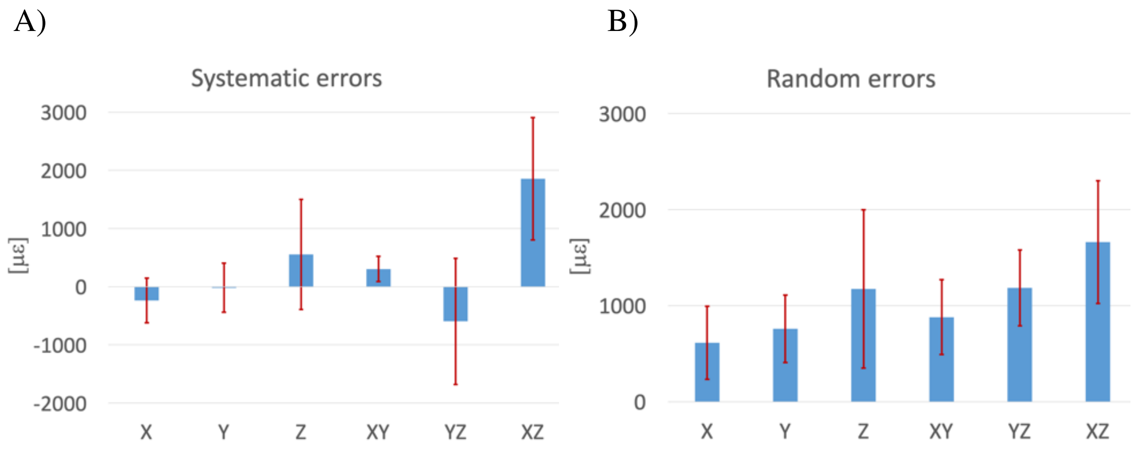

Figure 45: Medians and standard deviations for the six component of the systematic (A) and random (B) errors (με) over the sample (11 specimens).

Table 11: Systematic error for the components and MAER (in $\mu\varepsilon$) values among eleven specimens.

SPECIMEN	Type of metastasis	Component Accuracy						MAER
		X	Y	Z	XY	YZ	XZ	
#766_T4	lytic	-94	-219	1104	284	-1358	2720	1116
#766_T6	lytic	-607	-730	1224	552	-1249	2816	1366
#771_T12	mixed	-237	129	1553	305	-731	1857	1022
#772_L4	lytic	-152	-201	669	485	-2614	1384	1264
#772_T6	lytic	-234	131	-1332	400	-578	3634	1715
#775_L2	lytic	-1235	-777	230	489	-597	1612	1204
#780_T6	mixed	32	709	-480	-143	1674	876	872
#780_T12	mixed	-305	138	2067	139	239	3447	1276
#781_T7	mixed	-63	57	150	105	128	647	295
#782_T5	lytic	-718	-331	469	442	32	3166	1155
#784_T8	mixed	12	-20	556	86	-633	1417	628
MEDIAN		-234	-20	556	305	-597	1857	1155
STD. DEV.		384	422	946	216	1086	1052	380

Table 12: Random error for the components and SDER (in $\mu\varepsilon$) values among eleven specimens.

SPECIMEN	Type of metastasis	Component Precision						SDER
		X	Y	Z	XY	YZ	XZ	
#766_T4	lytic	822	435	1170	861	1249	2469	797
#766_T6	lytic	1025	1175	1755	1135	1123	1540	637
#771_T12	mixed	473	448	2128	675	1184	1900	630
#772_L4	lytic	614	759	1580	1084	1462	1455	504
#772_T6	lytic	1087	1053	3307	1311	1766	2635	656
#775_L2	lytic	1658	1240	1174	1738	1233	2208	840
#780_T6	mixed	593	851	560	879	1297	976	379
#780_T12	mixed	547	432	1689	690	965	1573	515
#781_T7	mixed	294	230	262	356	224	462	118
#782_T5	lytic	881	854	1009	1125	851	2088	553
#784_T8	mixed	522	352	1010	528	870	1661	564
MEDIAN		614	759	1174	879	1184	1661	564
STD. DEV.		381	352	825	390	395	638	197

3.2 Analysis of strains at fracture

3.2.1 Global strain analysis

Eleven specimens were tested up to failure occurred, following the loading protocol reported in paragraph 2.3.2. One of the specimens (#766_T5T8) did not reach the fracture because the jig broke during the loading phases, thus the mechanical test and the acquisition were stopped. Another specimen (#780_T11L2) was corrupted during the image processing and the DVC analysis did not run. Thus, these two specimens were excluded.

The maximum (tensile) and minimum (compressive) principal strain fields were successfully measured in nine specimens by applying the DVC. The principal strain distributions did not meet the normal distribution ($p<0.0001$), thus, medians and standard deviations of the maximum principal (ε_1) and minimum principal strains (ε_3), for each metastatic and control vertebra, and the strain uncertainties of each specimen were reported (Fig. 46-47). Both maximum and minimum principal strain median values resulted statistically different when compared between the metastatic and control vertebra (Mann-Whitney, $p<0.0001$), except for the maximum principal strains of the specimen #784.

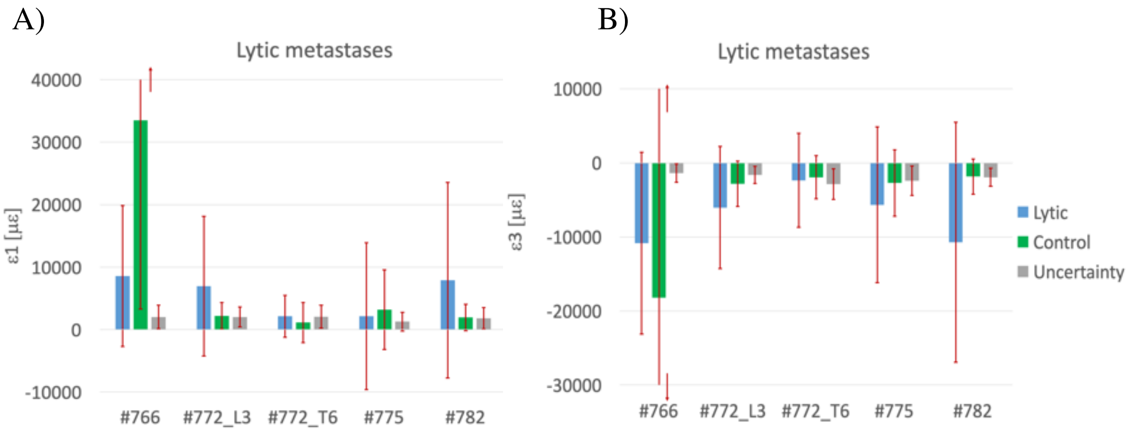

Figure 46: Maximum (A) and minimum principal strains (B) for five lytic-metastatic vertebrae (blue) and for the respective control vertebra (green). For each vertebra, the median and the standard deviation are reported. Additionally, for each vertebra, systematic (bars) and random errors (error bars) of the maximum and minimum principal strains are reported in grey.

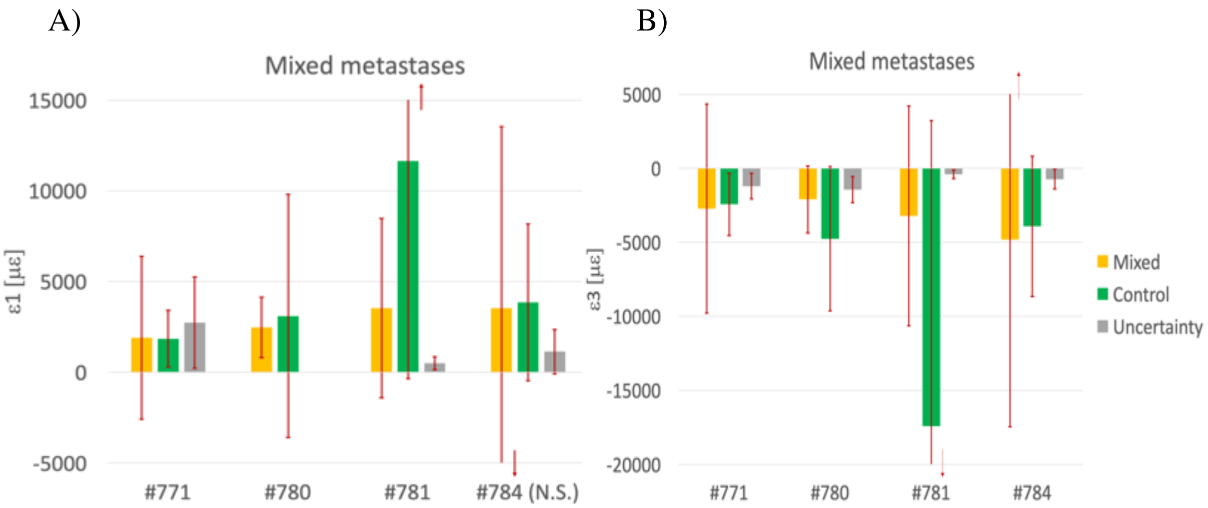

Figure 47: Maximum (A) and minimum principal strains (B) for four mixed-metastatic vertebrae (blue) and for the respective control vertebra (green). For each vertebra, the median and the standard deviation are reported. Additionally, for each vertebra, systematic (bars) and random errors (error bars) of the maximum and minimum principal strains are reported in grey.

In general, in the spine segments including lytic metastases, the metastatic vertebra failed (rather than the healthy control one): the maximum principal strains in the metastatic vertebra were 90-310% higher than the controls and the minimum principal strains were 20-500% higher than the controls. Specimen #766 reached a peak deformation in the control vertebra due to the presence of a large extended osteophyte in the anterior region. By contrast, spine segments with mixed lesions did not show a consistent behaviour in terms of which vertebra failed. In fact, vertebrae with mixed metastases with mainly lytic tissue failed (i.e. #771); vice versa, in case of mixed metastases with mainly blastic tissue, the controls failed (i.e. #780, #781).

In order to evaluate with a scalar indicator, the different deformations experienced by the metastatic and control vertebrae, the Biomechanical Volumetric Ratio (BVR) was calculated as the ratio of the median value of the minimum principal strain between the metastatic and the control vertebra (Table 13). A value of BVR higher than 1 indicates larger strains in the metastatic vertebra, which is less stiff than the control; a value of BVR lower than 1 indicates smaller strain in the metastatic vertebra, which is stiffer than the control. Most specimens affected by lytic metastases had Biomechanical Volumetric Ratio higher than one, which indicated a greater tendency for the metastatic vertebra to fail. Biomechanical Volumetric Ratios in case of mixed metastases were both higher and lower than one, highlighting the variability of the strain patterns in case of mixed lesions.

Table 13: Values of the Biomechanical Volumetric Ratio, volume of the vertebra, volume of the metastasis and the SINS for the nine specimens. The SINS* was evaluated without considering the pain.

Specimen	Type of metastasis	Biomechanical Volumetric Ratio	Volume of the vertebra (mm^3)	Volume of the metastasis (mm^3)	SINS*
#766_T2T5	lytic	0.60	18460	2995	4
#772_L2L5	lytic	2.15	25577	600	4
#772_T5T8	lytic	1.21	11593	5206	3
#775_T12L3	lytic	2.08	25331	3555	10
#782_T4T7	lytic	5.83	13638	845	3
#771_T10L1	mixed	1.11	34538	1366	8
#780_T5T8	mixed	0.44	13995	4331	7
#781_T6T9	mixed	0.18	15930	5317	6
#784_T6T9	mixed	1.23	21412	9960	5

3.2.2 Strain spatial distribution

Three-dimensional colour maps were created for each specimen to show the maximum and minimum principal strain spatial distribution. They were reported for four specimens affected by lytic (#772_T5T8, #782) and mixed (#771, #780) metastases, (see Appendix A for detailed analysis on the other specimens). The colour maps allowed us to localise the strain concentrations and the failure regions within the volume of the vertebra (Fig. 48-49). In particular, the full-field minimum principal strains maps confirmed that lytic-metastatic vertebrae reached larger strains than the controls and that those strain concentrations were in the closeness of the metastasis (Fig. 48). Vertebrae with mixed metastases, instead, experienced increased and decreased strains near the lytic and blastic portions of the lesions, respectively, when compared to the relative region of the control vertebra (Fig. 49).

A qualitative investigation of the association between the 3D strain field and the microstructure of the vertebra was performed by superimposing the strain distribution colour maps cross-section to the μCT cross-section. This allowed to localize the structure within the vertebral body with the larger deformations. In particular, in case of lytic metastases (Fig. 48), larger strains were experienced by the metastatic vertebrae in the regions including the metastases, and then propagated also to the surrounding regions. By contrast, the vertebrae affected by mixed metastases did not show a clear trend: some specimens (i.e. #771, Fig. 49 and Appendix A), in correspondence of denser tissue areas (blastic-like), experienced strain values higher than yield strain in pure compression (order of -10000 με); other specimens (i.e. #780, Fig. 49 and

Appendix A), in correspondence of the blastic lesions, reached strain smaller than those in the control vertebra, far from the bone yield strain.

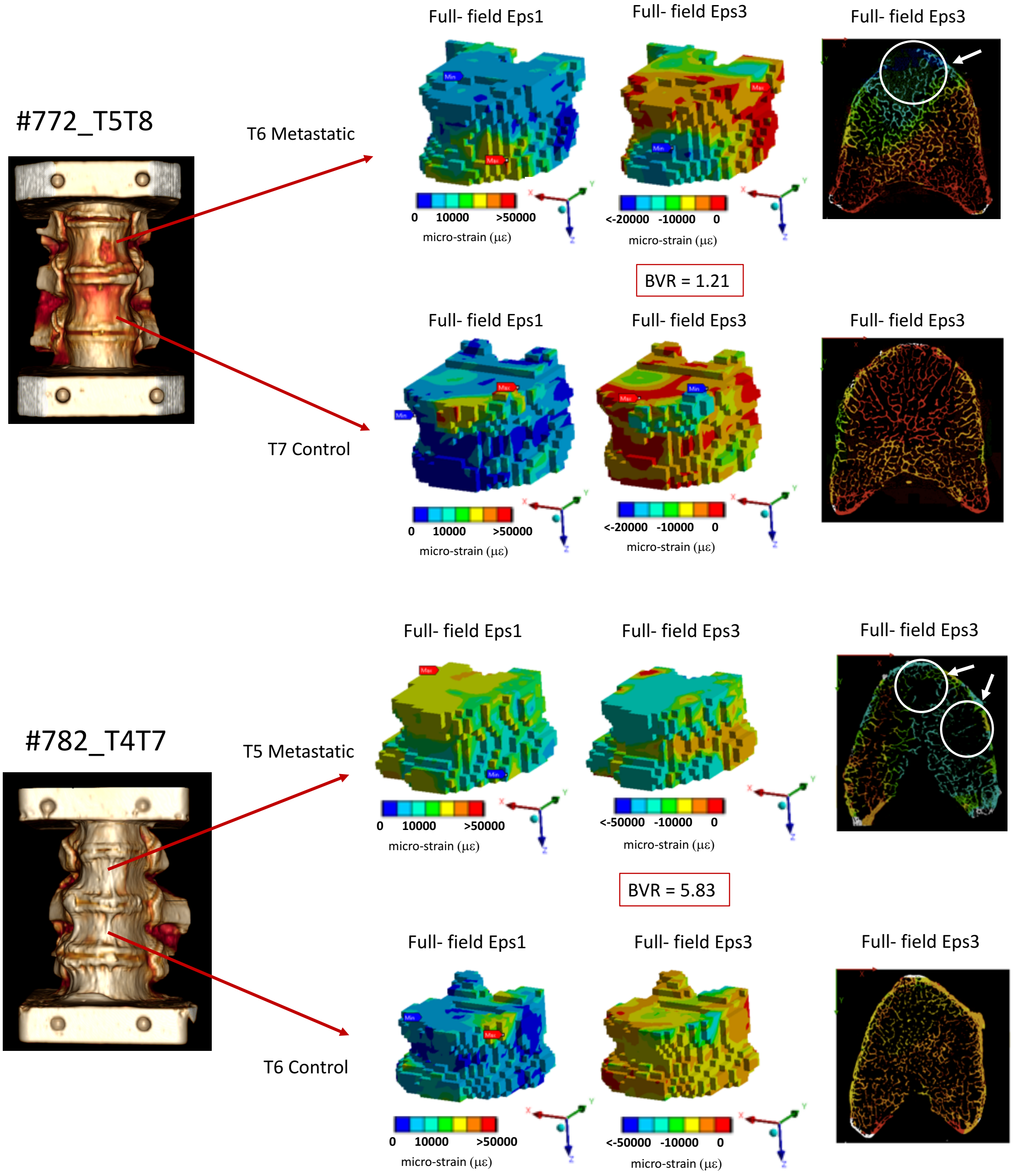

Figure 48: On the left, a 3D reconstruction of the spine segment from the qCT images is reported. Each vertebra was post-process and analysed separately: full-field maximum (Eps1) and minimum principal (Eps3) strains in the lytic-metastatic and in the control vertebra and the Biomechanical Volumetric Ratio (BVR). On the right the distribution of the minimum principal strain in the lytic-metastatic and control vertebra is superimposed on the μCT cross-section where the metastasis is located. White circles indicate the lesions.

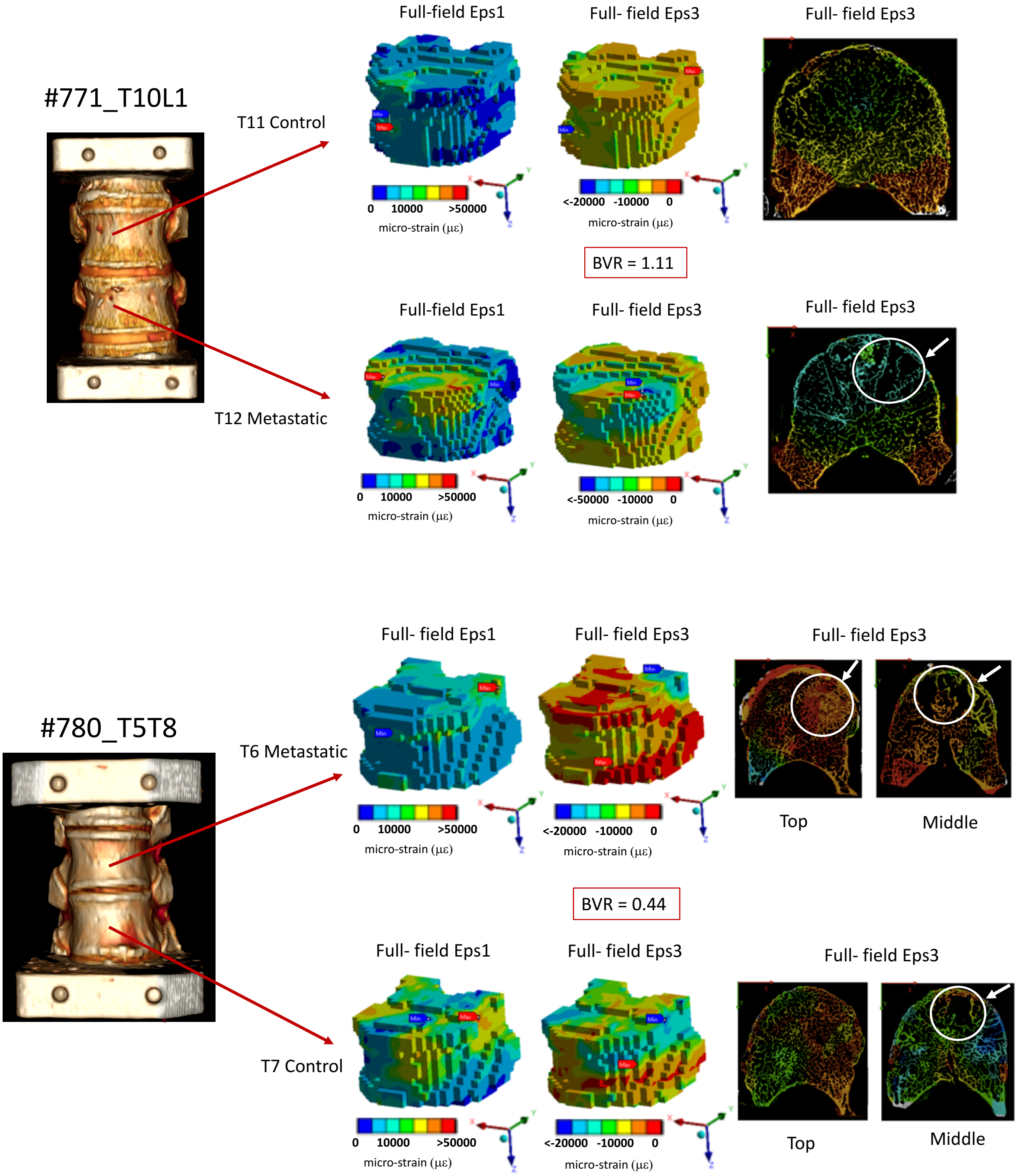

Figure 49: On the left, a 3D reconstruction of the spine segment from the qCT images is reported. Each vertebra was post-process and analysed separately: full-field maximum (Eps1) and minimum principal (Eps3) strains in the control and mixed-metastatic vertebra and the Biomechanical Volumetric Ratio (BVR). On the right the distribution of the minimum principal strain in the control and mixed-metastatic vertebra is superimposed on a μCT cross-section. White circles indicate the lesions. For specimen #780 two distribution are reported for the top and middle cross section considering the position of the blastic and lytic lesions, respectively.

3.2.3 Regional strain analysis

Lytic and blastic lesions could be more or less extended inside the vertebral body (the size of the metastases is reported in Table 7). Thus, a regional analysis was necessary to identify the most relevant strain pattern within the volume of the vertebrae.

The entire vertebra was divided into three regions of interest (ROI): Top, Middle and Bottom (refer to paragraph 2.6). The maximum and the minimum principal strain distributions in the different ROIs were evaluated for each specimen and reported for four specimens affected by lytic (#772_T5T8, #782) and mixed (#771, #780) metastases (see Appendix B for detailed analysis on the other specimens). In order to describe the frequency rate and the intensity of the principal strain patterns in the metastatic and control vertebra, frequency plots were reported: the blue histograms refer to the control vertebrae, the red ones to those with metastases (Figure 50-51-52-53). As expected, ROIs including the lytic lesions provided larger deformations in the metastatic vertebra and propagated them to the adjacent ROIs, potentially compromising the entire vertebral body. In particular, minimum principal strains in the metastatic vertebra reached strains higher than the yield strain in pure compression (order of -100000 $\mu\varepsilon$) and one order of magnitude higher than those in the control vertebra (order of -200000 $\mu\varepsilon$ and -20000 $\mu\varepsilon$, respectively).

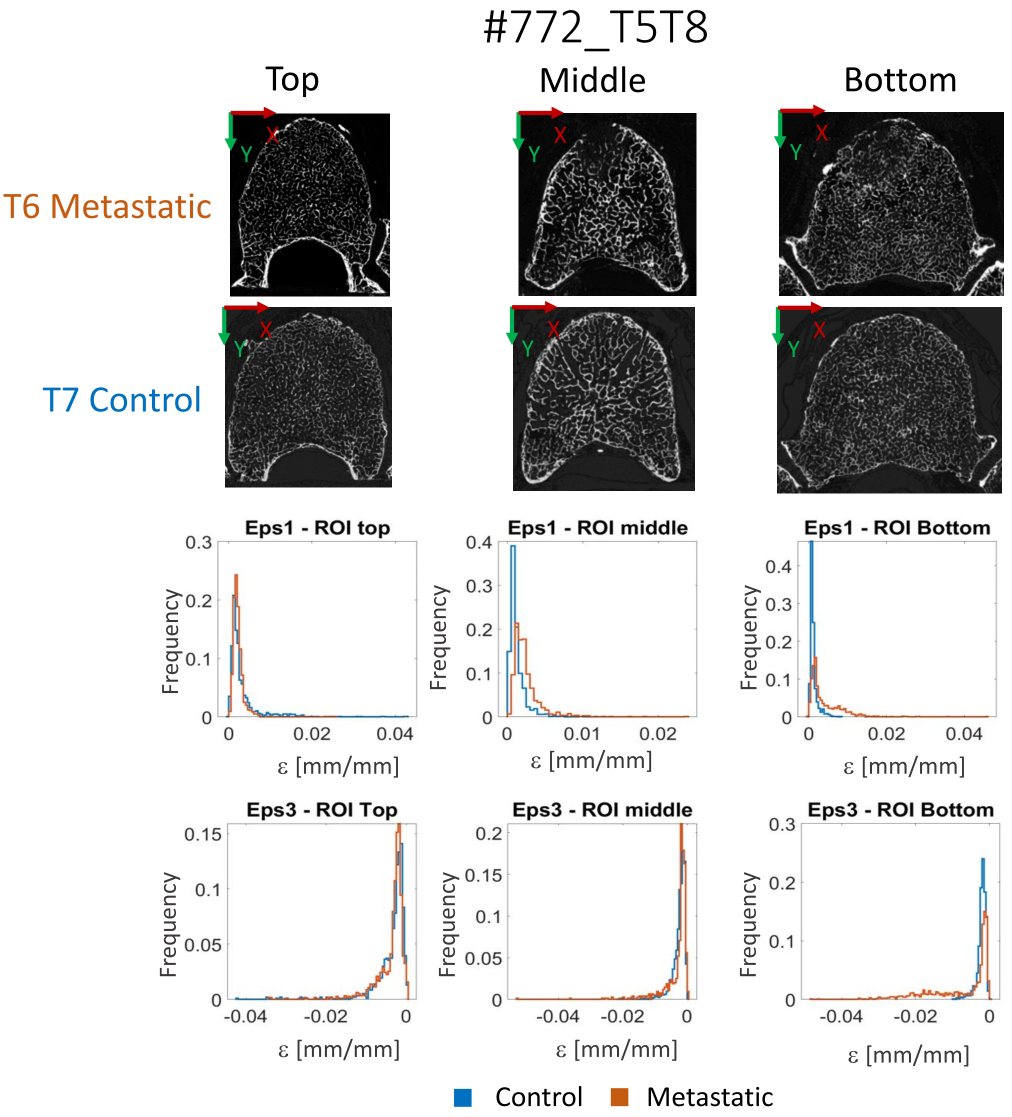

Figure 50: μCT cross-sections of the top (left column), middle (central column), bottom (right column) longitudinal ROIs of the control and lytic-metastatic vertebra; maximum principal (Eps1) and minimum principal (Eps3) strain in the top (left column), middle (central column), bottom (right column) longitudinal ROIs of lytic-metastatic (orange) and control vertebra (blue).

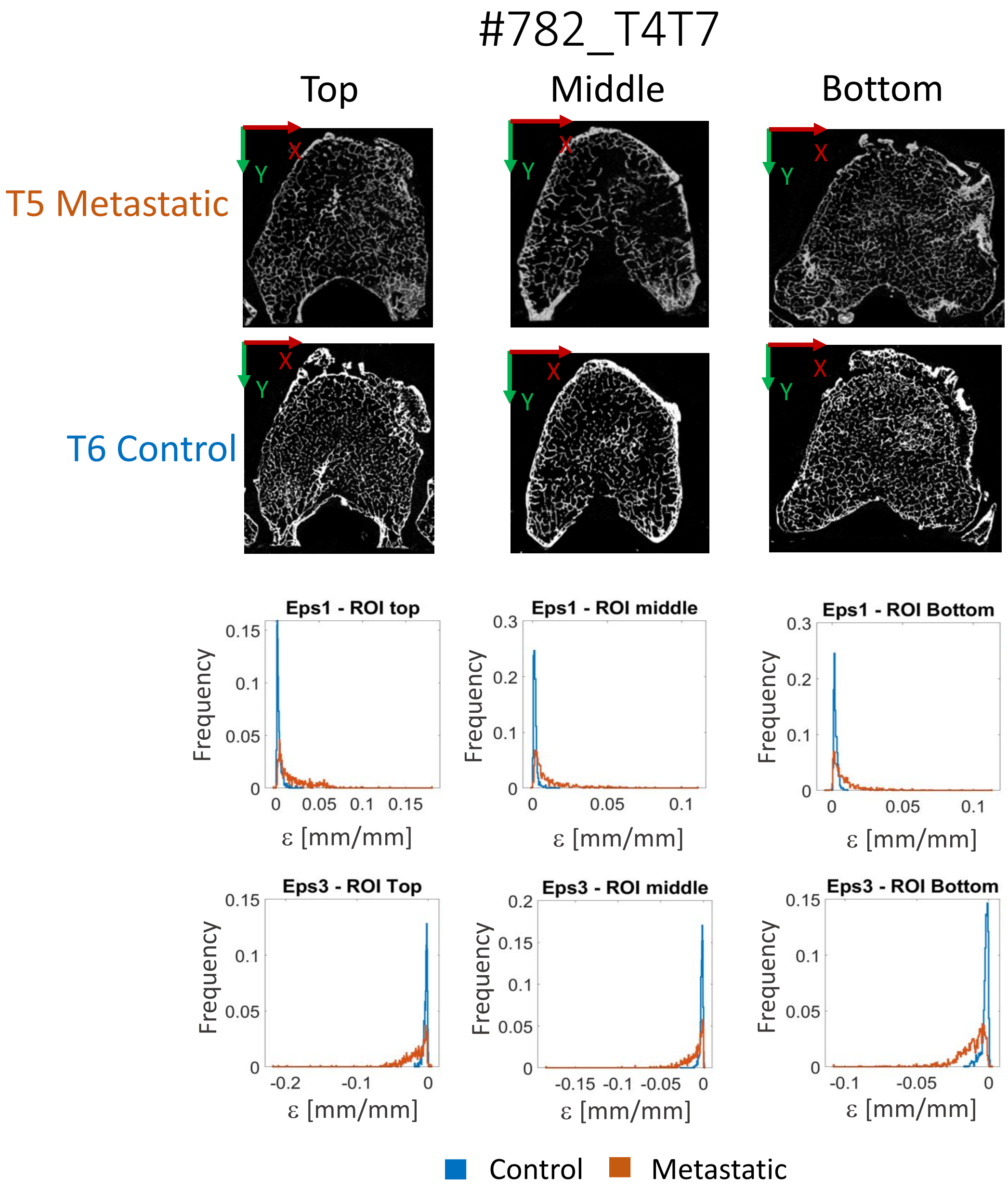

Figure 51: µCT cross-sections of the top (left column), middle (central column), bottom (right column) longitudinal ROIs of the control and lytic-metastatic vertebra; maximum principal (Eps1) and minimum principal (Eps3) strain in the top (left column), middle (central column), bottom (right column) longitudinal ROIs of lytic-metastatic (orange) and control vertebra (blue).

By contrast, vertebrae affected by mixed metastases showed different behaviours in the three ROIs. In fact, mixed metastases with mostly lytic tissue (i.e. #771, Fig. 52), reached strains similar to those reached by other lytic-metastatic vertebrae (minimum principal strains peak of the order of -100000 με), and larger than those of the controls (minimum principal strains peak of the order of -80000 με). Conversely, regions with lesions with mostly blastic tissue showed decreased strains with respect to the controls (i.e. #780, Fig. 53).

However, one specimen, classified as affected by mixed metastases with mainly blastic tissue (i.e. #784, see Appendix B), reported larger deformations in the metastatic vertebra with respect to the controls even in the blastic-metastatic region.

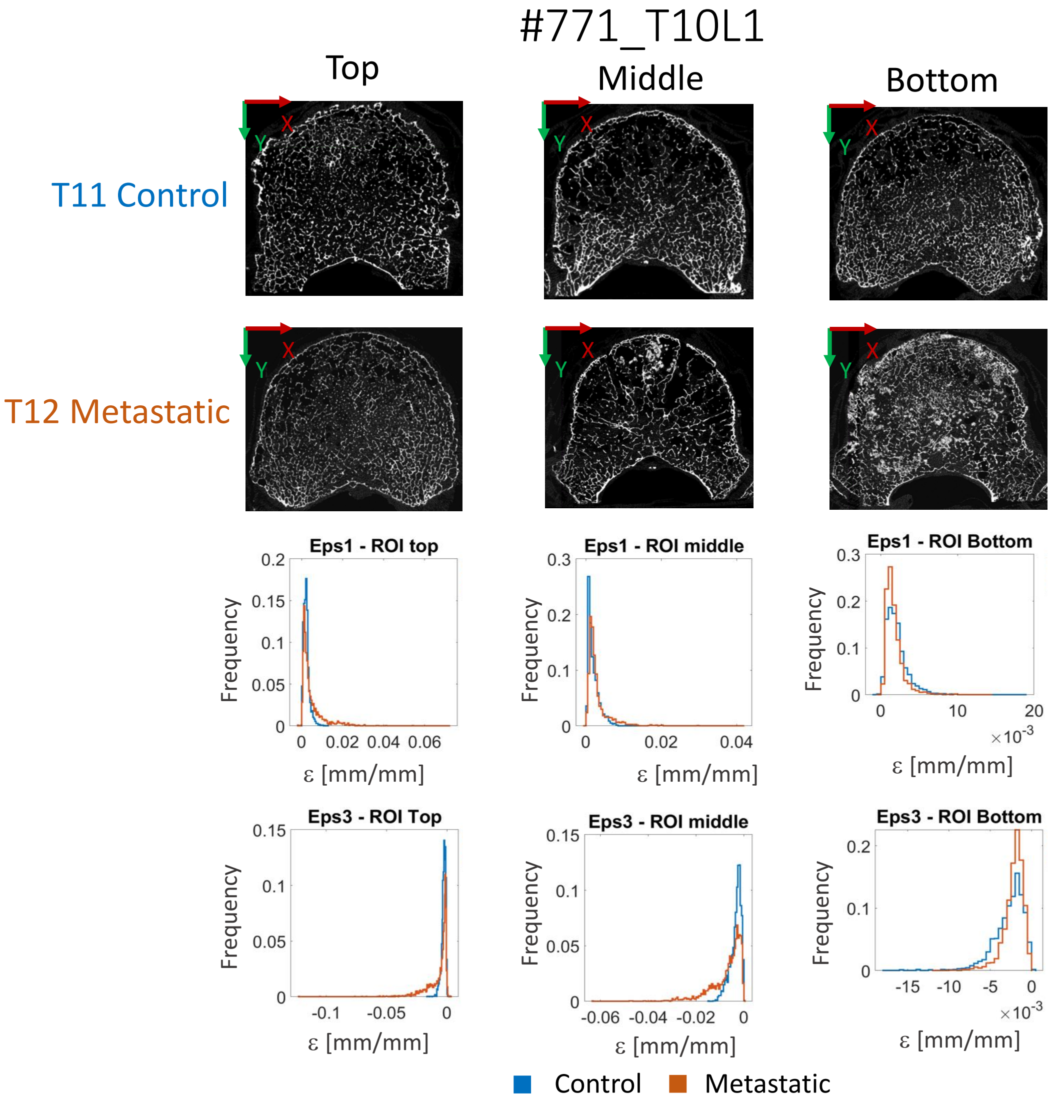

Figure 52: μCT cross-sections of the top (left column), middle (central column), bottom (right column) longitudinal ROIs of the control and mixed-metastatic vertebra; maximum principal (Eps1) and minimum principal (Eps3) strain in the top (left column), middle (central column), bottom (right column) longitudinal ROIs of lytic-metastatic (orange) and control vertebra (blue).

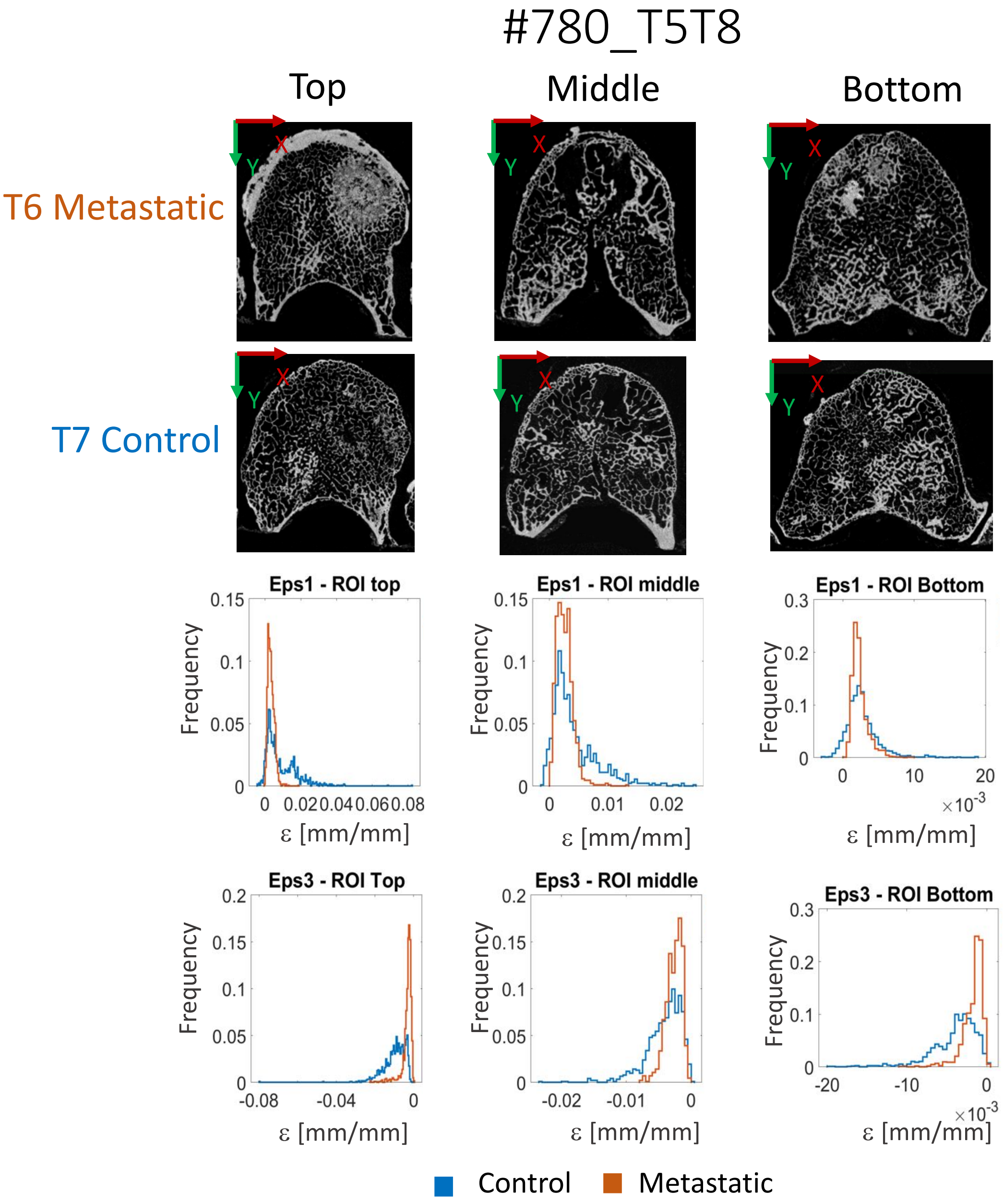

Figure 53: μCT cross-sections of the top (left column), middle (central column), bottom (right column) longitudinal ROIs of the control and mixed-metastatic vertebra; maximum principal (Eps1) and minimum principal (Eps3) strain in the top (left column), middle (central column), bottom (right column) longitudinal ROIs of lytic-metastatic (orange) and control vertebra (blue).

3.2.4 Sub-regional strain analysis

Considering the strain pattern variability in each ROI, 9 sub-regions of interest (subROIs) per ROI, in total 27 subROIs, were defined for each vertebra, allowing a more specific and detailed analysis of the most relevant portions of the metastatic vertebra. The frequency plots for the minimum principal strain distributions in the 9 subROIs of the middle ROI of one specimen (#772_T5T8), are reported in Figure 54.

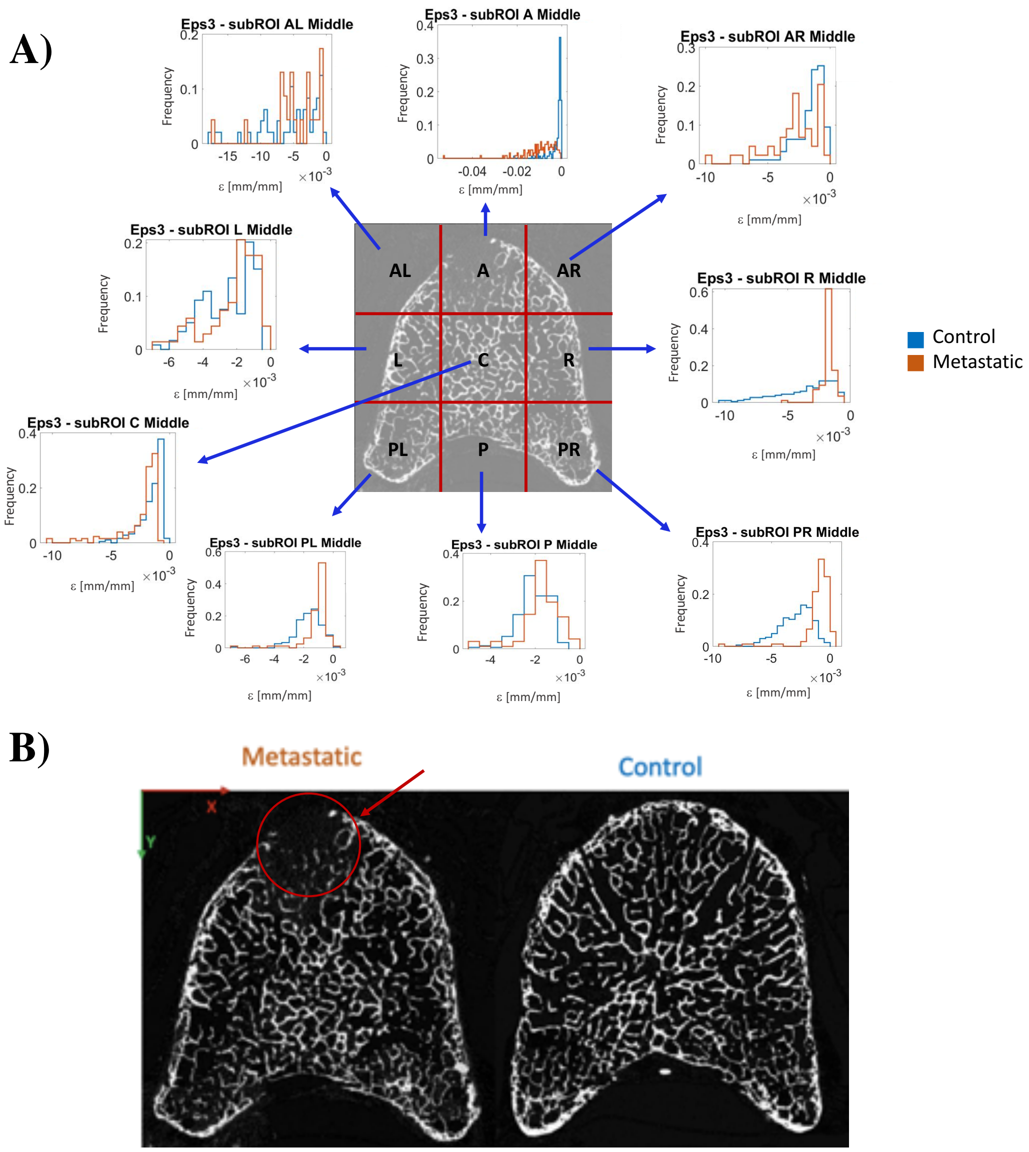

Figure 54: A) The middle cross-section was divided in nine subROIs. For each subROI minimum principal strains (Eps3) for the metastatic and control vertebra were computed and reported in histograms. B) µCT middle cross-section of the metastatic (left) and control (right) vertebrae.

In order to characterize the portion of the metastatic vertebra affected by the lesion, the Biomechanical Volumetric Ratio (BVR) was computed also for each subROI. By the comparison of the Biomechanical Volumetric Ratios, it emerged that subROIs including lytic lesions provided larger Biomechanical Volumetric Ratios. Conversely, subROIs including blastic lesions, or, denser tissues as in case of osteophyte, provided Biomechanical Volumetric Ratios lower than one, reflecting the similar behaviour of the metastatic and control vertebra.

Thematic colour maps were used to evaluate sub-regional different behaviours in the metastatic and the control vertebra. The difference between the mean minimum principal strain evaluated in the metastatic and in the control vertebra was calculated in each subROI. The subROIs were then coloured in blue when the metastatic vertebra was less deformed than the control one, not showing alarming strain for itself. Compartments were coloured in grey when the difference was below the sum of the systematic and random error and above their difference. SubROIs coloured in red represented the critical conditions of the metastatic vertebra that reached larger deformation, close to failure, with respect to the control vertebra.

The differences in the compartments confirmed the fact that subROIs including lytic lesions, in case of both lytic and mixed metastases, provided larger strains with the respect to the same subROI in the control vertebra, characterized by normal tissue, triggered the potential failure and propagated the deformation to the adjacent subROIs (i.e. #772_T5T8, #782, Fig. 55 and #771, Fig. 56). By contrast, subROIs including extended blastic regions showed similar or decreased strain with respect to those of the control vertebra (i.e. #771, #780, Fig 56), and generated alarming strains in the control vertebra.

#772_T5T8

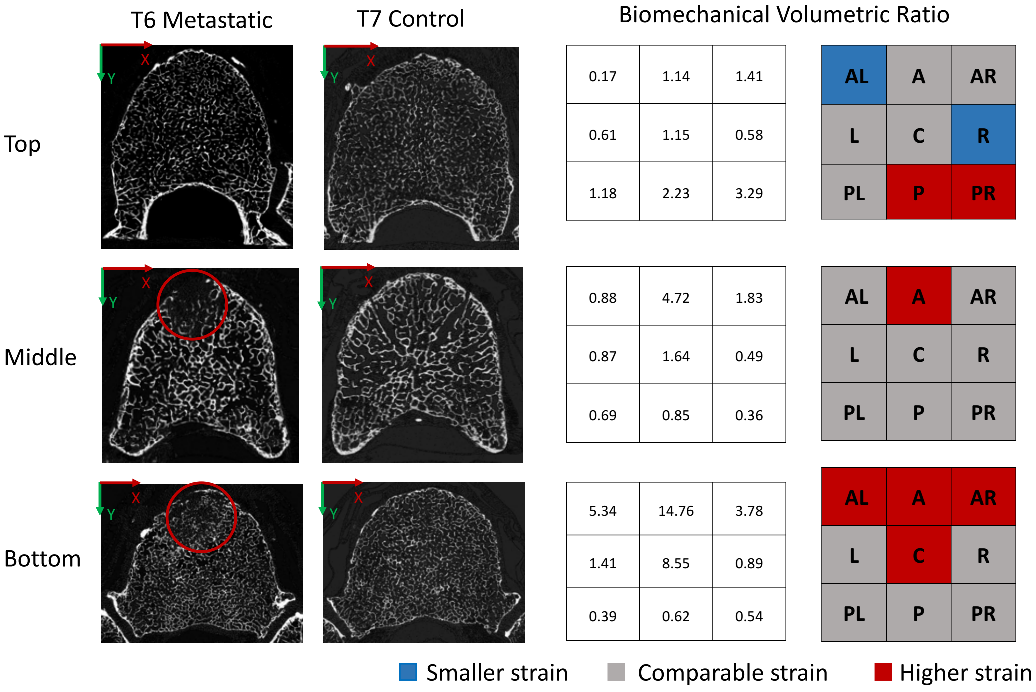

Biomechanical Volumetric Ratio

Top

0.17	1.14	1.41		🟦 AL	▨ A	▨ AR
0.61	1.15	0.58		▨ L	▨ C	🟦 R
1.18	2.23	3.29		▨ PL	🟥 P	🟥 PR

Middle

0.88	4.72	1.83		▨ AL	🟥 A	▨ AR
0.87	1.64	0.49		▨ L	▨ C	▨ R
0.69	0.85	0.36		▨ PL	▨ P	▨ PR

Bottom

5.34	14.76	3.78		🟥 AL	🟥 A	🟥 AR
1.41	8.55	0.89		▨ L	🟥 C	▨ R
0.39	0.62	0.54		▨ PL	▨ P	▨ PR

🟦 Smaller strain ▨ Comparable strain 🟥 Higher strain

#782_T4T7

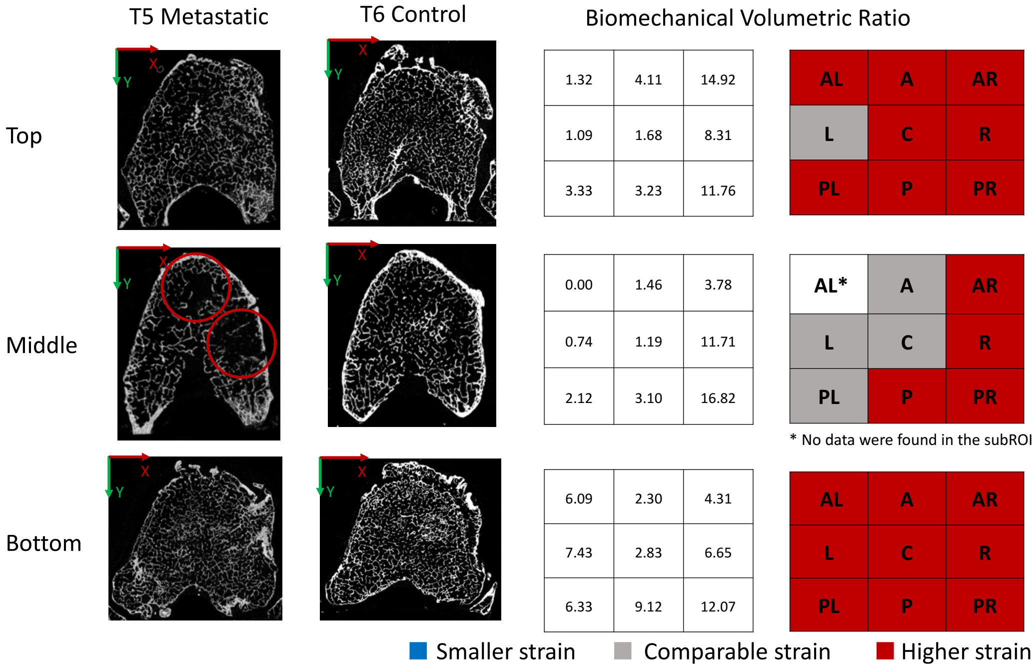

Biomechanical Volumetric Ratio

Top

1.32	4.11	14.92		🟥 AL	🟥 A	🟥 AR
1.09	1.68	8.31		▨ L	🟥 C	🟥 R
3.33	3.23	11.76		🟥 PL	🟥 P	🟥 PR

Middle

0.00	1.46	3.78		AL*	▨ A	🟥 AR
0.74	1.19	11.71		▨ L	▨ C	🟥 R
2.12	3.10	16.82		▨ PL	🟥 P	🟥 PR

* No data were found in the subROI

Bottom

6.09	2.30	4.31		🟥 AL	🟥 A	🟥 AR
7.43	2.83	6.65		🟥 L	🟥 C	🟥 R
6.33	9.12	12.07		🟥 PL	🟥 P	🟥 PR

🟦 Smaller strain ▨ Comparable strain 🟥 Higher strain

Figure 55: From left to right: µCT cross-sections of the top, middle and bottom longitudinal ROIs of the control and lytic-metastatic vertebra (red circles indicate the lesions); Biomechanical Volumetric Ratio for each subROI. Thematic colour maps: blue = smaller Eps3 in the metastatic than in the control vertebra, larger than the measurement uncertainties; grey = differences below the sum of the systematic and random error of Eps3 and above their differences; red = larger Eps3 in the metastatic than in the control vertebra, larger than the measurement uncertainties.

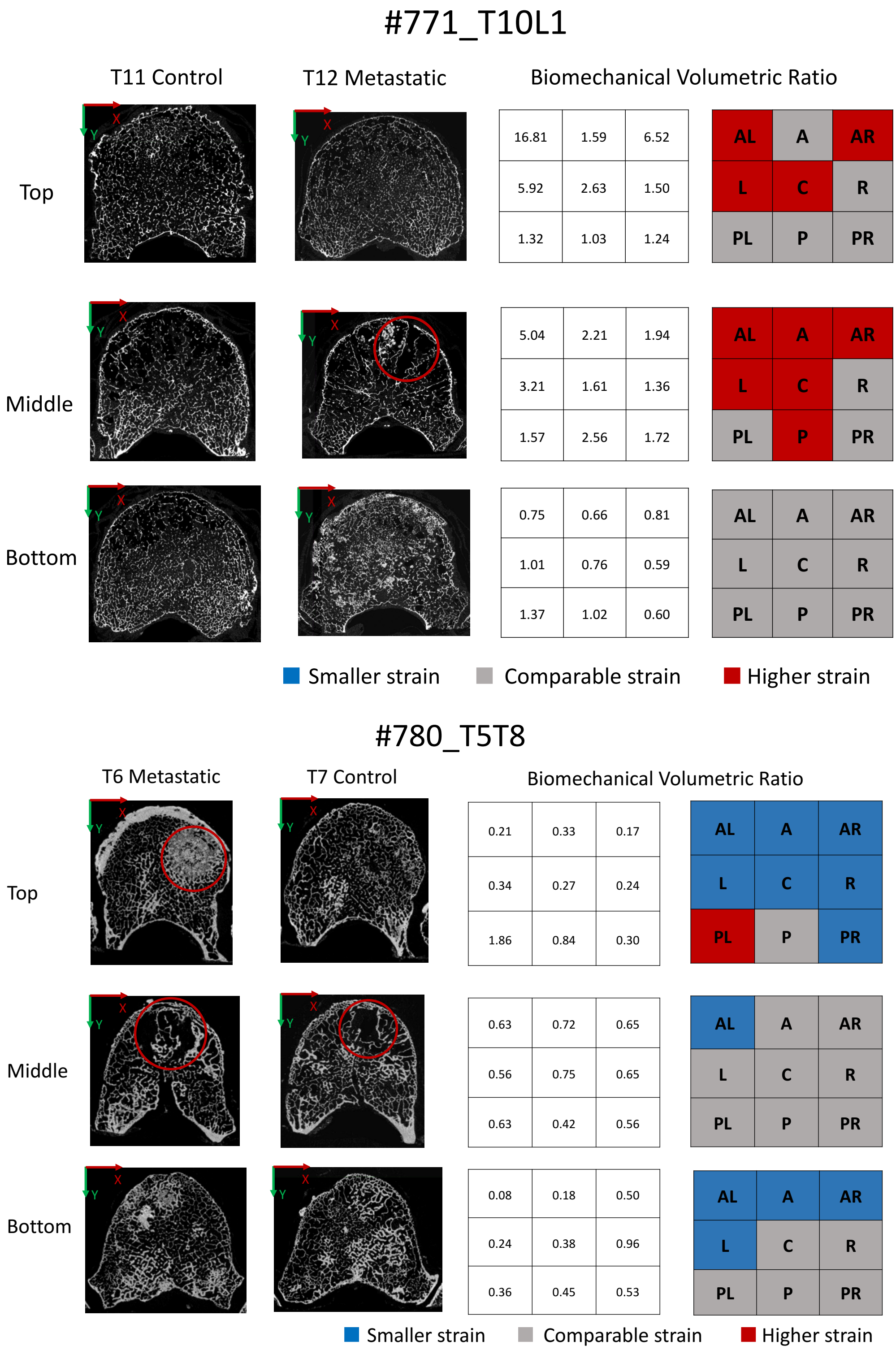

#771_T10L1 – Biomechanical Volumetric Ratio

Top

16.81	1.59	6.52
5.92	2.63	1.50
1.32	1.03	1.24

🟥 AL	⬜ A	🟥 AR
🟥 L	🟥 C	⬜ R
⬜ PL	⬜ P	⬜ PR

Middle

5.04	2.21	1.94
3.21	1.61	1.36
1.57	2.56	1.72

🟥 AL	🟥 A	🟥 AR
🟥 L	🟥 C	⬜ R
⬜ PL	🟥 P	⬜ PR

Bottom

0.75	0.66	0.81
1.01	0.76	0.59
1.37	1.02	0.60

⬜ AL	⬜ A	⬜ AR
⬜ L	⬜ C	⬜ R
⬜ PL	⬜ P	⬜ PR

🟦 Smaller strain ⬜ Comparable strain 🟥 Higher strain

#780_T5T8 – Biomechanical Volumetric Ratio

Top

0.21	0.33	0.17
0.34	0.27	0.24
1.86	0.84	0.30

🟦 AL	🟦 A	🟦 AR
🟦 L	🟦 C	🟦 R
🟥 PL	⬜ P	🟦 PR

Middle

0.63	0.72	0.65
0.56	0.75	0.65
0.63	0.42	0.56

🟦 AL	⬜ A	⬜ AR
⬜ L	⬜ C	⬜ R
⬜ PL	⬜ P	⬜ PR

Bottom

0.08	0.18	0.50
0.24	0.38	0.96
0.36	0.45	0.53

🟦 AL	🟦 A	🟦 AR
🟦 L	⬜ C	⬜ R
⬜ PL	⬜ P	⬜ PR

🟦 Smaller strain ⬜ Comparable strain 🟥 Higher strain

Figure 56: From left to right: µCT cross-sections of the top, middle and bottom longitudinal ROIs of the control and mixed-metastatic vertebra (red circles indicate the lesions); Biomechanical Volumetric Ratio for each subROI. Thematic colour maps: blue = smaller Eps3 in the metastatic than in the control vertebra, larger than the measurement uncertainties; grey = differences below the sum of the systematic and random error of Eps3 and above their differences; red = larger Eps3 in the metastatic than in the control vertebra, larger than the measurement uncertainties.

CHAPTER 4: Discussion

The aim of this study was to evaluate *in vitro* the mechanical behaviour of human metastatic vertebrae at fracture, in comparison with adjacent (healthy) control vertebrae.

In particular, human spine segments were axially loaded within a microCT (μCT) scanner, and the internal three-dimensional strain fields were measured using a global Digital Volume Correlation approach (BoneDVC). The strain measurement uncertainties were assessed for each specimen, and the global and local effects of the metastases were investigated.

The evaluation *in vitro* of the effect of metastatic lesions on the mechanical behaviour of the spine is widely reported in the literature. Single human vertebrae and spinal segments [30] with simulated metastatic lesions were tested under different loading conditions and the apparent properties and pointwise strains, by means of strain gauges, were evaluated. They showed the decrease of the mechanical competence of the vertebral body in case of lesions. However, the use of strain gauges provided only a measurement of the strain averaged over the small area where they were glued. To investigate the full-field strain distribution on the external surface of the specimen, Digital Image Correlation (DIC) can be applied. In 2018, Palanca et al. [18] tested three-vertebrae spine segments with simulated lytic defects to measure the full-field distribution of strain on the external surface of the vertebra. They showed that the size of the simulated lesion affected the strain distribution, and they identified a threshold for the volume of the defect that significantly reduces the spinal stability. However, artificial lesions cannot mimic diffused lytic or blastic lesions but can only mimic simplified geometries and do not take into account the mechanical properties of the bone metastatic tissues: tumour-altered tissue mineral content and the mineral distribution [18]. Recently, human spine segments with actual lytic and mixed metastases were analysed by using DIC combined with mechanical tests in elastic regime [36]. The measurement of the strain field on the external surface of the specimen highlighted the relevance of the evaluation of the type, size and location of the metastases in triggering the biomechanical instability. However, further analyses were necessary to evaluate the comprehensive biomechanical behaviour of metastatic vertebrae.

This limitation was overtaken in this study by using DVC, that allowed to measure of the 3D strain fields within the volume of the specimens. Accuracy and precision cannot be taken for granted, in particular human spine segments affected by actual metastases have never been tested before. We performed a preliminary analysis to optimize the DVC parameters (nodal spacing, DVC mask and voxel detection mask) and quantify the strain measurement uncertainties. An unexpected large measurement uncertainty in the coronal plane was observed. However, these high values did not clearly associate with the presence of metastases, the type of metastasis, the structural features of the vertebral body or a specific event. The mean absolute error (1155 ± 380 με) and the standard deviation of the error (564 ± 197 με) were comparable to those found on previous studies on human healthy vertebrae [3] and porcine vertebrae [46], [53], which have a more regular tissue distribution.

The field of maximum and minimum principal strain within the metastatic and control vertebral bodies at fracture were investigated through a compartmental analysis to identify the onset fracture location, possible strain patterns typical for the metastatic vertebrae, and regions with focalized strain concentrations.

3D strains colour maps reflected the distribution of the healthy and metastatic bone tissue within the vertebral bodies highlighting the different behaviours in triggering the biomechanical instability in case of lytic and mixed metastases. In general, vertebrae affected by lytic metastases showed overall higher strains than controls (Biomechanical Volumetric Ratio >1, Fig. 46). This is an effect of the lack of trabecular density and loss of structural integrity which cause a reduction in the load-bearing capacity of the remaining bone [12], [13] and increases the risk of collapse [3]. Vertebrae affected by mixed metastasis did not show a univocal trend (Biomechanical Volumetric Ratio >1 and <1, Fig. 47). In fact, mixed-metastatic vertebrae were characterized by both lytic and blastic lesions, which combined their opposite behaviours and could trigger the fracture in the adjacent control vertebrae. Thus, it is not sufficient to evaluate the behaviour at fracture of the metastatic vertebrae, but the effects of the metastases on the adjacent tissues must also be analysed.

The local analysis showed that regions with lytic-like lesions reached strains larger than normal (healthy) tissue within the same vertebra or in the control one (i.e. #782 and #771, Fig. 55). By contrast, denser or blastic-like tissues experienced smaller strains than normal (healthy) tissue (i.e. #780, Fig. 55). Even if in most cases the stiffness is well correlated with the bone mineral density [1], an unexpected behaviour was observed in some control and metastatic vertebrae.

Regions with denser trabecular patterns which were expected to be stiffer, showed larger deformations than normal (healthy) tissue. Thereby the quality of the bone (e.g.: tissue mineral distribution and content) seems to play a fundamental role in the response of the tissue to the applied load, and its potential connected risk of fracture.

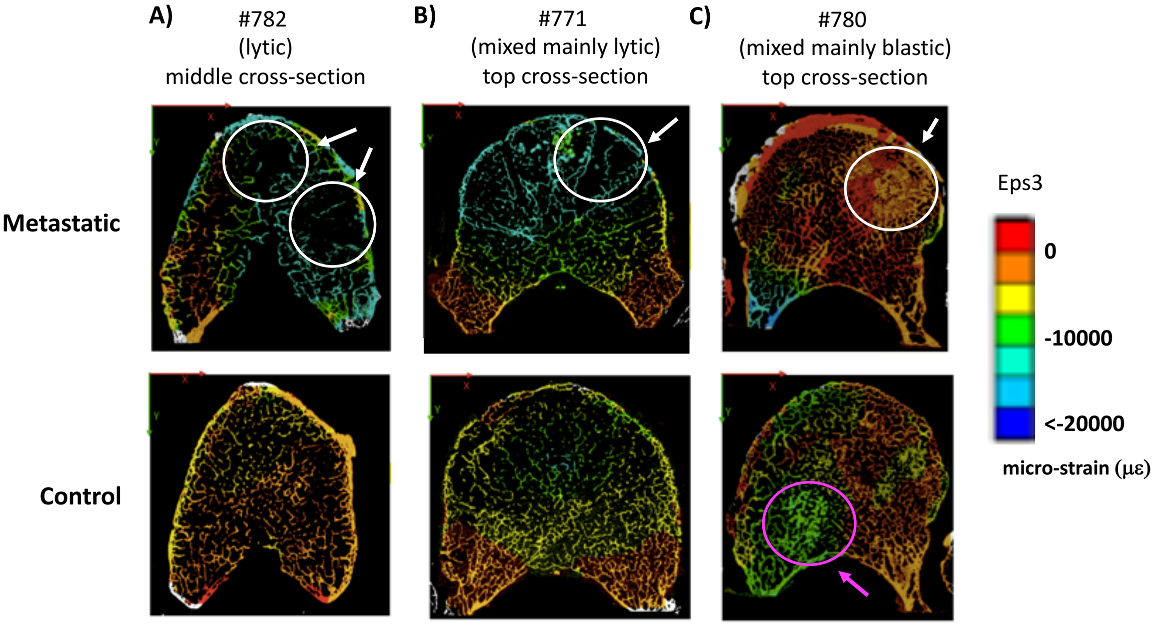

Figure 55: Comparison between the minimum principal strain field in a lytic (A), mixed with mainly lytic tissue (B) and mixed with mainly blastic tissue (C) metastatic vertebrae and their respective control vertebrae on μCT cross-section. White circles indicate lytic and blastic lesions, pink circle indicates a region with denser trabecular pattern with an unexpected behaviour.

This behaviour was clear for instance in specimen #784 (Fig. 56): the mixed-metastases was mainly blastic but the metastatic vertebra reached strains higher than those in the control vertebra and similar to those provided by lytic lesions. Thus, it must be taken into account that the mechanical competence of the vertebrae could be compromised by the poor bone tissue quality and/or by the non-optimal spatial distribution of the bone tissue.

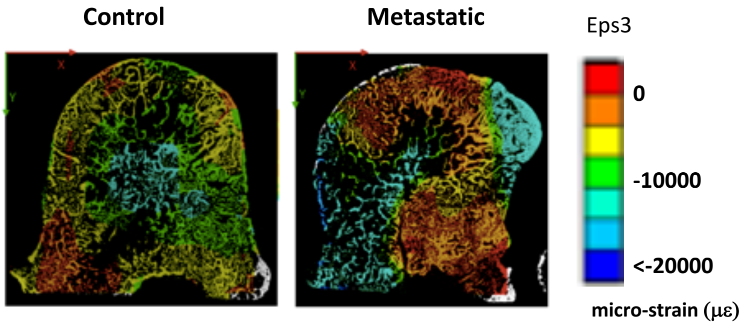

Figure 56: Specimen #784. Minimum principal strain distribution in control and metastatic vertebra on μCT cross-section. Regions with denser trabecular patter showed deformations close to the yield strain (order of -10000 με) similar to those provided by lytic lesions.

A compartmental strain analysis was performed in order to evaluate the regional and sub-regional mechanical behaviours of pathologic (lytic and mixed) and healthy bones. By dividing the metastatic and control vertebrae in region of interest (ROI, Top, Middle and Bottom), the effects of the metastases on the strain distributions were analysed to identify regions with local strain concentrations. The results confirmed that ROIs including lytic lesions experienced larger deformations with respect to those of the control vertebra in the same ROI.

As regarding mixed metastases, regions too wide, as a ROI, could include both lytic and blastic lesions which combine their opposite behaviours. Thus, to evaluate the single supply of each lesion a more focused analysis on a smaller region was necessary.

The sub-ROI division was defined for each specimen to allow a more specific and detailed analysis of the portion of the metastatic vertebra affected by the lesion. The BVR was computed in each subROI to have an immediate comparison between the mechanical assessment of the metastatic and control vertebrae in each subROI. In case of lytic lesions, the largest BVR were in the subROIs including the lesions and the surrounding ones; blastic lesions or, area with denser bone tissue or osteophytes, provided BVR lower than one, reflecting the similar behaviour of the metastatic and control vertebra. The use of thematic colour maps to represent the sub-regional differences between the minimum principal strain in the metastatic and control vertebra allowed us to obtain an easy-to-use tool to identify the most critical differences between the metastatic and control vertebra. In fact, the compartments allowed to qualitatively identify the subROIs that triggered the potential failure in the metastatic or control vertebra and to correlate it with the features of the metastasis, as size, position, shape, etc.

As the failure is the effect of a local balance between the load and the strength, these approaches and the consequent unprecedented data will provide the first insight to better understand the mechanics of the fracture in metastatic spine segments. This study merged a detailed strain analysis within the bone tissue, a qualitative local characterization of the bone structure, with the complex mechanical behaviour of the vertebra, providing an innovative method for a comprehensive characterization of metastatic spinal segments.

In a future translational research, this evidence could be used to implement new biomechanical-based criteria to ensure clearer guidelines for bone stabilization.

Moreover, these results could be used to validate the local outputs of computational models of human vertebra with actual metastases. In fact, finite element (FE) models have already been used to predict the effect of the metastases on the apparent properties (e.g. bone strength) of human vertebral bodies with actual lesions [63]. However, considering the complex and variable behaviour of vertebrae with actual metastases, the DVC data can be used to validate Micro-FE models of human vertebrae to predict the local deformations and the local effects of the metastatic lesions [54], [59].

There are some limitations in this study that must be considered. First of all, the sample size was too small to generalise the findings. However, a comprehensive and detailed analysis was performed on each specimen, evaluating the global and local properties. Moreover, this analysis could be enlarged considering that the sample was subjected to a series of mechanical tests [36] before the analysis reported in this work. Physiological loads were applied to each specimen only in the elastic regime, according to the protocol reported in [36] during the DIC measurements, and the effects of type, size and position of the metastasis were identified.

In this study, each specimen was tested inside the μCT chamber only in step-wise axial compressive loadings. To have a multi-loading characterization of the biomechanical behaviour of the spine segments, the experimental set-up should be modified in order to apply other loading conditions, as flexion and anterior and later bending [36], and measure the actual multi-directional imposed loads. Anyway, the relevance of the study is not compromised because, in general, the spine is mainly subject to compressive loads in almost all physiologic motor tasks [1], [2].

In order to allow the spine segments to fit within the jig, the posterior elements of each specimen had to be removed. The lack of support from the posterior elements is a worst case scenario that can actually affect patients with spinal metastases: when metastases destroy the pedicles [16].

Another limitation of the DVC approach combined with *in situ* mechanical tests concerned the time consuming process to acquire the 3D images within the μCT. Since the spine segment including both vertebral bodies and discs are viscoelastic structures, they have a time-dependent behaviour and show creep and stress relaxation when constant loads or deformations are applied. However, this study focused mainly on the bone tissues of the vertebral body, which have a linear behaviour. Furthermore, during these long scanning sessions, the specimens could be dehydrated. To avoid this problem, specimens were wrapped in gauzes soaked in saline solution.

The image processing phase included manual operator-dependent selection of portions of the images, as for the mask preparation. The reproducibility of the approach was explored.

Spinal metastases are a widespread tumour, which can affect multiple vertebrae in the same spine and eventually, adjacent vertebrae. The type and location of the metastasis were evaluated by two expert spinal oncological surgeons through qCT. Each specimen included a control vertebra, a metastatic one and other two at the extremities. The control vertebrae were considered as a healthy vertebrae based on the qCT, but sometimes the vertebrae of a metastatic spine could be affected by a less relevant metastatic condition, not resolvable by a qCT but clearly visible in the μCT.

Moreover, patients affected by spinal metastases often have co-morbidity and are subjected to pharmacological treatments which can alter the normal distribution and the quality of the bone tissue. In fact, the bone tissue could have poor mechanical properties that influence the bone strength [12] [69]. Thus, an assessment of the bone tissue quality may be useful to have a comprehensive characterization of the vertebral tissue.

In order to have a quantitative assessment of the architecture of the vertebral bodies, a microstructural analysis is necessary. It would allow quantifying the ratio between the bone volume and the total volume of bone tissue (BV/TV), the size and number of trabeculae. Nanoindentation tests of the metastatic and healthy bone tissue should be performed in order to evaluate the effects of the metastases on the bone structure and the blastic metastatic tissue properties. Microstructural analysis would also allow us to evaluate whether there is a correlation between the trabecular pattern and the 3D strain distribution inside the vertebra and to better understand the different behaviours in regions with the same apparent trabecular density.

Conclusions

In this work, for the first time, the Digital Volume Correlation (DVC) was used to evaluate the effects of the metastatic features (e.g. size, position, shape, etc.) on the mechanical behaviour at fracture in human spine segments.

A preliminary methodological optimization of the DVC parameters (nodal spacing, DVC mask and VD mask) allowed us to obtain an acceptable accuracy and precision to investigate the variation of strain distributions inside the vertebra in case of failure.

The full-field principal strain distributions at fracture in the metastatic and control vertebrae were measured and compared. The outcomes showed the different behaviours between the control and metastatic vertebrae, and the effects of the different types of metastases on the global deformation: the vertebrae affected by lytic metastases experienced overall higher strains than those measured in the controls. Conversely, the vertebrae affected by mixed metastases did not show a univocal trend in the failed vertebra. Moreover, the association between the 3D strain field and the microstructure of the vertebra allowed the reciprocal identification of the regions with focalized strain concentration and the onset fracture location.

The local characterization of the strain distributions highlighted the variability of the strain patterns in case of mixed metastases which combine the opposite behaviour of lytic and blastic lesions. In particular, regions including lytic lesions reached strains larger than those measure in the normal (healthy) tissue. Conversely, denser or blastic-like tissues experienced overall smaller strains than the adjacent normal (healthy) tissue. However, in some metastatic and control vertebrae an unexpected behaviour was observed. In some regions with denser trabecular patterns, which were expected to be stiffer, deformations larger than those measured in the adjacent normal (healthy) tissue were found. Indeed, the bone tissue spatial distribution, density and quality play a fundamental role in the load-bearing capacity. In particular, possible consequences of the tumour and the drug treatments can explain the reduced mechanical competence of the spine, and trigger the fracture. In order to better understand this unexpected behaviour, a qualitative and quantitative assessment of the bone structure is mandatory.

Regional and sub-regional analyses confirmed the importance of locally analysing the strain pattern to identify regions that trigger the potential failure in the metastatic or in the control vertebra, and to correlate them with the features of the metastasis, as size, position, shape, etc. This method and the consequent evidence, once generalized on a larger sample, could be used to implement new biomechanical-based criteria in the current scoring systems ensuring clearer guidelines for assessing the spinal instability.

Acknowledgements

I would like to sincerely thank my supervisor Prof. Luca Cristofolini for the opportunity to take part in this study, for trusting my skills and for teaching me what scientific research is. The current situation did not allow me to come to Bologna every day, however, even from home, you always made me feel part of the team.

And it is the SPINE-TEAM that I want to thank the most. A special thanks goes to Dr. Enrico Dall'Ara who trusted me even from miles away. I'm so grateful for your continuous support and suggestion. I hope we could meet soon. Thanks to Marco, for sharing this project with me 24/7, thanks for your patience and your contagious enthusiasm, and for helping me in times of difficulty (holy back-up)! Thank you for taking me to the amazing Sheffield (remotely), now I am psychologically-prepared for the rain! I’m sure I will never forget all your life tips.

And finally I want to thank every person who has shared with me all these years. Everything would have been different without you.

Bibliography

[1] A. A. White e M. M. Panjabi, «Clinical biomechanics of the spine», 1990.

[2] H. Gray, «*Gray's Anatomy*», 41st ed. Elsevier, 2015.

[3] C. G. Fisher *et al.*, «A Novel Classification System for Spinal Instability in Neoplastic Disease: An Evidence-Based Approach and Expert Consensus From the Spine Oncology Study Group», *Spine*, vol. 35, n. 22, pagg. E1221–E1229, ott. 2010.

[4] I. Laufer *et al.*, «The NOMS Framework: Approach to the Treatment of Spinal Metastatic Tumors», *The Oncologist*, vol. 18, n. 6, pagg. 744–751, giu. 2013, doi: 10.1634/theoncologist.2012-0293.

[5] Y. Tokuhashi, H. Matsuzaki, H. Oda, M. Oshima, e J. Ryu, «A Revised Scoring System for Preoperative Evaluation of Metastatic Spine Tumor Prognosis», pag. 6.

[6] M. C. Costa, P. Eltes, A. Lazary, P. P. Varga, M. Viceconti, e E. Dall'Ara, «Biomechanical assessment of vertebrae with lytic metastases with subject-specific finite element models», *Journal of the Mechanical Behavior of Biomedical Materials*, vol. 98, pagg. 268–290, ott. 2019, doi: 10.1016/j.jmbbm.2019.06.027.

[7] M. R. Hardisty, M. K. Akens, S.-P. Hojjat, A. Yee, e C. M. Whyne, «Quantification of the effect of osteolytic metastases on bone strain within whole vertebrae using image registration: EFFECT OF OSTEOLYTIC METASTASES ON BONE STRAIN», *J. Orthop. Res.*, vol. 30, n. 7, pagg. 1032–1039, lug. 2012, doi: 10.1002/jor.22045.

[8] R.Putz e R.Pabs, «Sobotta - Atlas Human Anatomy Volume2 14th Edition». .

[9] A. I. Hussein, Z. D. Mason, e E. F. Morgan, «Presence of intervertebral discs alters observed stiffness and failure mechanisms in the vertebra», *Journal of Biomechanics*, vol.

46, n. 10, pagg. 1683–1688, giu. 2013, doi: 10.1016/j.jbiomech.2013.04.004.

[10] M. Palanca, L. Cristofolini, A. Gasbarrini, G. Tedesco, e G. Barbanti-Bròdano, «Assessing the Mechanical Weakness of Vertebrae Affected by Primary Tumors: A Feasibility Study», *Materials*, vol. 13, n. 15, pag. 3256, lug. 2020, doi: 10.3390/ma13153256.

[11] R. Coleman, «Incidence and Distribution of Bone Metastases», in *Metastatic Bone Disease*, I. J. Diel, M. Kaufmann, e G. Bastert, A c. di Berlin, Heidelberg: Springer Berlin Heidelberg, 1994, pagg. 20–30.

[12] C. M. Whyne, «Biomechanics of metastatic disease in the vertebral column», *Neurological Research*, vol. 36, n. 6, pagg. 493–501, giu. 2014, doi: 10.1179/1743132814Y.0000000362.

[13] R. E. Coleman, «Metastatic bone disease: clinical features, pathophysiology and treatment strategies», *Cancer Treatment Reviews*, vol. 27, n. 3, pagg. 165–176, giu. 2001, doi: 10.1053/ctrv.2000.0210.

[14] G. H. Bell, O. Dunbar, J. S. Beck, e A. Gibb, «Variations in strength of vertebrae with age and their relation to osteoporosis», *Calc. Tis Res.*, vol. 1, n. 1, pagg. 75–86, dic. 1967, doi: 10.1007/BF02008077.

[15] T. Hansson e B. Roos, «The Influence of Age, Height, and Weight on the Bone Mineral COntent of Lumbar Vertebrae», *Spine*, vol. 5, n. 6, dic. 1980.

[16] H. Taneichi, K. Kaneda, N. Takeda, K. Abumi, e S. Satoh, «Risk Factors and Probability of Vertebral Body Collapse in Metastases of the Thoracic and Lumbar Spine»:, *Spine*, vol. 22, n. 3, pagg. 239–245, feb. 1997, doi: 10.1097/00007632-199702010-00002.

[17] F. Galbusera *et al.*, «The Role of the Size and Location of the Tumors and of the Vertebral Anatomy in Determining the Structural Stability of the Metastatically Involved Spine: a Finite Element Study», *Translational Oncology*, vol. 11, n. 3, pagg. 639–646, giu. 2018,

doi: 10.1016/j.tranon.2018.03.002.

[18] M. Palanca, G. Barbanti-Bròdano, e L. Cristofolini, «The Size of Simulated Lytic Metastases Affects the Strain Distribution on the Anterior Surface of the Vertebra», *Journal of Biomechanical Engineering*, vol. 140, n. 11, pag. 111005, nov. 2018, doi: 10.1115/1.4040587.

[19] C. G. Fisher *et al.*, «Reliability of the Spinal Instability Neoplastic Scale Among Radiologists: An Assessment of Instability Secondary to Spinal Metastases», *American Journal of Roentgenology*, vol. 203, n. 4, pagg. 869–874, ott. 2014, doi: 10.2214/AJR.13.12269.

[20] C. G. Fisher *et al.*, «Reliability of the Spinal Instability Neoplastic Score (SINS) among radiation oncologists: an assessment of instability secondary to spinal metastases», *Radiat Oncol*, vol. 9, n. 1, pag. 69, dic. 2014, doi: 10.1186/1748-717X-9-69.

[21] D. R. Fourney *et al.*, «Spinal Instability Neoplastic Score: An Analysis of Reliability and Validity From the Spine Oncology Study Group», *JOURNAL OF CLINICAL ONCOLOGY*, pag. 6.

[22] M. Palanca, L. Cristofolini, M. Marciante, M. Serra, A. Gasbarrini, e G. Barbanti-Bròdano, «Lack of correlation between the SINS and the biomechanical outcomes in case of metastatic vertebra», *GSC2020*, 2020.

[23] A. I. Hussein, P. E. Barbone, e E. F. Morgan, «Digital Volume Correlation for Study of the Mechanics of Whole Bones», *Procedia IUTAM*, vol. 4, pagg. 116–125, 2012, doi: 10.1016/j.piutam.2012.05.013.

[24] H. Mirels, «The Classic: Metastatic Disease in Long Bones A Proposed Scoring System for Diagnosing Impending Pathologic Fractures»:, *Clinical Orthopaedics and Related Research*, vol. 415, pagg. S4–S13, ott. 2003, doi: 10.1097/01.blo.0000093045.56370.dd.

[25] N. Brandolini, L. Cristofolini, e M. Viceconti, «EXPERIMENTAL METHODS FOR

THE BIOMECHANICAL INVESTIGATION OF THE HUMAN SPINE: A REVIEW», *J. Mech. Med. Biol.*, vol. 14, n. 01, pag. 1430002, feb. 2014, doi: 10.1142/S0219519414300026.

[26] N. V. Jaumard, J. Leung, A. J. Gokhale, B. B. Guarino, W. C. Welch, e B. A. Winkelstein, «Relevant Anatomic and Morphological Measurements of the Rat Spine: Considerations for Rodent Models of Human Spine Trauma», *Spine*, vol. 40, n. 20, pagg. E1084–E1092, ott. 2015, doi: 10.1097/BRS.0000000000001021.

[27] L. Cristofolini, N. Brandolini, V. Danesi, M. M. Juszczyk, P. Erani, e M. Viceconti, «Strain distribution in the lumbar vertebrae under different loading configurations», *The Spine Journal*, vol. 13, n. 10, pagg. 1281–1292, ott. 2013, doi: 10.1016/j.spinee.2013.06.014.

[28] M. J. Silva, J. A. Hipp, D. P. McGowan, T. Takeuchi, e W. C. Hayes, «Strength reductions of thoracic vertebrae in the presence of transcortical osseous defects: effects of defect location, pedicle disruption, and defect size», *Eur Spine J*, vol. 2, n. 3, pagg. 118–125, ott. 1993, doi: 10.1007/BF00301407.

[29] R. N. Alkalay, «Effect of the metastatic defect on the structural response and failure process of human vertebrae: An experimental study», *Clinical Biomechanics*, pag. 8, 2015.

[30] R. N. Alkalay e T. P. Harrigan, «Mechanical assessment of the effects of metastatic lytic defect on the structural response of human thoracolumbar spine: EFFECT OF CRITICAL LYTIC DEFECT», *J. Orthop. Res.*, vol. 34, n. 10, pagg. 1808–1819, ott. 2016, doi: 10.1002/jor.23154.

[31] B. C. Roberts, E. Perilli, e K. J. Reynolds, «Application of the digital volume correlation technique for the measurement of displacement and strain fields in bone: A literature review», *Journal of Biomechanics*, vol. 47, n. 5, pagg. 923–934, mar. 2014, doi:

10.1016/j.jbiomech.2014.01.001.

[32] M. Palanca, G. Tozzi, e L. Cristofolini, «The use of digital image correlation in the biomechanical area: a review», *International Biomechanics*, vol. 3, n. 1, pagg. 1–21, gen. 2016, doi: 10.1080/23335432.2015.1117395.

[33] M. L. Ruspi, M. Palanca, C. Faldini, e L. Cristofolini, «Full-field in vitro investigation of hard and soft tissue strain in the spine by means of Digital Image Correlation», pag. 8.

[34] M. Palanca, M. Marco, M. L. Ruspi, e L. Cristofolini, «Full-field strain distribution in multi-vertebra spine segments: An in vitro application of digital image correlation», *Medical Engineering & Physics*, vol. 52, pagg. 76–83, feb. 2018, doi: 10.1016/j.medengphy.2017.11.003.

[35] M. Palanca, T. M. Brugo, e L. Cristofolini, «USE OF DIGITAL IMAGE CORRELATION TO INVESTIGATE THE BIOMECHANICS OF THE VERTEBRA», *J. Mech. Med. Biol.*, vol. 15, n. 02, pag. 1540004, apr. 2015, doi: 10.1142/S0219519415400047.

[36] M. Palanca *et al.*, «The type, size and position of the metastatic lesions explain the reduction of the mechanical competence of the vertebra», gen. 2021.

[37] C. Techens, M. Palanca, P. E. Éltes, Á. Lazáry, e L. Cristofolini, «Testing the impact of discoplasty on the biomechanics of the intervertebral disc with simulated degeneration: An in vitro study», *Medical Engineering & Physics*, vol. 84, pagg. 51–59, ott. 2020, doi: 10.1016/j.medengphy.2020.07.024.

[38] M. L. Ruspi *et al.*, «Digital Image Correlation (DIC) Assessment of the Non-Linear Response of the Anterior Longitudinal Ligament of the Spine during Flexion and Extension», *Materials*, vol. 13, n. 2, pag. 384, gen. 2020, doi: 10.3390/ma13020384.

[39] G. Tozzi, V. Danesi, M. Palanca, e L. Cristofolini, «Elastic Full-Field Strain Analysis and Microdamage Progression in the Vertebral Body from Digital Volume Correlation: Strain

Analysis in the Vertebral Body from Digital Volume Correlation», *Strain*, vol. 52, n. 5, pagg. 446–455, ott. 2016, doi: 10.1111/str.12202.

[40] B. K. Bay, T. S. Smith, D. P. Fyhrie, e M. Saad, «Digital volume correlation: Three-dimensional strain mapping using X-ray tomography», *Experimental Mechanics*, vol. 39, n. 3, pagg. 217–226, set. 1999, doi: 10.1007/BF02323555.

[41] E. Dall'Ara, M. Peña-Fernández, M. Palanca, M. Giorgi, L. Cristofolini, e G. Tozzi, «Precision of Digital Volume Correlation Approaches for Strain Analysis in Bone Imaged with Micro-Computed Tomography at Different Dimensional Levels», *Front. Mater.*, vol. 4, pag. 31, nov. 2017, doi: 10.3389/fmats.2017.00031.

[42] J. C. Elliott e S. D. Dover, «X-ray microtomography», *Journal of Microscopy*, vol. 126, n. 2, pagg. 211–213, mag. 1982, doi: 10.1111/j.1365-2818.1982.tb00376.x.

[43] M. R. Hardisty e C. M. Whyne, «Whole Bone Strain Quantification by Image Registration: A Validation Study», *Journal of Biomechanical Engineering*, vol. 131, n. 6, pag. 064502, giu. 2009, doi: 10.1115/1.3127249.

[44] S. J. Schambach, S. Bag, L. Schilling, C. Groden, e M. A. Brockmann, «Application of micro-CT in small animal imaging», pag. 12, 2010.

[45] M. Palanca, G. Tozzi, L. Cristofolini, M. Viceconti, e E. Dall'Ara, «Three-Dimensional Local Measurements of Bone Strain and Displacement: Comparison of Three Digital Volume Correlation Approaches», *Journal of Biomechanical Engineering*, vol. 137, n. 7, pag. 071006, lug. 2015, doi: 10.1115/1.4030174.

[46] M. Palanca *et al.*, «Digital volume correlation can be used to estimate local strains in natural and augmented vertebrae: An organ-level study», *Journal of Biomechanics*, vol. 49, n. 16, pagg. 3882–3890, dic. 2016, doi: 10.1016/j.jbiomech.2016.10.018.

[47] E. Dall'Ara, D. Barber, e M. Viceconti, «About the inevitable compromise between spatial resolution and accuracy of strain measurement for bone tissue: A 3D zero-strain

study», *Journal of Biomechanics*, vol. 47, n. 12, pagg. 2956–2963, set. 2014, doi: 10.1016/j.jbiomech.2014.07.019.

[48] L. Liu e E. F. Morgan, «Accuracy and precision of digital volume correlation in quantifying displacements and strains in trabecular bone», *Journal of Biomechanics*, vol. 40, n. 15, pagg. 3516–3520, gen. 2007, doi: 10.1016/j.jbiomech.2007.04.019.

[49] M. Giorgi e E. Dall'Ara, «Variability in strain distribution in the mice tibia loading model: A preliminary study using digital volume correlation», *Medical Engineering & Physics*, vol. 62, pagg. 7–16, dic. 2018, doi: 10.1016/j.medengphy.2018.09.001.

[50] M. K. Ryan, S. Oliviero, M. C. Costa, J. M. Wilkinson, e E. Dall'Ara, «Heterogeneous Strain Distribution in the Subchondral Bone of Human Osteoarthritic Femoral Heads, Measured with Digital Volume Correlation», *Materials*, vol. 13, n. 20, pag. 4619, ott. 2020, doi: 10.3390/ma13204619.

[51] I. Busscher, J. J. W. Ploegmakers, G. J. Verkerke, e A. G. Veldhuizen, «Comparative anatomical dimensions of the complete human and porcine spine», *Eur Spine J*, vol. 19, n. 7, pagg. 1104–1114, lug. 2010, doi: 10.1007/s00586-010-1326-9.

[52] T. M. Jackman, A. M. DelMonaco, e E. F. Morgan, «Accuracy of finite element analyses of CT scans in predictions of vertebral failure patterns under axial compression and anterior flexion», *Journal of Biomechanics*, vol. 49, n. 2, pagg. 267–275, gen. 2016, doi: 10.1016/j.jbiomech.2015.12.004.

[53] M. Palanca, G. De Donno, e E. Dall'Ara, «A novel approach to evaluate the effects of artificial bone focal lesion on the three- dimensional strain distributions within the vertebral body», nov. 2020.

[54] M. C. Costa, G. Tozzi, L. Cristofolini, V. Danesi, M. Viceconti, e E. Dall'Ara, «Micro Finite Element models of the vertebral body: Validation of local displacement predictions», *PLoS ONE*, vol. 12, n. 7, pag. e0180151, lug. 2017, doi:

10.1371/journal.pone.0180151.

[55] M. J. Fagan, S. Julian, e A. M. Mohsen, «Finite element analysis in spine research», *Proc Inst Mech Eng H*, vol. 216, n. 5, pagg. 281–298, mag. 2002, doi: 10.1243/09544110260216568.

[56] M. Dreischarf *et al.*, «Comparison of eight published static finite element models of the intact lumbar spine: Predictive power of models improves when combined together», *Journal of Biomechanics*, vol. 47, n. 8, pagg. 1757–1766, giu. 2014, doi: 10.1016/j.jbiomech.2014.04.002.

[57] C. M. Whyne e S. S. Hu, «Parametric finite element analysis of vertebral bodies affected by tumors», *Journal of Biomechanics*, pag. 8, 2001.

[58] M. Viceconti, M. Davinelli, F. Taddei, e A. Cappello, «Automatic generation of accurate subject-specific bone finite element models to be used in clinical studies», *Journal of Biomechanics*, vol. 37, n. 10, pagg. 1597–1605, ott. 2004, doi: 10.1016/j.jbiomech.2003.12.030.

[59] M. C. Costa, «Effect of size and location of simulated lytic lesions on the structural properties of human vertebral bodies, a micro-finite element study», *Bone Reports*, pag. 9, 2020.

[60] P. A. Kramer, A. G. Hammerberg, e A. D. Sylvester, «Modeling the Spine Using Finite Element Models: Considerations and Cautions», in *Spinal Evolution*, E. Been, A. Gómez-Olivencia, e P. Ann Kramer, A c. di Cham: Springer International Publishing, 2019, pagg. 387–400.

[61] D. R. Carter e W. C. Hayes, «The Compressive Behavior of Bone as a Two-Phase Porous Structure», *J. Bone Jt Surg.*, n. 59A, pagg. 954-962., 1977.

[62] C. M. Whyne, S. S. Hu, K. L. Workman, e J. C. Lotz, «Biphasic Material Properties of Lytic Bone Metastases», *Annals of Biomedical Engineering*, vol. 28, n. 9, pagg. 1154–

1158, set. 2000, doi: 10.1114/1.1313773.

[63] M. A. Stadelmann, «Conventional finite element models estimate the strength of metastatic human vertebrae despite alterations of the bone’s tissue and structure», pag. 14, 2020.

[64] B. Helgason *et al.*, «A modified method for assigning material properties to FE models of bones», *Medical Engineering & Physics*, vol. 30, n. 4, pagg. 444–453, mag. 2008, doi: 10.1016/j.medengphy.2007.05.006.

[65] «Italian Ethical Approval». 2019.

[66] «Ethics Application». 2019.

[67] Available on: https://www.qrm.de/en/products/european-spine-phantom/#Key-Feature.

[68] M. L. Bouxsein, S. K. Boyd, B. A. Christiansen, R. E. Guldberg, K. J. Jepsen, e R. Müller, «Guidelines for assessment of bone microstructure in rodents using micro-computed tomography», *J Bone Miner Res*, vol. 25, n. 7, pagg. 1468–1486, giu. 2010, doi: 10.1002/jbmr.141.

[69] M. Pazianas, S. van der Geest, e P. Miller, «Bisphosphonates and bone quality», *BoneKEy Reports*, vol. 3, mag. 2014, doi: 10.1038/bonekey.2014.24.

Appendix A

For each specimen affected by lytic metastases the three-dimensional colour maps of the principal strain field were reported. On the left, a 3D reconstruction of the spine segment from the qCT images is reported. Each vertebra was post-process and analysed separately: full-field maximum (Eps1) and minimum principal (Eps3) strains in the lytic-metastatic and in the control vertebra and the Biomechanical Volumetric Ratio (BVR). On the right the distribution of the minimum principal strain in the lytic-metastatic and control vertebra is superimposed on the μCT cross-section where the metastasis is located. White circles indicate the lesions.

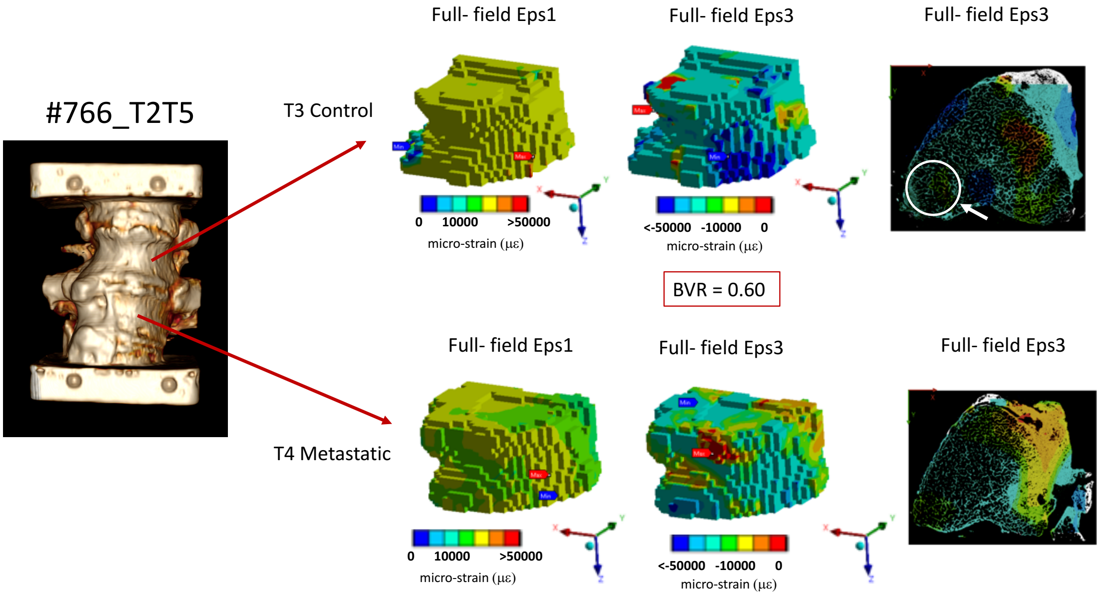

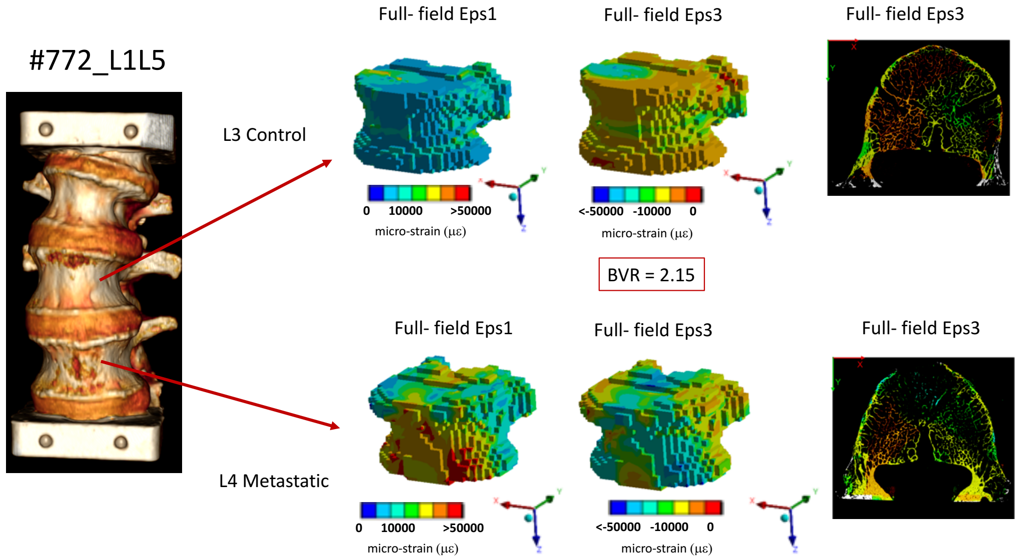
#772_L1L5
L3 Control
L4 Metastatic
Full- field Eps1
Full- field Eps3
Full- field Eps3
0 10000 >50000
micro-strain (με)
<-50000 -10000 0
micro-strain (με)
BVR = 2.15
Full- field Eps1
Full- field Eps3
Full- field Eps3
0 10000 >50000
micro-strain (με)
<-50000 -10000 0
micro-strain (με)

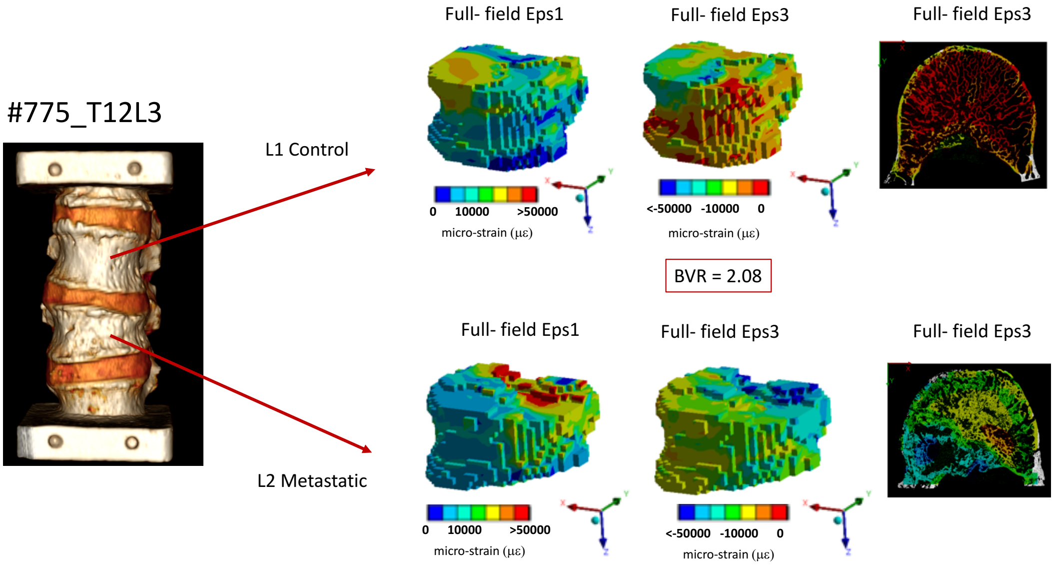
#775_T12L3
L1 Control
L2 Metastatic
Full- field Eps1
Full- field Eps3
Full- field Eps3
0 10000 >50000
micro-strain (με)
<-50000 -10000 0
micro-strain (με)
BVR = 2.08
Full- field Eps1
Full- field Eps3
Full- field Eps3
0 10000 >50000
micro-strain (με)
<-50000 -10000 0
micro-strain (με)

As well as, for mixed-metastatic vertebrae, three-dimensional colour maps were reported. On the left, a 3D reconstruction of the spine segment from the qCT images is reported. Each vertebra was post-process and analysed separately: full-field maximum (Eps1) and minimum principal (Eps3) strains in the mixed-metastatic and in the control vertebra and the Biomechanical Volumetric Ratio (BVR). On the right the distribution of the minimum principal strain in the lytic-metastatic and control vertebra is superimposed on the μCT cross-section where the metastasis is located. White circles indicate the lesions.

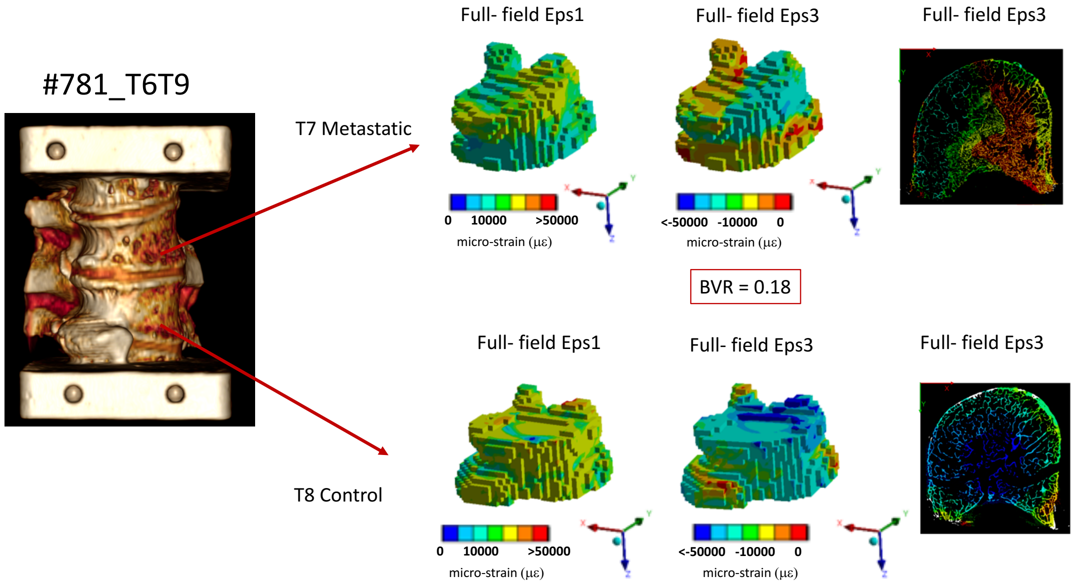

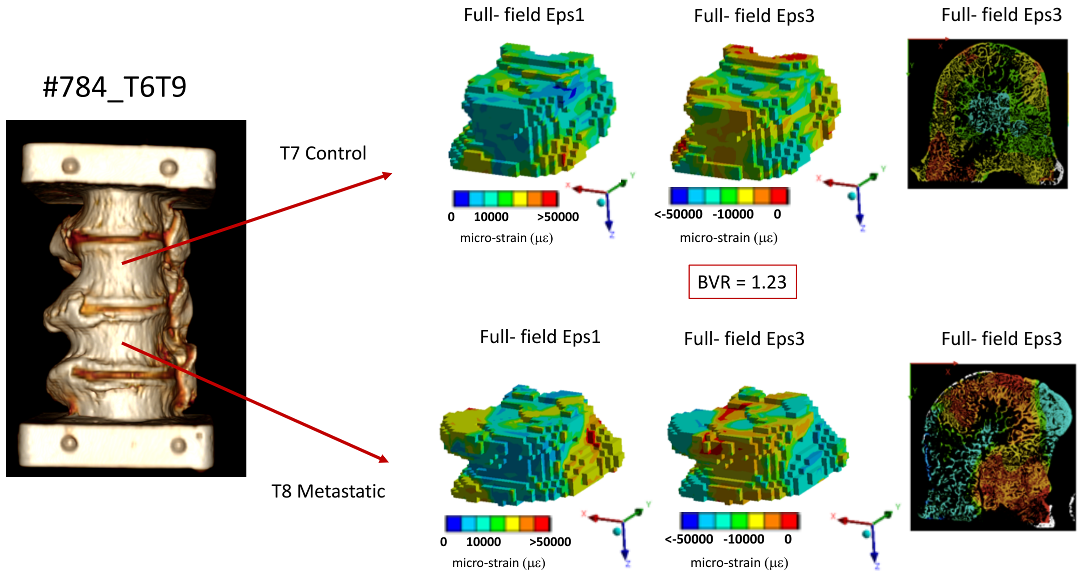

Appendix B

For each specimen affected by lytic metastases, frequency plots were reported: µCT cross-sections of the top (left column), middle (central column), bottom (right column) longitudinal ROIs of the control and lytic-metastatic vertebra; maximum principal (Eps1) and minimum principal (Eps3) strain in the top (left column), middle (central column), bottom (right column) longitudinal ROIs of lytic-metastatic (orange) and control vertebra (blue).

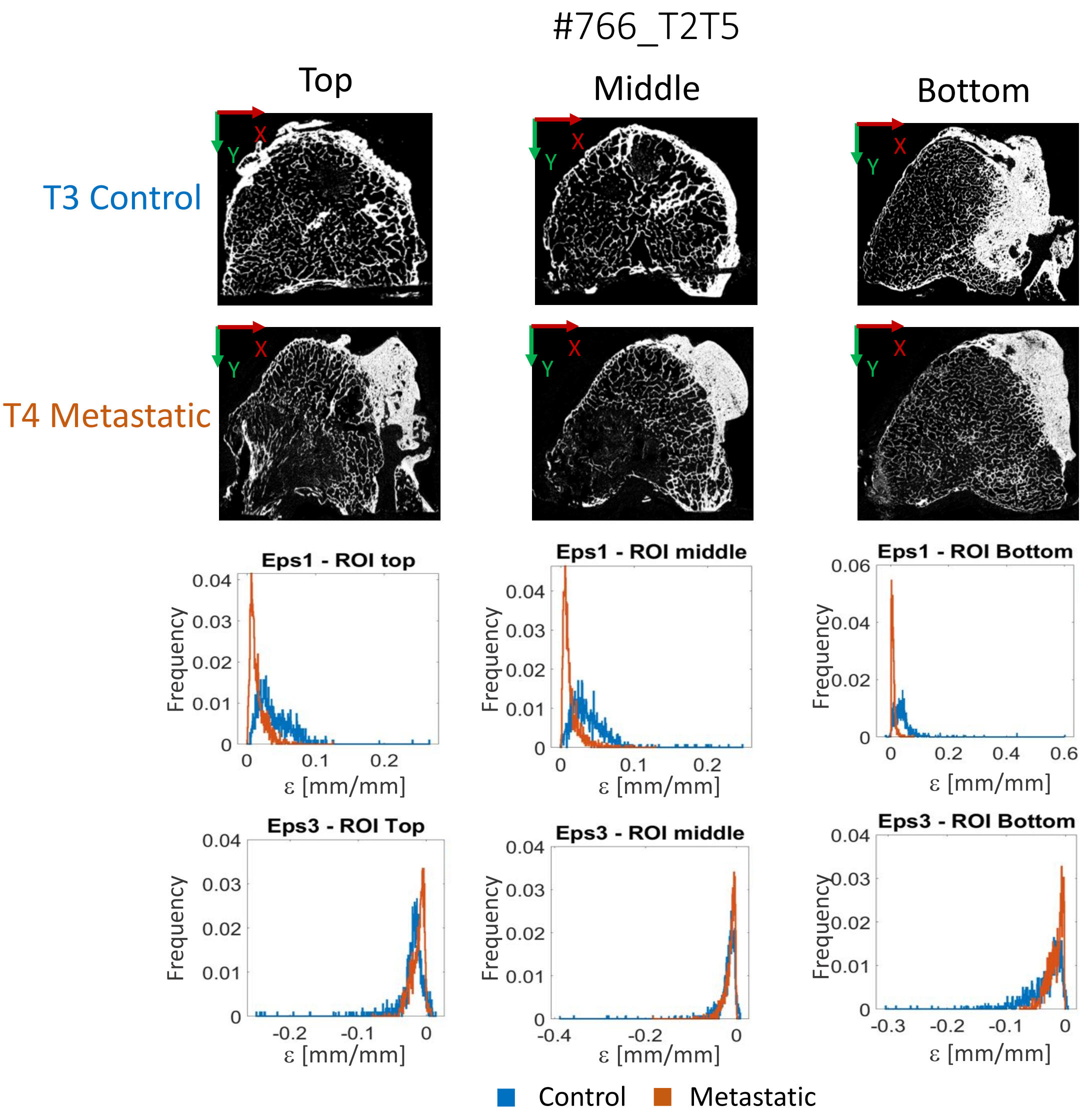

#772_L2L5

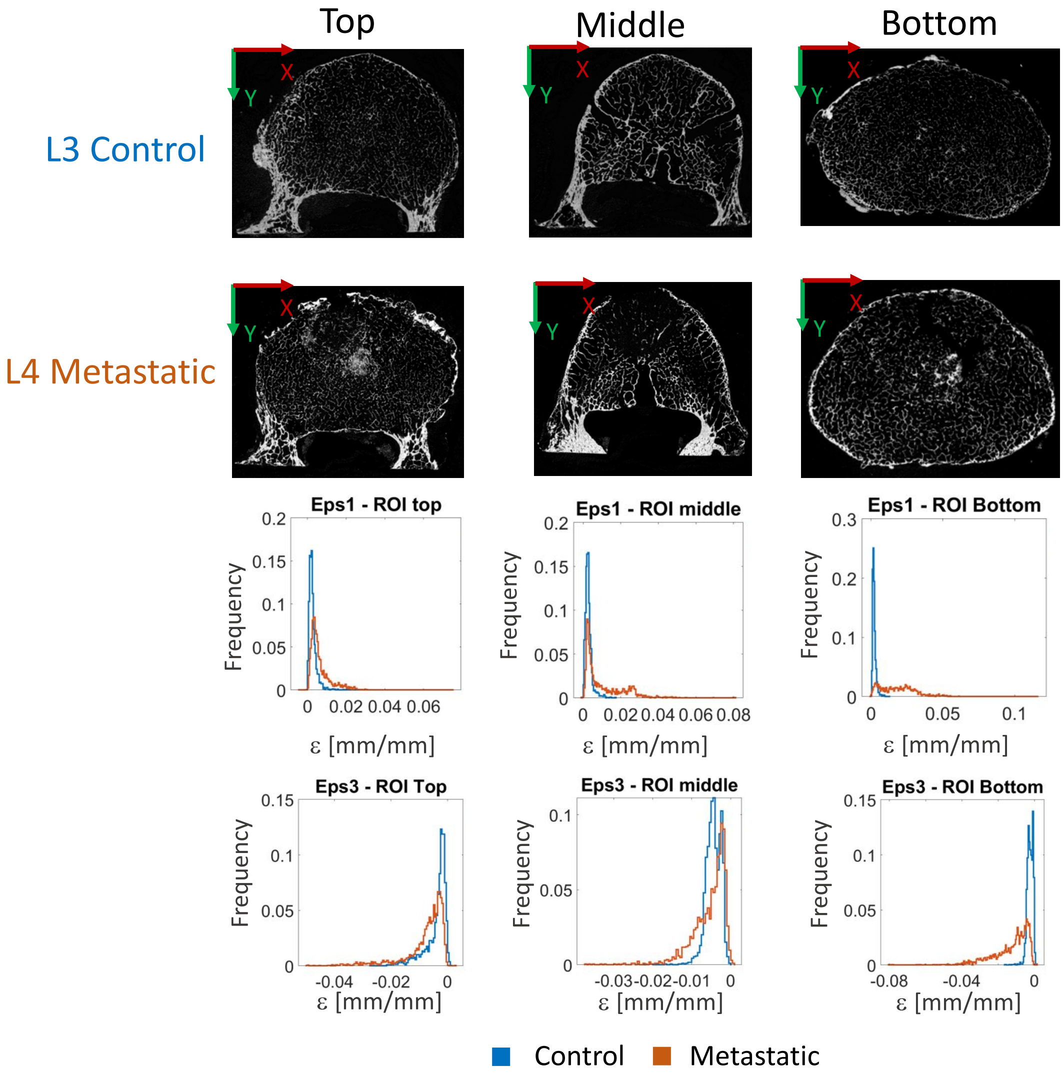
Top
Middle
Bottom
L3 Control
L4 Metastatic
X
Y
Eps1 - ROI top
Eps1 - ROI middle
Eps1 - ROI Bottom
Eps3 - ROI Top
Eps3 - ROI middle
Eps3 - ROI Bottom
Frequency
ε [mm/mm]
0 0.02 0.04 0.06
0 0.02 0.04 0.06 0.08
0 0.05 0.1
-0.04 -0.02 0
-0.03 -0.02 -0.01 0
-0.08 -0.04 0
0 0.05 0.1 0.15 0.2 0.3
🟦 Control 🟧 Metastatic

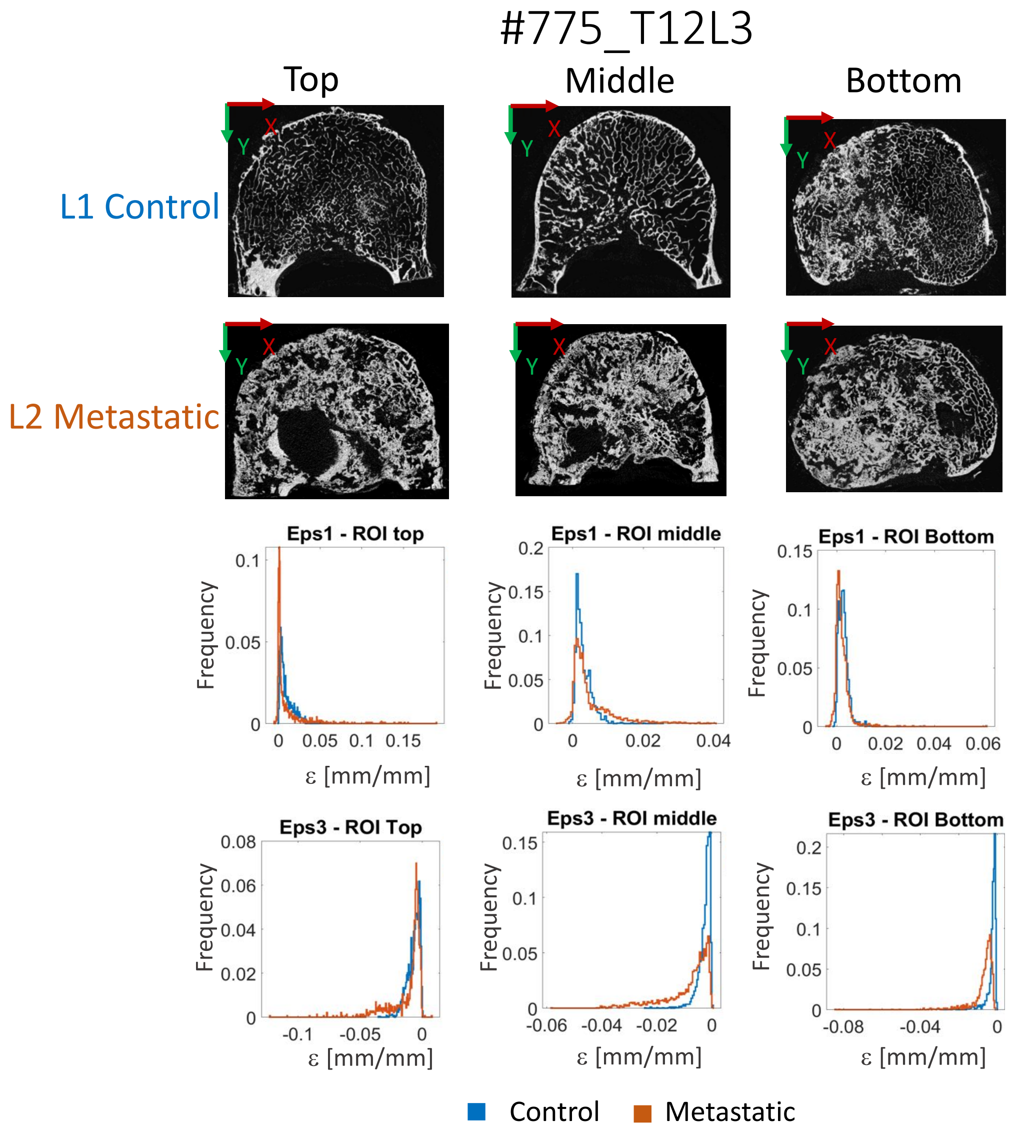
#775_T12L3
Top
Middle
Bottom
L1 Control
L2 Metastatic
X
Y
Eps1 - ROI top
Eps1 - ROI middle
Eps1 - ROI Bottom
Eps3 - ROI Top
Eps3 - ROI middle
Eps3 - ROI Bottom
Frequency
ε [mm/mm]
0.1
0.05
0
0.05 0.1 0.15
0.2
0.15
0.02
0.04
0.06
0.08
-0.1
-0.05
-0.06 -0.04 -0.02
-0.08 -0.04
■ Control ■ Metastatic

As well as, for mixed-metastatic vertebrae, frequency plots were reported: µCT cross-sections of the top (left column), middle (central column), bottom (right column) longitudinal ROIs of the control and mixed-metastatic vertebra; maximum principal (Eps1) and minimum principal (Eps3) strain in the top (left column), middle (central column), bottom (right column) longitudinal ROIs of lytic-metastatic (orange) and control vertebra (blue).

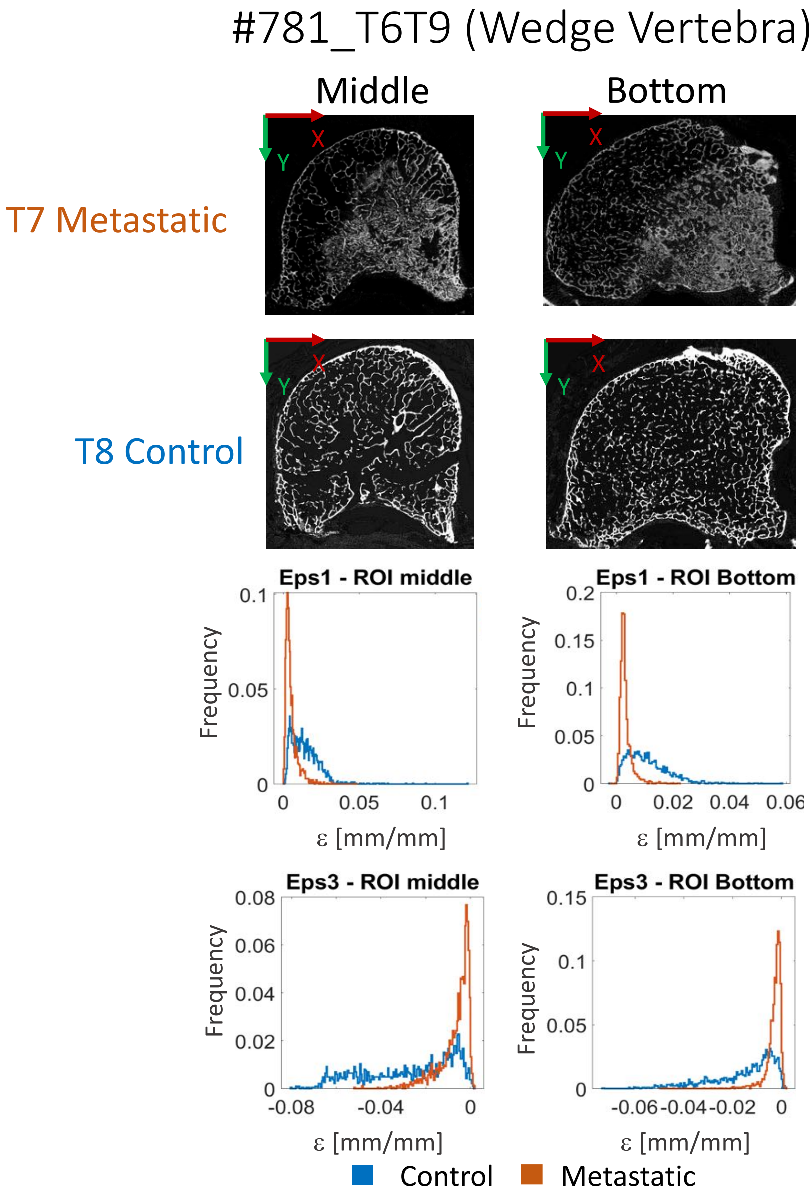

#784_T6T9

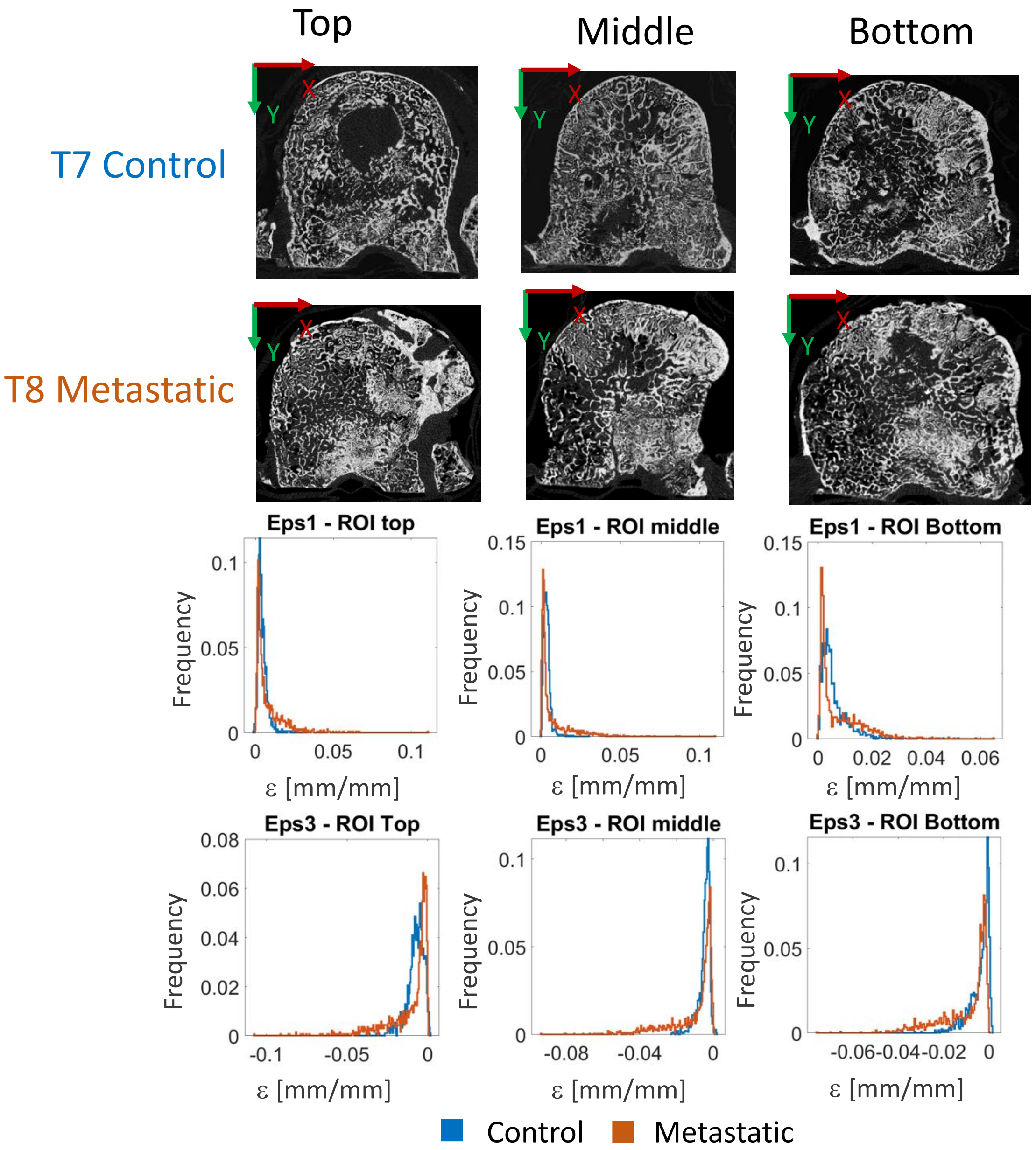
Top
Middle
Bottom
T7 Control
T8 Metastatic
X
Y
Eps1 - ROI top
Eps1 - ROI middle
Eps1 - ROI Bottom
Frequency
0.1
0.05
0
0.15
0.05
0.1
ε [mm/mm]
0.02 0.04 0.06
Eps3 - ROI Top
Eps3 - ROI middle
Eps3 - ROI Bottom
0.08
0.06
0.04
0.02
-0.1
-0.05
-0.08
-0.04
-0.06-0.04-0.02
Control
Metastatic

Appendix C

For each specimen affected by lytic metastases, thematic colour maps were reported. From left to right: µCT cross-sections of the top, middle and bottom longitudinal ROIs of the control and lytic-metastatic vertebra (red circles indicate the lesions); Biomechanical Volumetric Ratio for each subROI. Thematic colour maps: blue = smaller Eps3 in the metastatic than in the control vertebra, larger than the measurement uncertainties; grey = differences below the sum of the systematic and random error of Eps3 and above their differences; red = larger Eps3 in the metastatic than in the control vertebra, larger than the measurement uncertainties.

#766_T2T5

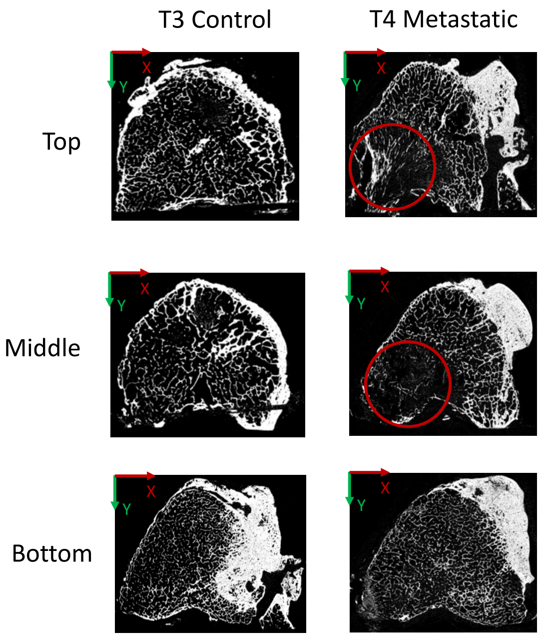

Biomechanical Volumetric Ratio

Top

0.22	0.42	0.39
0.24	0.86	1.79
0.15	0.65	0.85

🟦 AL	🟦 A	🟦 AR
🟦 L	⬜ C	🟥 R
🟦 PL	🟦 P	🟦 PR

Middle

0.23	0.17	0.10
0.98	1.21	0.94
0.62	1.51	1.63

🟦 AL	🟦 A	🟦 AR
⬜ L	🟥 C	⬜ R
🟦 PL	🟥 P	🟥 PR

Bottom

0.12	0.56	0.56
0.53	0.73	0.43
0.53	0.51	0.38

🟦 AL	🟦 A	🟦 AR
🟦 L	🟦 C	🟦 R
🟦 PL	🟦 P	🟦 PR

🟦 Smaller strain ⬜ Comparable strain 🟥 Higher strain

#772_L2L5

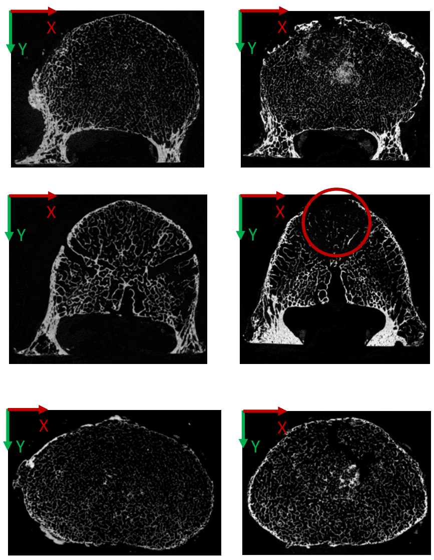

Biomechanical Volumetric Ratio

Top

2.67	4.93	1.40
1.50	4.03	0.55
2.19	11.39	1.39

🟥 AL	🟥 A	⬜ AR
⬜ L	🟥 C	🟦 R
⬜ PL	🟥 P	⬜ PR

Middle

2.61	2.52	2.10
0.83	1.25	1.36
0.47	1.15	0.77

🟥 AL	🟥 A	🟥 AR
⬜ L	⬜ C	⬜ R
🟦 PL	⬜ P	⬜ PR

Bottom

14.71	2.43	9.11
6.37	3.15	7.37
1.50	2.88	4.78

🟥 AL	🟥 A	🟥 AR
🟥 L	🟥 C	🟥 R
⬜ PL	🟥 P	🟥 PR

🟦 Smaller strain ⬜ Comparable strain 🟥 Higher strain

#775_T12L3

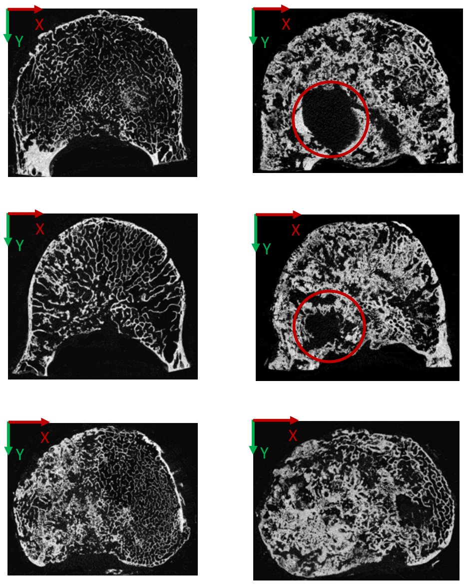

Biomechanical Volumetric Ratio

Top

4.10	0.50	0.32
3.31	0.83	0.32
719	4.05	2.08

🟥 AL	🟦 A	🟦 AR
🟥 L	⬜ C	🟦 R
🟥 PL	🟥 P	🟥 PR

Middle

4.25	3.08	1.51
4.07	1.82	2.57
4.56	3.27	2.54

🟥 AL	🟥 A	⬜ AR
🟥 L	⬜ C	⬜ R
🟥 PL	🟥 P	🟥 PR

Bottom

3.85	3.41	1.90
3.17	2.87	1.95
5.22	1.19	1.73

🟥 AL	🟥 A	🟥 AR
🟥 L	🟥 C	⬜ R
🟥 PL	⬜ P	🟥 PR

🟦 Smaller strain ⬜ Comparable strain 🟥 Higher strain

As well as, for mixed-metastatic vertebrae, thematic colour maps were reported. From left to right: μCT cross-sections of the top, middle and bottom longitudinal ROIs of the control and mixed-metastatic vertebra (red circles indicate the lesions); Biomechanical Volumetric Ratio for each subROI. Thematic colour maps: blue = smaller Eps3 in the metastatic than in the control vertebra, larger than the measurement uncertainties; grey = differences below the sum of the systematic and random error of Eps3 and above their differences; red = larger Eps3 in the metastatic than in the control vertebra, larger than the measurement uncertainties.

#781_T6T9

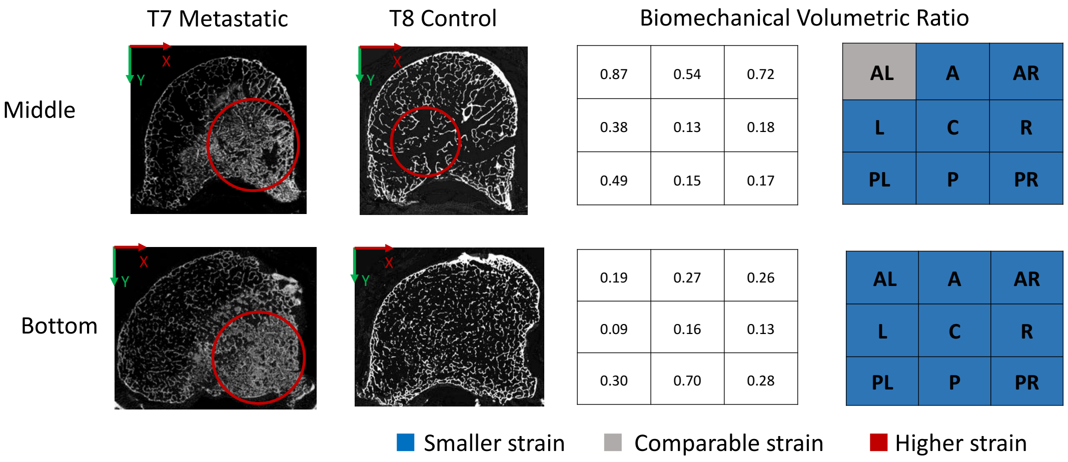

Middle	0.87	0.54	0.72	⬜ AL	🟦 A	🟦 AR
	0.38	0.13	0.18	🟦 L	🟦 C	🟦 R
	0.49	0.15	0.17	🟦 PL	🟦 P	🟦 PR
Bottom	0.19	0.27	0.26	🟦 AL	🟦 A	🟦 AR
	0.09	0.16	0.13	🟦 L	🟦 C	🟦 R
	0.30	0.70	0.28	🟦 PL	🟦 P	🟦 PR

🟦 Smaller strain ⬜ Comparable strain 🟥 Higher strain

#784_T6T9

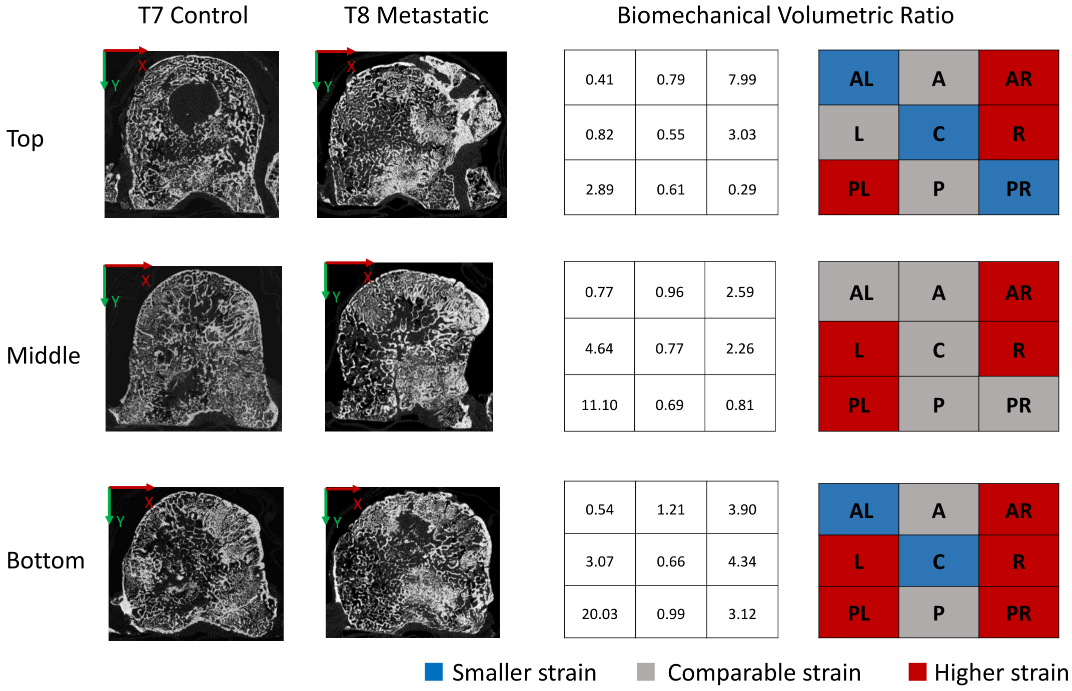

Top	0.41	0.79	7.99	🟦 AL	⬜ A	🟥 AR
	0.82	0.55	3.03	⬜ L	🟦 C	🟥 R
	2.89	0.61	0.29	🟥 PL	⬜ P	🟦 PR
Middle	0.77	0.96	2.59	⬜ AL	⬜ A	🟥 AR
	4.64	0.77	2.26	🟥 L	⬜ C	🟥 R
	11.10	0.69	0.81	🟥 PL	⬜ P	⬜ PR
Bottom	0.54	1.21	3.90	🟦 AL	⬜ A	🟥 AR
	3.07	0.66	4.34	🟥 L	🟦 C	🟥 R
	20.03	0.99	3.12	🟥 PL	⬜ P	🟥 PR

🟦 Smaller strain ⬜ Comparable strain 🟥 Higher strain